

DISPLACEMENT HISTORY OF THE NAHEF EAST
FAULT SCARP, NORTHERN ISRAEL: A COSMOGENIC ^{36}Cl
APPROACH

A Thesis Presented

by

Sara E. Gran

to

The Faculty of the Graduate College

of

The University of Vermont

In Partial Fulfillment of the Requirements

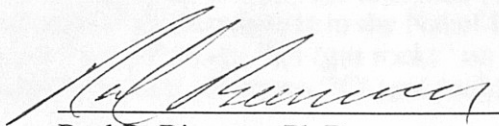
for the Degree of Master of Science

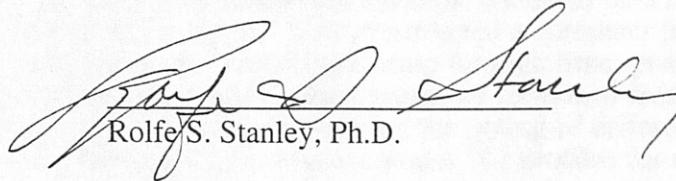
Specializing in Geology

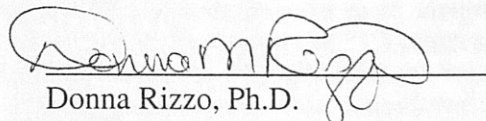
March, 2000

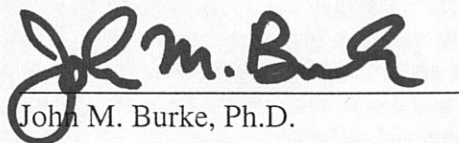
Accepted by the Faculty of the Graduate College, The University of Vermont, in partial fulfillment of the requirements for the degree of Master of Science, specializing in Geology.

Thesis Examination Committee:


Paul R. Bierman, Ph.D. Advisor


Rolfe S. Stanley, Ph.D.


Donna Rizzo, Ph.D. Chairperson


John M. Burke, Ph.D. Interim Dean,
Graduate College

Date: October 4, 1999

ABSTRACT

Cosmogenic ^{36}Cl data, collected from the Nahef East bedrock normal fault scarp (northern Israel, 33° , 300 m asl), give evidence of Holocene earthquake activity, can be interpreted to estimate rates of landform evolution, and provide insight into the mechanics of active normal faults. The Nahef East fault, which is very fresh-looking despite a lack of historic seismicity, is located on the 700 m-high Zurim Escarpment, a major geomorphic feature in northern Israel.

Forty-one limestone samples, collected from a 10.4 m-down-dip transect across the 6 km-long Nahef East normal fault scarp, were analyzed for in-situ cosmogenic ^{36}Cl and other chemical parameters. ^{36}Cl abundances in the Nahef East samples decrease regularly from a maximum 79×10^4 atoms $^{36}\text{Cl} (\text{gm rock})^{-1}$ on the limestone surface above the scarp to the minimum 11×10^4 atoms $^{36}\text{Cl} (\text{gm rock})^{-1}$ measured at the base of the scarp.

Using the ^{36}Cl production-at-depth relationships, chemical data from the scarp samples, and the geometry of the scarp, I have constructed a computer program that calculates ^{36}Cl accumulation on the Nahef Fault scarp through time, given a series of different displacement scenarios. Displacement scenarios contained from one to six equal-magnitude events. By systematically varying the timing of different rupture events (smallest time interval = 500 years), I evaluated model ^{36}Cl profiles for over 600 unique displacement histories. Model ^{36}Cl abundances for each sample resulting from these different histories were compared to the measured ^{36}Cl concentrations. If the sum of the variance between measured and modeled ^{36}Cl abundances was less than the sum of the 2σ error for the profile, the displacement history was considered acceptable.

The displacement histories resulting in acceptable ^{36}Cl values indicate that the Nahef East fault had three distinct episodes of fault activity within the past 14 kyr; over six meters of displacement occurred within a 3000 year time interval during the middle Holocene, while smaller amounts of surface rupture occurred in the late Pleistocene and late Holocene. Such a large amount of displacement in the middle Holocene indicates the potential for large and destructive earthquakes ($M > 6$) on this historically inactive fault system. The slip rate on the Nahef East fault has not been constant through time; therefore, it is not possible to calculate recurrence intervals. However, because of this fault's episodic nature, it is likely that once another earthquake occurs, more will soon follow.

This study is an advance in both the development of paleoseismological methods and in the understanding of the tectonics of northern Israel. This is the first research to determine a paleoseismic history from a bedrock fault scarp that cannot be dated using any other method. This is also one of the first studies indicating significant Holocene fault activity in northern Israel, outside of the nearby, active Dead Sea Rift zone. Nuclide dating of scarp surfaces holds great promise for advancing our understanding of the paleoseismology and potential behavior of active normal fault systems.

ACKNOWLEDGEMENTS

Many people and organizations contributed to the completion of this project. Primary thanks go to Paul Bierman, Ari Matmon, and Yehouda Enzel for developing the

Material for this thesis has been submitted for publication to the *Journal of Geophysical Research* on October 6, 1999 in the following form:

of Vermont (in the form of travel grants to Paul and a SUGR/FAME research grant to Paul and me that paid for analyses). My life in general was funded by a UVM teaching fellowship and a

Sara E. Gran, A. Matmon, P. R. Bierman, Y. Enzel, M. Caffee, D. Rizzo. Displacement history of a limestone normal fault scarp, northern Israel, from cosmogenic ^{36}Cl . *Journal of Geophysical Research*.

Paul helped with ICP and Cl analyses. Bjorn Klauw (with the support of Joel Blum) at Dartmouth College ran ICP-MS samples. Donna Rizzo taught me how to program in MATLAB, and I thank her for being extremely patient and spending so much time programming with me.

The folks at Lawrence Livermore National Laboratory (including Marc Caffee and John Southon) made this whole project possible by trusting me to run my samples on their \$10 million machine by myself through the night (DOE contract W-7405-ENG-48).

Special thanks go to John Stone at the University of Washington. He was incredibly generous with his time and intellectual property and helped me immensely with the calculus and physics that go into determining ^{36}Cl production below complicated surfaces. This project could not have been completed without his help.

ACKNOWLEDGEMENTS

Many people and organizations contributed to the completion of this project. Primary thanks go to Paul Bierman, Ari Matmon, and Yehouda Enzel for developing the idea in the first place. Funding for this project came from a multitude of sources including the Israel Atomic Energy Commission and The University of Vermont (in the form of travel grants to Paul and a SUGR/FAME research grant to Paul and me that paid for analyses). My life in general was funded by a UVM teaching fellowship and a National Science Foundation graduate fellowship.

Christine Massey, Daniel Gluek, and a gaggle of local boys assisted Paul, Ari, and me with fieldwork. Jen Larsen helped with ICP and Cl analyses. Bjorn Klaue (with the support of Joel Blum) at Dartmouth College ran ICP-MS samples. Donna Rizzo taught me how to program in MATLAB, and I thank her for being extremely patient and spending so much time programming with me.

The folks at Lawrence Livermore National Laboratory (including Marc Caffee and John Southon) made this whole project possible by trusting me to run my samples on their \$10 million machine by myself through the night (DOE contract W-7405-ENG-48).

Special thanks go to John Stone at the University of Washington. He was incredibly generous with his time and intellectual property and helped me immensely with the calculus and physics that go into determining ^{36}Cl production below complicated surfaces. This project could not have been completed without his help.

Finally, thanks to those who have just “been there” for me throughout this whole graduate school experience; first and foremost, my parents, Dick and Gloria Gran, who have always encouraged me and have humored endless discussions about what I have been working on, “so, explain it to me so I can explain it to my friends....” My brother, Rik, and sister-in-law, Karen, both allowed me to bounce ideas off of them and gloried in asking frighteningly challenging questions. Thanks to Kyle Nichols and Erik Clapp for the incessant teasing, falafel indeed! Finally, I thank Dave Mitchell for being an amazingly patient and supportive friend who helped me get through sometimes-difficult times, and who has continued to love me throughout this whole ordeal.

Production rate calibration	10
Exposure age calculations	12
Erosion rate and landform evolution	14
Paleoseismology, fault recurrence, and fault segmentation	15
Paleoseismology methods	16
Bedrock scarps	20
Paleoseismicity magnitude	20
Fault segmentation	21
Slip rates and recurrence intervals	23
Fault behavior models	25
CHAPTER 3: Article for the Journal of Geophysical Research	28
ABSTRACT	29
1. Introduction	29
1.1 Study area	30
1.2 Fault scarp dating and scarp-earthquake relationships	32
1.3 Recurrence intervals, characteristic earthquakes, and fault segmentation	33
2. Methods	34
2.1 Field methods	34
2.2 Analytical methods	36
3. Data	38
3.1 Fault displacement data	38
3.2 Isotopic and chemical data	38
4. Numerical modeling of ¹⁰ Be accumulation on an active fault scarp	39
4.1 Steady-state erosion rate of upper limestone surface and pre-faulting nuclide abundance	40
4.2 ¹⁰ Be accumulation on tilted surfaces	41
4.3 ¹⁰ Be accumulation during faulting	42
4.4 Model results	43
5 Discussion	45
5.1 Nahal East fault behavior deduced from ¹⁰ Be data and supporting evidence for the timing of fault motion	45
5.2 Testing models of fault behavior	46

TABLE OF CONTENTS

CITATION	ii
ACKNOWLEDGEMENTS.....	iii
TABLE OF CONTENTS	v
LIST OF TABLES	vii
LIST OF FIGURES.....	viii
CHAPTER 1: Introduction	1
Purpose of study	1
In-situ-produced cosmogenic isotopes	2
Determining seismic histories from ³⁶ Cl accumulation on a fault scarp	4
CHAPTER 2: Literature review.....	5
Introduction.....	5
Galilee geology and tectonics	5
Stratigraphy.....	5
Geologic evolution of the Galilee	6
Seismicity of the Galilee.....	7
Cosmogenic isotopes, with emphasis on ³⁶ Cl	9
Production rate calibration	10
Exposure age calculations.....	12
Erosion rate and landform evolution	14
Paleoseismology, fault recurrence, and fault segmentation	15
Paleoseismology methods.....	16
Bedrock scarps	20
Paleoearthquake magnitude	20
Fault segmentation.....	21
Slip rates and recurrence intervals.....	23
Fault behavior models.....	25
CHAPTER 3: Article for the Journal of Geophysical Research.....	28
Abstract.....	29
1. Introduction.....	29
1.1 Study area.....	30
1.2 Fault scarp dating and scarp-earthquake relationships	32
1.3 Recurrence intervals, characteristic earthquakes, and fault segmentation.....	33
2. Methods	34
2.1 Field methods	34
2.2 Analytical methods	36
3. Data.....	38
3.1 Fault displacement data.....	38
3.2 Isotopic and chemical data	38
4. Numerical modeling of ³⁶ Cl accumulation on an active fault scarp.....	39
4.1 Steady-state erosion rate of upper limestone surface and pre-faulting nuclide abundance	40
4.2 ³⁶ Cl accumulation on tilted surfaces	41
4.3 ³⁶ Cl accumulation during faulting.....	42
4.4 Model results	43
5 Discussion.....	45
5.1 Nahef East fault behavior deduced from ³⁶ Cl data and supporting evidence for the timing of fault motion	45
5.2 Testing models of fault behavior.....	46

5.3 The role of the Nahef East fault in the evolution of the Zurim Escarpment.....	47
5.4 Seismic hazard of the Zurim Escarpment fault system.....	50
5.5 Prospects for cosmogenic isotope dating.....	51
5.6 Implications for paleoseismology.....	52
Acknowledgements.....	53
References.....	53
Appendix 1— ^{36}Cl production mechanisms.....	58
Spallation of ^{40}Ca	58
Muon capture by ^{40}Ca	59
Thermal neutron capture by ^{35}Cl	60
COMPREHENSIVE BIBLIOGRAPHY.....	83
APPENDIX A—Sample processing.....	90
APPENDIX B—Dissolution data.....	92
APPENDIX C—Chloride carrier information.....	97
APPENDIX D—ICP major element data.....	98
APPENDIX E—Chlorine data.....	103
APPENDIX F— Y_{ca} scaling for muon capture reactions.....	107
APPENDIX G—Calculation of f_{35}	110
APPENDIX H— ^{36}Cl production from radiogenic (α,n) reactions.....	111
APPENDIX I—Production rates from neutrons on tilted surfaces.....	114
APPENDIX J—Muon scaling on tilted surfaces.....	117
APPENDIX K—Rock density.....	119
APPENDIX L—MATLAB 5.6 model.....	120

LIST OF TABLES

Figure 2-1. Stratigraphic column of Galilee rock units.....	8
Table 1. Chemical and isotopic data from Nahef East fault scarp samples	78
Table 2. Isotopic data from laboratory blanks	80
Table A1. List of symbols and units for ^{36}Cl production equations.....	81
Table A2. Published ^{36}Cl production rates from calcium spallation.....	82
Figure 5. Photograph of the Nahef East fault scarp	88
Figure 6. Measured ^{36}Cl abundance (10^5 atoms ^{36}Cl (gm rock) $^{-1}$) in Nahef East limestone samples	69
Figure 7. ^{36}Cl production rates at depth for the seven production pathways, assuming 10 ppm Cl in pure calcite (CaCO_3).....	70
Figure 8. Steady-state ^{36}Cl abundances in the upper samples as they are exhumed at different erosion rates.....	71
Figure 9. Sample shielding depth throughout time with respect to each fault block for a hypothetical, 12 kyr, two-event exposure history.....	72
Figure 10. Best fit displacement scenarios for 4, 5, and 6 events	73
Figure 11. Model ^{36}Cl values for three different displacement histories.....	74
Figure 12. Relative likelihood that displacement events occur in certain time intervals, for the four-, five- and six-event series	75
Figure 13. Lowest residual (χ^2) value for each displacement history series.....	76
Figure 14. Space-time and displacement diagrams showing different models of tectonic activity for the Nahef East fault.....	77

LIST OF FIGURES

Figure 2-1. Stratigraphic column of Galilee rock units	8
Figure 1. Location map of the Nahef East fault scarp	64
Figure 2. Vertical offset of the Nahef East fault scarp	65
Figure 3. Topographic map of the Nahef East fault scarp	66
Figure 4. Cross-section of the Nahef East fault scarp	67
Figure 5. Photograph of the Nahef East fault scarp	68
Figure 6. Measured ^{36}Cl abundance (10^5 atoms ^{36}Cl (gm rock) $^{-1}$) in Nahef East limestone samples	69
Figure 7. ^{36}Cl production rates at depth for the seven production pathways, assuming 10 ppm Cl in pure calcite (CaCO_3)	70
Figure 8. Steady-state ^{36}Cl abundances in the upper samples as they are exhumed at different erosion rates	71
Figure 9. Sample shielding depth throughout time with respect to each fault block for a hypothetical, 12 kyr, two-event exposure history	72
Figure 10. Best fit displacement scenarios for 4, 5, and 6 events	73
Figure 11. Model ^{36}Cl values for three different displacement histories	74
Figure 12. Relative likelihood that displacement events occur in certain time intervals, for the four-, five- and six-event series	75
Figure 13. Lowest residual (χ^2) value for each displacement history series	76
Figure 14. Space-time and displacement diagrams showing different models of tectonic activity for the Nahef East fault	77

CHAPTER 1: Introduction

This thesis is written to follow the University of Vermont Graduate College guidelines for a journal article thesis. 'Chapter 1: Introduction,' provides an overview of the project and states the significance of this study. 'Chapter 2: Literature Review,' contains a comprehensive literature review, including: a geologic and tectonic overview for the field area, a review of the cosmogenic isotope literature, a discussion of the theory and methodology of paleoseismology (dating and size estimation of prehistoric earthquakes), and the behavior of normal faults. Chapter 3 is a journal article submitted to the *Journal of Geophysical Research*. This article focuses on the research methodology (field, chemical, and computer modeling), systematics of ^{36}Cl production beneath complex surface geometries, and the results and implications of the study. A comprehensive bibliography follows the journal article. Following the bibliography is a series of appendices that include equations that were used to calculate ^{36}Cl production rates (including chemical and geometry corrections), the data produced during the course of this project, and the complete computer code for the numerical model.

Purpose of study

This research determined the faulting history of the Nahef East normal fault, located in northern Israel (33° latitude), using in-situ cosmogenic ^{36}Cl . This project is important for several reasons. First, using ^{36}Cl to determine paleoseismic histories is a relatively untested method, yet I show that it can be extremely effective in determining scarp ages and unraveling paleoseismic histories. Second, the seismic risk of the Beit-Hakerem Valley is largely unknown. There is currently no major seismic activity in the vicinity of the Nahef East fault; however, the fault is distinguished by a fresh-looking, 9-meter high limestone scarp. The question of seismic risk looms over the Beit-Hakerem

CHAPTER 1: Introduction

This thesis is written to follow the University of Vermont Graduate College guidelines for a journal article thesis. 'Chapter 1: Introduction,' provides an overview of the project and states the significance of this study. 'Chapter 2: Literature Review,' contains a comprehensive literature review, including: a geologic and tectonic overview for the field area, a review of the cosmogenic isotope literature, a discussion of the theory and methodology of paleoseismology (dating and size estimation of prehistoric earthquakes), and the behavior of normal faults. Chapter 3 is a journal article submitted to the *Journal of Geophysical Research*. This article focuses on the research methodology (field, chemical, and computer modeling), systematics of ^{36}Cl production beneath complex surface geometries, and the results and implications of the study. A comprehensive bibliography follows the journal article. Following the bibliography is a series of appendices that include equations that were used to calculate ^{36}Cl production rates (including chemical and geometry corrections), the data produced during the course of this project, and the complete computer code for the numerical model.

Purpose of study

This research determined the faulting history of the Nahef East normal fault, located in northern Israel (33° latitude), using in-situ cosmogenic ^{36}Cl . This project is important for several reasons. First, using ^{36}Cl to determine paleoseismic histories is a relatively untested method, yet I show that it can be extremely effective in determining scarp ages and unraveling paleoseismic histories. Second, the seismic risk of the Beit-Hakerem Valley is largely unknown. There is currently no major seismic activity in the vicinity of the Nahef East fault; however, the fault is distinguished by a fresh-looking, 9-meter high limestone scarp. The question of seismic risk looms over the Beit-Hakerem

Valley, a densely populated area (80,000 people live in the valley itself) that is riddled with similar fault scarps. Before this study, there were no numerical ages for any of the scarps, and it was uncertain whether any of them (including the Nahef East fault) still posed a seismic risk. By revealing both the timing and magnitude of surface displacement, this study provides some information on rates of landscape evolution and allows the investigation of different models of fault behavior.

I have measured ^{36}Cl in 41 samples taken from and near a 10.4 m down-dip transect of the partially-dolomitized limestone of the Nahef fault scarp. These data, paired with an interpretive numerical model, indicate that the scarp formed during the Holocene, and give a range of possible displacement scenarios.

In-situ-produced cosmogenic isotopes

Measurement of in-situ produced cosmogenic isotopes has become an effective method by which to determine exposure ages and erosion rates of bedrock surfaces. As early as 1955, researchers deduced that the interaction between cosmic rays and terrestrial materials would produce otherwise-rare isotopes that could be measured and used to estimate exposure ages (Davis and Shaeffer, 1955). Advances in accelerator mass spectrometry allowed measurement of the vanishingly-small abundances of the cosmogenic isotopes in reasonably-sized samples (< 1 kg rock) (Elmore and Phillips, 1987; Leavy et al., 1987). Increased understanding of cosmogenic isotope systematics (based on experimental, empirical, and theoretical studies—see Chapter 2) enables researchers to estimate erosion rates and exposure ages from once-ambiguous isotope data with a higher degree of certainty (Gillespie and Bierman, 1995).

Cosmogenic isotopes form when secondary cosmic ray particles (including fast neutrons, thermal neutrons, negative muons, and fast muons) cause nuclear reactions with

target atoms within the crystal lattices of minerals (Lal, 1988). Isotope production rates are, in general, dependent on several properties: the number of cosmic rays traveling through the material in question (flux), and the concentration of nuclide-producing target elements in the rock (Lal, 1988).

The cosmic ray flux is dependent on many factors. The altitude and latitude of the target material has a significant effect on cosmic ray intensity (Lal, 1988; Lal, 1991). Secondary cosmic rays are created when primary cosmic rays (usually protons) enter the atmosphere, react with the gasses, and create showers of new particles (Friedlander, 1989). These new particles, including neutrons and muons, then cascade toward Earth's surface. Cosmic rays react with atoms in the atmosphere (creating atmospheric cosmogenic isotopes such as ^{14}C as a result) and attenuate; therefore, the number of rays reaching a given surface is dependent on the altitude of that surface (Lal, 1988). Latitude dependence of the cosmic ray flux exists because most secondary cosmic rays were formed originally from primary cosmic ray protons and protons are deflected by the Earth's magnetic field; because of the positive charge of the protons and the alignment of the magnetic field, fewer rays are deflected near the poles than at the equator. Therefore, production rates of cosmogenic isotopes are higher near the poles than at the equator (Lal, 1988).

When considering sub-surface isotope accumulation (as in this project), one must also consider cosmic ray attenuation with depth in rock. Neutrons attenuate rapidly once they start penetrating rock, therefore neutron-produced cosmogenic isotopes are largely limited to the upper 2 to 3 meters of a solid rock surface (Lal, 1988; Lal, 1991; Stone et al., 1996a). Fast-neutron-produced thermal neutrons are also limited to the upper meters of rock (Dep et al., 1994a; Liu et al., 1994). Muons are able to penetrate deeper than neutrons and can create measurable amounts of cosmogenic isotopes as deep as 30 meters, both from muon capture and muon-produced thermal neutrons (Charalumbus,

1971; Stone et al., 1998). Finally, radiogenically-produced thermal neutrons also create ^{36}Cl ; this form of nuclide production is not depth-dependent (Fabryka-Martin, 1988; Stone et al., 1998). A thorough treatment of ^{36}Cl production at depth in carbonate rocks is presented in Chapter 3.

Determining seismic histories from ^{36}Cl accumulation on a fault scarp

The approach I have taken to determine the paleoseismic history of the Nahef East fault scarp is to create a numerical model that calculates and tracks ^{36}Cl accumulation through time given a displacement history. This model, written in the computer program *MATLAB 5.6*, is based on the geometry of the Nahef East fault scarp, the chemistry of the collected samples, the ^{36}Cl production at depth relationships, and an iterative series of model displacement scenarios. I then compare the model ^{36}Cl values to those actually measured on the scarp. By considering analytical error and running multiple simulations with the *MATLAB* model, I have determined a range of possible displacement scenarios.

From these multiple scenarios, I have developed a robust picture of when displacement occurred on the Nahef East fault. Once the timing of rupture events is known, one can then proceed to the overall goals of paleoseismology, studying fault behavior and determining seismic risk.

CHAPTER 2: Literature review

Introduction

This chapter describes literature relevant to this study. There are three sections: (1) *Galilee geology and tectonics*, (2) *Cosmogenic isotopes, with emphasis on ^{36}Cl* , and (3) *Paleoseismology, fault recurrence, and fault segmentation*. Very little has been published on the stratigraphy of the Nahel region since Freund's research in the 1960s and early 1970s (Freund, 1965b, Freund, 1970).

Galilee geology and tectonics

The Galilee region of northern Israel is located north of the Jezreel Valley and west of the Dead Sea Transform (Figure 1, Chapter 3). The region consists mainly of Cretaceous carbonates, which have subsequently been deformed through gentle folding and faulting (Freund, 1965a; Freund, 1970; Matmon et al., 1999). The geomorphology of the region consists of gently dipping sedimentary layers separated by faults into various horsts and grabens (Freund, 1970). The seismicity of the Galilee today is negligible (Garfunkel et al., 1980), though the presence of several young-looking normal fault scarps attests to recent extensional activity.

Stratigraphy

During the Late Cretaceous (100 My), an extensive transgression of the Tethys Sea (proto-Mediterranean Sea) covered most of the Middle East and parts of North Africa (Freund, 1965b). Through this time (specifically the Cenomanian and Turonian, 100 to 80 Mya), thick sequences of dolomite, chalk, and limestone were deposited over the

region of today's Galilee. These carbonates probably represent reefs, though few primary structures have survived to the present day (Freund, 1965b). The Nahef East fault drops a section of Senonian chalk (80 My), which post-dates the harder limestones and dolomites, next to the contact between the Bina Formation (50 to 100 m of bioclastic and lithographic limestone) and underlying Sakhnin Formation (150 to 200 m of hard and coarse-grained dolomite) (Figure 2-1) (Freund, 1965b). Very little has been published on the stratigraphy of the Nahef region since Freund's research in the 1960s and early 1970s (Freund, 1965b, Freund, 1970).

Geologic evolution of the Galilee

Structural features within the Cretaceous carbonates of the Galilee are fairly young (Freund, 1970; Matmon et al., 1998; Matmon et al., 1999). Matmon et al. (1999) developed a history of the Galilee by interpreting the stratigraphy, geomorphology, and structure of the region. During the end of the Mesozoic, the carbonate strata of the Galilee region underwent N-S compression and were warped into a series of E-W trending folds, to be later overlain by chalk. At the end of the Eocene, the Cretaceous carbonates were exposed on a coastal plain and truncated by fluvial activity. At the same time, normal faulting began in the region, forming grabens where the chalk deposits were preserved from truncation. By the beginning of the Miocene, the coastal plain was largely eroded but contained a complicated (though truncated) stratigraphy of folded and faulted sedimentary units.

Since the Miocene, the dominant tectonic activity has been extension. Freund (1965a) postulated that this extension was possibly related to bends in the left-lateral Dead Sea Rift, 40 km to the east. The ~5% extension has resulted in a series of large, normal fault-bounded (1000 m-high) escarpments, separated by flat valleys (Freund, 1970). The development of this topography is probably quite young, based on analyses of the escarpment profiles and paleodrainage systems (Matmon et al., 1998; Matmon et al., 1999). Morphometric analysis of profiles of different escarpments indicate that they formed relatively rapidly (500 to 1000 m of relief within 2 My) within the past 10 My (Matmon et al., 1998). Wide hanging valleys indicate earlier, well-developed fluvial systems, and gravel deposits in the Beit-Hakerem Valley, containing 1 to 4.5 My basalt pebbles from the Golan Heights, which is located on the opposite side of the modern drainage divide, also indicate changes in divide locations since the Miocene (Figure 1, Chapter 3) (Matmon et al., 1999).

Seismicity of the Galilee

Along the steep southern side of the Zurim Escarpment, there are many small (2 to 6 km-long, 1 to 11 m-high) normal fault scarps (Figure 1, Chapter 3). Several of these scarps, including the Nahef East fault scarp, look quite fresh and attest to relatively recent faulting activity. New evidence of major, Holocene earthquakes in the region was discovered in a Chalcolithic (7000 to 6000 BP) cave dwelling located on the Zurim Escarpment, 4 km to the east of the Nahef East fault. Earthquake damage inside the cave (including structural collapse and the entering of a debris flow) appears to have killed

inhabitants (crushed skulls and damaged artifacts were found). U-Th samples collected from the base of stalagmites forming on the debris indicate that the earthquake probably occurred a short time before 6200 BP; (Bar-Matthews, pers. comm., 1999).

Today, the extensional faults in the Galilee are seismically quiet (Freund, 1965a; Garfunkel et al., 1980; van Eck and Hofstetter, 1990), though large (Modified Mercalli intensity IX) earthquakes have occurred in historic times on the Dead Sea Rift, affecting the Galilee (Ben-Menahem, 1981). The damage done in 1837 by the Dead Sea Rift earthquake in Safed was significant; if large earthquakes were to happen on extensional faults in the central Galilee, similar damage could occur (Ben-Menahem, 1981).

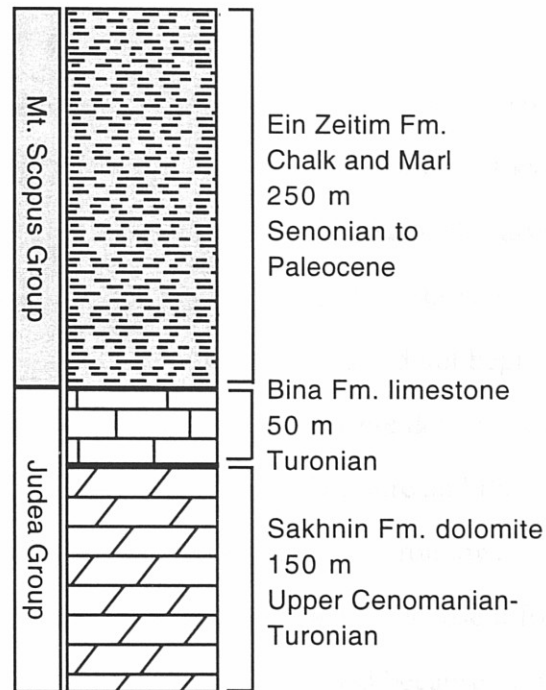


Figure 2-1. Simplified stratigraphic column of the Galilee, including rock units found adjacent to the Nahef East fault. The Senonian chalk has been dropped at least 50 meters and is now found next to Turonian carbonates.

Cosmogenic isotopes, with emphasis on ^{36}Cl

Several experimental, field-based, and theoretical studies have calibrated ^{36}Cl production rates. Six cosmogenic isotopes have been used in terrestrial geomorphic studies: ^3He , ^{10}Be , ^{14}C , ^{21}Ne , ^{26}Al , and ^{36}Cl (Lal, 1988; Lal, 1991). These isotopes can be used (under different sets of assumptions) to measure exposure ages of outcrops or landforms (Kurz et al., 1990; Phillips et al., 1990; Cerling and Craig, 1994; Bierman et al., 1995a; Stone et al., 1996b; Bierman et al., 1999), erosion rates of bedrock surfaces (Nishiizumi et al., 1991; Bierman, 1994; Bierman et al., 1995b), and denudation rates of drainage basins measured from sediments (Bierman and Steig, 1996; Granger et al., 1996; Anderson et al., 1996; Granger et al., 1997). Recently, researchers have begun measuring cosmogenic isotopes on fault surfaces to determine paleoseismic histories (Noller et al., 1996; Phillips et al., 1998; Zreda and Noller, 1998; Handwerger et al., 1999).

Field-based The hypothesis that cosmic rays could produce nuclides in terrestrial materials was first verified when Davis and Schaeffer (1955) calculated a 24 ± 4 kyr exposure age from in situ cosmogenic ^{36}Cl in a high-Cl tonalite from Colorado. Because of insensitive isotope measurement methods and limited understanding of production systematics, widespread use of cosmogenic nuclides for exposure dating did not begin until many years later, when accelerator mass spectrometry methods were developed and production rates were calibrated (Elmore, 1987; Leavy et al., 1987; Elmore and Phillips, 1987).

erosion Chlorine-36 is a well-studied isotope in atmospheric, groundwater, and terrestrial environments (Bentley, et al., 1986; Fabryka-Martin, 1988). Because it forms at a relatively high production rate in Ca- and Cl- rich rocks, and because of its moderately-long half life, 3.06×10^5 years, ^{36}Cl makes a good chronometer for many different types of rocks exposed near Earth's surface between a few thousand and 700,000 years (Phillips et al., 1986; Leavy et al., 1987; Stone et al., 1996a).

Cosmogenic isotopes, with emphasis on ^{36}Cl

Six cosmogenic isotopes have been used in terrestrial geomorphic studies: ^3He , ^{10}Be , ^{14}C , ^{21}Ne , ^{26}Al , and ^{36}Cl (Lal, 1988; Lal, 1991). These isotopes can be used (under different sets of assumptions) to measure exposure ages of outcrops or landforms (Kurz et al., 1990; Phillips et al., 1990; Cerling and Craig, 1994; Bierman et al., 1995a; Stone et al., 1996b; Bierman et al., 1999), erosion rates of bedrock surfaces (Nishiizumi et al., 1991; Bierman, 1994; Bierman et al., 1995b), and denudation rates of drainage basins measured from sediments (Bierman and Steig, 1996; Granger et al., 1996; Anderson et al., 1996; Granger et al., 1997). Recently, researchers have begun measuring cosmogenic isotopes on fault surfaces to determine paleoseismic histories (Noller et al., 1996; Phillips et al., 1998; Zreda and Noller, 1998; Handwerger et al., 1999).

The hypothesis that cosmic rays could produce nuclides in terrestrial materials was first verified when Davis and Schaeffer (1955) calculated a 24 ± 4 kyr exposure age from in situ cosmogenic ^{36}Cl in a high-Cl tonalite from Colorado. Because of insensitive isotope measurement methods and limited understanding of production systematics, widespread use of cosmogenic nuclides for exposure dating did not begin until many years later, when accelerator mass spectrometry methods were developed and production rates were calibrated (Elmore, 1987; Leavy et al., 1987; Elmore and Phillips, 1987).

Chlorine-36 is a well-studied isotope in atmospheric, groundwater, and terrestrial environments (Bentley, et al., 1986; Fabryka-Martin, 1988). Because it forms at a relatively high production rate in Ca- and Cl- rich rocks, and because of its moderately-long half life, 3.06×10^5 years, ^{36}Cl makes a good chronometer for many different types of rocks exposed near Earth's surface between a few thousand and 700,000 years (Phillips et al., 1986; Leavy et al., 1987; Stone et al., 1996a).

Production rate calibration

Several experimental, field-based, and theoretical studies have calibrated ^{36}Cl production rates for the various reactions: Ca spallation (Yokoyama et al., 1977; Zreda et al., 1991; Swanson et al., 1994; Maserik and Reedy, 1995; Phillips et al., 1996; Stone et al., 1996a); neutron activation of Cl (Dep, et al., 1994a; Dep et al., 1994b; Liu et al., 1994); and muon capture (Stone et al., 1998). Several of these studies also consider specifically the production rate of ^{36}Cl beneath the rock surface (Liu et al., 1994; Stone et al., 1998; Dunne et al., 1999).

Ca-spallation production rates have been calibrated by several different methods, in a number of areas and over various time ranges. Maserik and Reedy (1995) calibrated ^{36}Cl production rates using numerical simulations. However, field-based calibrations are more commonly made (Zreda et al., 1991; Stone et al., 1996a; Phillips et al., 1996). Field-based production rate values are calculated by measuring ^{36}Cl in surfaces of known age (most commonly constrained by ^{14}C ages). Popular calibration surfaces include basalt flows (Zreda et al., 1991; Stone et al., 1996a), and glacial landforms (Swanson et al., 1994; Phillips et al., 1996). Basalt flows may be more reliable calibration surfaces than glacial features; it is relatively easy to determine the degree of erosion on a basalt flow, and one can safely assume zero ^{36}Cl inheritance. When calibrations are done on glacial features, such as boulders on moraines, it is often difficult to quantify the amount of erosion that has taken place or accurately determine the amount of ^{36}Cl present in the boulder prior to its deposition on the moraine. Perhaps the ideal calibration surface is a well-dated bedrock surface that was deeply eroded (by tens of meters) during glaciation, and which still retains glacial striae.

Some calibrations have been done on single surfaces, which means that the calibration is most accurate for landforms of similar altitude, latitude, and age range

(Swanson et al., 1994; Clark et al., 1995; Stone et al., 1996a; Stone et al., 1998).

Production rates vary through time due to changes in the strength of Earth's magnetic field (Lal, 1988). Production rates at the poles are least sensitive to changes in the magnetic field, because at the poles the magnetic field has very little influence on the rate of incoming primary cosmic-ray protons (Lal and Peters, 1967). Because the effect of the magnetic field variation changes with latitude, calibrations are most accurate for other rocks at similar latitudes (Clark et al., 1995). Similarly, since ^{36}Cl in a rock represents the integration of a variable production rate through the time of isotope accumulation, calibrations are most accurate for rocks of similar exposure age.

Calibrations have been done using ^{36}Cl measured in both whole rock samples (Zreda et al., 1991; Swanson et al., 1994; Phillips et al., 1996) and mineral separates (Stone et al., 1996a). For calcium reactions (^{40}Ca spallation and ^{40}Ca muon capture), calibrations done using ^{36}Cl measured from Ca-rich mineral separates isolates Ca reactions more effectively than whole rock calibration; when ^{36}Cl is measured from whole-rock samples, there is a greater possibility of unexpected interactions that could either increase or decrease production rates to an unknown degree (Stone et al., 1996a). However, calibrations using whole rock samples are accurate for determining ^{36}Cl exposure ages measured from whole rock samples of similar rock types.

For this study, I use the ^{40}Ca spallation production rate of Stone et al. (1996a) of 48.8 ± 3.4 atoms $(\text{gm Ca})^{-1} \text{yr}^{-1}$ because this rate was calculated from high-Ca mineral separates (effectively isolating only Ca reactions), and because the calibration was done on the 17,300 year old Tabernacle Basalt, similar to the age of the Nahef East fault scarp (calculated using any Ca spallation production rate). The latitude of the Tabernacle Basalt is 41° (the latitude of the Galilee is 33°), making the calibration samples less sensitive to variation in the Earth's magnetic field than the samples collected for this study, though not terribly so.

Chlorine-36 production rates from thermal neutron activation of ^{35}Cl (specifically from spallation thermal neutrons) have also been described in detail. Dep et al. (1994b) modeled the systematics of ^{36}Cl production for materials of varying chemical composition and water content. In another study, Dep et al. (1994a) investigated the relationship between production rate and depth beneath the surface. Liu et al. (1994) took an experimental approach and provides a comprehensive look at ^{36}Cl production at depth from neutron capture on geomorphic surfaces; thermal neutron calculations for my thesis are based on the calculations and methods of Liu et al. (1994).

Muon-based ^{36}Cl production has been largely neglected in ^{36}Cl studies. Stone et al. (1998) provide the most recent, comprehensive treatment of muon production of ^{36}Cl . Stone et al. measured ^{36}Cl from a deep marble quarry profile and investigated all production mechanisms separately. Using both theoretical and empirical calculations, they produced a series of production-at-depth curves for each production reaction, with particular emphasis on the muon-based reactions. The sample site for Stone et al. (1998) muon study (Wombeyan Quarry, Australia, 34°S , 620 m asl) is at a latitude and altitude similar to the Nahef site (33°N , 300 m asl), and was composed of a similar lithology (calcium carbonate).

Finally, radiogenic ^{36}Cl production has been considered in detail, particularly by Fabryka-Martin (1988). She summarized much of the previous research and theoretical calculations used to calculate nuclide production rates from radiogenic neutron sources; many of the calculations in this thesis are based on the equations she summarizes.

Exposure age calculations

Davis and Shaeffer (1955) first tried using ^{36}Cl to measure exposure ages of rocks on the Earth's surface with limited, though impressive, success (considering the

analytical capabilities of the time). They extracted chlorine from several kilograms of tonalite from Colorado, and measured the $^{36}\text{Cl}/\text{Cl}$ ratio by decay-counting. Phillips et al. (1986) and Leavy et al. (1987) both proposed that with the newly-developed methods in accelerator mass spectrometry, ^{36}Cl exposure dating could be a viable geochronologic method. Both of these studies present data from a few rock samples, indicating that ^{36}Cl content can produce reasonable age estimates on surfaces of known age.

Since then, many studies have used cosmogenic ^{36}Cl accumulation to measure the ages of landforms and bedrock exposures. Phillips et al. (1990) determined a glacial chronology from ^{36}Cl measured on boulders from moraines in Bloody Canyon, in the Sierra Nevada. The ^{36}Cl chronology differed significantly from the previously determined chronology using stratigraphic relationships. The discrepancies have been attributed to the weathering of boulders and lowering of the moraine surface used for ^{36}Cl dating (Hallet and Putkonen, 1994). Not accounting for erosion of the boulders results in ages that are too young, as does ignoring the possibility that the moraine surface could have lowered significantly, thereby exposing previously-buried boulders (Hallet and Putkonen, 1994). The Bloody Canyon study serves as an example of the importance of understanding the erosional histories and geomorphic processes in operation on surfaces before reliable dates can be calculated.

Other aspects of glaciation and deglaciation have been investigated. Zreda et al. (1999) date the retreat of ice through the Nares Strait (in the Arctic) using ^{36}Cl . Briner and Swanson (1998) attempt to quantify the amount of erosion that has taken place under the Cordilleran Ice Sheet in Washington by measuring ^{36}Cl in boulders. The Briner and Swanson (1998) study does not include production of ^{36}Cl from muons, however, and therefore does not consider the full potential of nuclide inheritance.

Another application of cosmogenic ^{36}Cl exposure dating is Stone et al. (1996b), who measured ^{36}Cl from a wave-cut ocean platform. Assuming that a significant amount

of material was removed from the platform, Stone et al. determined that the platform was exhumed rapidly during the Younger Dryas, when the sea level was stable and the climate conducive to rapid bedrock weathering.

Erosion rate and landform evolution

Cosmogenic ^{36}Cl can be used to measure erosion rates, and therefore rates of landscape evolution (Bierman, 1994b). Chlorine-36 production at depth from cosmogenic and radiogenic sources and loss of ^{36}Cl to steady-state erosion of an upper surface result in rocks at all depths (including the modern surface) reaching equilibrium ^{36}Cl concentrations. The equilibrium concentrations are determined by the chemical composition of the rock (which determines the production rate) and the erosion rate of the rock surface (which determines the rate at which samples are brought to the surface) (Stone et al., 1998; Liu et al., 1994). By measuring the ^{36}Cl content of a surface rock sample, one can determine the erosion rate of that surface.

Bierman et al. (1995) investigated erosion rates by measuring ^{36}Cl from granite outcrops in California, Texas, and Georgia. In this study, Bierman et al. isolate the thermal neutron activation production pathway by measuring ^{36}Cl in chlorine-rich fluid inclusions within the granite. They created a numerical model that integrates thermal neutron activation ^{36}Cl production throughout time as a sample is brought to the surface under different erosion rates. Stone et al. (1998) investigate the erosion rate of limestone surfaces in Wombeyan, Australia. The Wombeyan study, which was done on calcium-rich rocks, models erosion rates from all production pathways (as opposed to isolating the thermal neutron pathway).

Paleoseismology, fault recurrence, and fault segmentation

Earthquakes are spectacular and destructive geologic events. Much time and many resources have been given to understand when, where, why, and in what manner they occur (Bolt, 1993; McCalpin, 1996). An excellent summary of paleoseismic research methods, explanations of recurrence intervals and fault behavior models, and an invaluable compilation of references is J. McCalpin's *Paleoseismology* (1996); much of the research summarized in the following sections was located through this book's detailed and comprehensive bibliography.

Seismic hazard assessments conducted using only historic earthquake data can result in inaccurate estimates of earthquake risk, especially if earthquake cycles are the same length or longer than the historic record. Geologic evidence of earthquakes on currently active fault systems lengthens the time span of available data, and therefore results in more accurate risk assessments (e.g. Schwartz and Coppersmith, 1984; Sieh et al., 1989). To date, most paleoseismic studies have involved trenching through active fault zones offsetting unconsolidated sediment, identifying co-seismic deposits, and then dating the deposits (McCalpin, 1996). Attempts have been made to estimate earthquake magnitude and timing from bedrock scarp weathering; however, these studies produce only relative ages for earthquake events (Stewart, 1996).

Using paleoseismic data, one can estimate the magnitude and temporal distribution of earthquakes that happened in the past (e.g. Schwartz and Coppersmith, 1984; Youngs and Coppersmith, 1985; Sieh et al., 1989). From paleoseismic data, both recurrence intervals (the average amount of time between earthquakes) and characteristic earthquake magnitudes (on some faults, earthquakes of similar size appear to occur repeatedly) can be used to determine earthquake risk in a particular area (e.g. Schwartz

and Coppersmith, 1984; Wallace, 1987; Youngs and Coppersmith, 1985; McCalpin, 1996; Bell et al., 1999).

Often, only a short segment or series of segments of a long fault system will rupture in an earthquake (Jackson and White, 1989; de Polo et al., 1991; Machette et al., 1991). Paleoseismic information from all the segments is necessary to determine earthquake recurrence intervals for the fault system as a whole.

Paleoseismology methods

The majority of paleoseismology studies have been conducted on normal faults that create scarps in or otherwise deform unconsolidated materials (e.g. Bucknam and Anderson, 1979; Schwartz and Coppersmith, 1984; Mayer, 1984; Hanks et al., 1984; Sieh et al., 1989; McCalpin et al., 1993; McCalpin, 1996; Bell et al., 1999). A trench is dug across the scarp, perpendicular to the fault trend, and detailed logs drawn of the sediments exposed on the trench walls (McCalpin, 1996). In the case of normal faults, vertical displacement will expose a scarp of unconsolidated material. Since the material is loose and often initially exposed by faulting at an angle greater than the angle of repose, it begins to slough down from the scarp face onto the base of the scarp, creating a colluvial wedge of sediment (Forman et al., 1991; McCalpin, 1996; Bell et al., 1999). If more than one earthquake occurs on the same fault, there may be several layers within the colluvial wedge. If there is enough time between earthquakes for the scarp to stabilize (and the climate is appropriate), datable soils may develop on each of the colluvial wedge deposits (McCalpin, 1996).

¹⁴C and thermoluminescence dating. Dating colluvial wedge material usually involves either ¹⁴C or thermal luminescence (TL) methods (Forman et al., 1991; Sieh et al., 1989; McCalpin, 1996). Organic material from soils, charcoal, or plant material in

colluvial wedges can be dated using ^{14}C (provided the carbon is younger than 40,000 years) (Stuiver et al., 1979; Easterbrook, 1993).

TL is a method by which one can measure when a particular sediment sample was buried (Aitken, 1985). Radiation emitted from U and Th decay causes the absorption and storage of energy in crystal lattices; this stored energy (which is proportional to the amount of time the energy has been accumulating and the dose rate) can be quantified by measuring the intensity of light released from the sample during heating. Exposure to sunlight also releases this energy, so samples exposed on the Earth's surface are effectively "zeroed" of their luminescence. Once the sample is buried, energy starts accumulating again. Measuring the TL of samples buried in the colluvial wedge indicates the time of burial (up to 300,000 years), provided that the sediment was at the surface long enough to zero properly (Easterbrook, 1993; Forman et al., 1991). Forman et al., 1991 describe in detail which kinds of colluvial sediments are most likely to have spent enough time at the surface (only 8 hours of direct sunlight is needed to release all luminescence). They conclude that fine-grained sediments near the top of individual colluvial deposits represent the material slowly deposited through sheetwash. They determine that the coarse-grained colluvium at the base of the wedge is likely to have been deposited very rapidly following the earthquake and is not suitable material to date using TL.

Morphologic dating methods. Morphologic methods have also been used to determine earthquake magnitude and timing. Fault scarp profiling and diffusion modeling have been used to determine both relative and numerical scarp ages in unconsolidated sediment (Bucknam and Anderson, 1979; Nash, 1980; Mayer, 1984; Hanks et al., 1984; Hanks and Schwartz, 1987). Displacement of dated landforms can also be quantified and interpreted in a paleoseismic context (McGill and Sieh, 1991; Machette et al., 1991; Grant and Sieh, 1994).

Dating fault scarps using diffusion models was very popular in the early 1980s, when it represented a simple and low-technology method of dating “undatable” landforms. The general concept is that scarps form at steep angles and material quickly begins to erode from the top of the scarp and collect at the base. Bucknam and Anderson (1979) developed a method for comparing the height and slope of scarps of similar and different ages. They make two conclusions: first, slope angle is proportional to the logarithm of the scarp height. Second, the slope angle decreases with age for slopes of a given height. In 1980, Nash proposed that scarps in alluvium degrade through time according to a simple diffusion model. Rates of fault scarp degradation are calibrated using scarps of known age and are applied to scarps of unknown age.

Mayer (1984) expanded on the diffusion model concept and concluded that its usefulness was largely dependent on the importance of non-diffusive processes on the scarp, such as changes in sediment cohesiveness through time. Mayer also warns against diffusion dating on composite scarps (scarps that represent more than one fault motion) because diffusion is disturbed by additional faulting. Hanks and Schwartz (1987) discussed various errors associated with measuring scarp ages using the diffusion model. In most studies, the diffusion constant, k , is measured on a feature of known age. This calibrated k value is then applied to different features (with at least similar composition and in a similar climate). As Hanks and Schwartz (1987) state, “age estimates, however, will only be as accurate as the k borrowed from some other structure of known age. Extracting this k in the first place is not without nuance and uncertainty; transferring it to another area and structure involves entirely different uncertainties, of which not much is known.”

In 1998, Nash re-visited morphologic dating of fault scarps and determined that diffusion modeling only works for simple (one motion), small (< 5 m) scarps. Scarps over 5 meters high do not seem to have the same pattern of symmetry as smaller scarps

(the top of the scarp is convex up to the same extent as the bottom of the scarp is concave up), and the sediment flux does not seem to be in proportion to scarp slope in the same manner as it is for smaller scarps (Nash, 1998). Regardless, studies continue to use morphologic parameters to determine scarp age. Recently, measurements of cosmogenic ^{36}Cl have been used to help constrain the diffusion constant for unconsolidated materials (Phillips et al., 1998).

Archaeoseismology. Displaced or destroyed archeological remains such as buildings and monuments can also be used to determine ages and magnitudes of earthquake events. Reches and Hoexter (1981) quantified displacement of a palace, located on top of the Dead Sea Transform fault in Israel. They determined that an earthquake destroyed this palace before it was completed, and were able to measure displacement by looking at deformation in the palace walls. Zhang et al. (1986) measured displacement on the Great Wall of China resulting from historic earthquakes (1739 AD) on the Yinchuan Graben. Zhang et al. (1986) were also able to calibrate fault scarp degradation models because the Great Wall was built over fresh scarps, preserving the scarp angle at the time the Wall was built. Ellenblum et al. (1998) document a large ($M > 7$) earthquake along the Dead Sea Transform damaging a crusader castle in Israel in the year 1202. This earthquake offset the walls by 1.6 meters. In each of these situations, the age of the monument or building was known, the damage could be dated using archaeological and geological techniques, and the magnitude of the earthquake estimated both from displacement data and the extent of earthquake damage. Very recent (and as yet unpublished) evidence of a cave collapse near the Nahef East fault scarp is yet another example of archaeoseismology (Bar-Matthews, pers. comm., 1999).

Co-seismic deposits. Earthquake occurrence and rupture ages can also be determined by identifying, dating, and mapping co-seismic sedimentary deposits, such as tsunami deposits and landslides (McCalpin, 1996). Atwater (1987, 1992) and Yamaguchi

et al. (1997) use tsunami deposits, dendrochronology of drowned trees, and buried soils to determine ages of large coastal earthquakes occurring on the Cascadia subduction zone. Frydman and Talesnick (1988) examine seismically-triggered landslides on the Israel coastal shelf, caused by large earthquakes on the Dead Sea Transform. These landslides resulted in tsunamis in the Mediterranean Sea. Wilson and Keefer (1983) describe earthquake characteristics and the resulting slope failure occurring in the 1979 Coyote Lake earthquake in California. The importance of the Wilson and Keefer research is that they were able to quantify ground shaking parameters capable of triggering landslides.

Bedrock scarps

Dating earthquake events that result in bedrock scarps is difficult because they lack datable material and bedrock scarp morphology changes slowly and unpredictably through time (Stewart, 1996). However, if the scarp is in a lithology that weathers fairly rapidly, such as limestone, sometimes different earthquake events are apparent from relative weathering and surface roughness horizons (Stewart, 1996; Zreda and Noller, 1998). However, using this method, it is difficult to get numerical (as opposed to relative) ages.

Paleoearthquake magnitude

It is important to be able to estimate earthquake magnitudes from paleoseismic evidence. Several studies have compiled historic earthquake characteristics and related them to earthquake magnitude (Bonilla et al., 1984; Wells and Coppersmith, 1994). These characteristics include primary evidence such as: surface rupture length, maximum vertical displacement, average vertical displacement, rupture area, and seismic moment

(McCalpin, 1996). I will focus on the maximum vertical displacement method, because such displacement is among the primary evidence collected from the Nahef East fault.

Historic data sets of earthquake maximum displacement as a function of earthquake moment magnitude (M) have been compiled (most recently) by Wells and Coppersmith (1994). In general, earthquake size increases as a log function of maximum displacement (eq. 2.1):

$$M = (6.61 \pm 0.09) + (0.71 \pm 0.15) \log (MD), \quad (2.1)$$

where M is moment magnitude and MD is the maximum displacement.

There are many sources of error involved in estimating M from maximum displacement (most of which are errors in measuring the maximum displacement of a single rupture), and these errors can cause either over- or under-estimation of earthquake magnitude. However, errors in vertical displacement of tens of cm become insignificant when dealing with displacements >1 m (a maximum vertical displacement of 0.5 m and 1 m result in earthquakes of $M = 6.4$ and 6.6, respectively).

Fault segmentation

It has long been noticed that earthquakes do not rupture entire lengths of fault zones at one time (Jackson and White, 1989; dePolo et al, 1991; Crone and Haller, 1991; McCalpin, 1996). From this observation, the concept of an *earthquake segment* arose, “discrete portions of faults that have been demonstrably ruptured to the surface two or more times...” (McCalpin, 1996). Earthquake segments are best defined from historic surface ruptures or detailed paleoseismic information. When such information is not available, segments have been defined by geologic characteristics, based on the assumption that discontinuities along a long fault zone will tend to arrest an earthquake rupture (Wheeler, 1989; Schwartz, 1989). These are called *fault segments*, and are

distinguished by the physical characteristics of the fault (Wheeler, 1989; McCalpin, 1996); however, understanding the fault behavior and segmentation characteristics depend upon knowing which segments rupture at what time. The study of fault and earthquake segmentation is limited by the resolution and accuracy of fault scarp dating and paleoseismic investigations (McCalpin, 1996).

dePolo et al. (1991) discuss the characteristics of historic surface ruptures in the Basin and Range, including: earthquake magnitudes, geometry of the faults, and characteristics of the rupture edges. With these data, dePolo et al. (1991) conclude that only about half of historic surface ruptures (earthquake segments) coincide with fault discontinuities (fault segments), and that large earthquakes ($M > 7$) rupture several segments concurrently. These conclusions are extremely important because they indicate that a comprehensive understanding of paleoseismicity on all segments of a fault system is necessary to determine paleoearthquake size and earthquake recurrence.

A similar study was conducted on the Wasatch fault zone by Machette et al. (1991). In contrast to dePolo et al. (1991), they used paleoseismic information rather than historic earthquake data. Through extensive trenching, structural mapping, and compilation of available data (largely compiled from Machette et al., 1987), Machette et al. (1991) divided the Wasatch fault zone into ten discrete segments (based mostly on structural discontinuities) and determined recurrence intervals for individual segments. Machette et al. based their segments on structural controls and obtained earthquake ages from radiocarbon dating and TL, in contrast to the historic data set compiled by dePolo et al. (1991). Machette et al. constructed an impressive earthquake and segmentation chronology with their paleoseismic data, despite their necessary assumption that fault segments are the equivalent of earthquake segments.

Crone and Haller (1991) studied normal fault segmentation in a region of the Basin and Range with the intent of characterizing segment boundaries. Using fault scarp

morphology (e.g. Nash, 1980; Mayer, 1984), structural and geomorphic mapping, and data from historic ruptures, they conclude that it is possible to identify individual rupture segments based on geomorphic characteristics. These characteristics include: en echelon offsets or gaps, distinct along-strike changes in fault scarp morphology, irregularities in a fault-bounded range front, and transverse bedrock ridges with low amounts of cumulative displacement relative to the rest of the fault. Though this study assumes that earthquakes rupture single segments (which are defined by structural, not seismological data), they do recognize that over time, "all barriers fail," and that the surface expression of normal-fault-bounded mountain ranges are explicit evidence of the transience of segment activity (Crone and Haller, 1991).

McCalpin (1996) emphasizes that there is much confusion over whether the fault segmentation concept is useful; in other words, it is still uncertain whether we can consider fault segments to be consistent with earthquake segments. If they are, reconstructing paleoseismic information from multi-segment faults becomes vastly simplified (one can assume fault segments represent rupture zones, instead of needing to find paleoseismic evidence for rupture zones). If, as dePolo et al. (1991) suggest, fault segments do not coincide with rupture events, it then becomes necessary to collect large amounts of paleoseismic data both from individual segments and from the fault system as a whole, in order to understand the earthquake behavior of the entire system.

Slip rates and recurrence intervals

An important goal of paleoseismic studies is to determine earthquake risk—the size and temporal distribution of destructive earthquakes. Seismic hazard assessments must navigate the complex relationships between geologic and paleoseismic data, recurrence and slip rate models, and fault segmentation (McCalpin, 1996). Recurrence

intervals can be calculated using either long-term slip rates or numerical ages of paleoearthquakes. If a particular fault has many different segments, each must be considered separately and then all of them as a whole in order to understand the recurrence intervals for the entire system.

Recurrence estimates can be calculated from long term slip rates (McCalpin, 1996) by simply dividing the estimated slip per event by the long term slip rate (eq. 2.2);

$$RI = D / (S - C), \quad (2.2)$$

where RI is the mean recurrence interval, D is the displacement during a typical faulting event (often estimated from historic ruptures), S is the coseismic slip rate (measured from dated, offset landforms), and C is the creep slip rate (usually assumed to be zero) (Wallace, 1970). Examples of recurrence intervals calculated using slip rates include Niemi and Hall (1992), McGill and Sieh (1991), and Bierman et al. (1995a). The advantage of using the slip rate method is one needs only a displaced and datable landform and an estimate of the average displacement occurring in one earthquake. No paleoseismic data are needed.

Recurrence interval estimation is also done using numerical ages of paleoearthquakes. If all earthquakes can be identified and dated, calculating recurrence intervals is as simple as averaging the length of quiescence between events. Sieh et al. (1989) is a classic example of calculating recurrence intervals from a well-dated paleoseismic chronology. They have used a field site (Pallet Creek, California) that contains a remarkable sedimentary record of earthquakes on the San Andreas Fault, with extremely precise radiocarbon dating (error of less than 23 years for all but two samples) to calculate that the average interval between faulting events (as calculated from the most recent 10 earthquakes) is 132 years. However, because variability exists in the amount of time between events (anywhere from < 100 to > 300 years), Sieh et al. (1989) suggest that detailed chronologies such as these do not help with calculating more precise

recurrence intervals; rather, they allow a more detailed examination of temporal patterns of earthquake occurrence. The evidence from Pallet Creek shows that earthquakes tend to cluster (several earthquakes occur within a short period of time) between longer periods of quiescence. Evidence of earthquake clustering is found in other sections of the San Andreas fault as well (Grant and Sieh, 1994).

Fault behavior models

In an attempt to describe how fault displacement varies both temporally and spatially along a fault trace, several different models of fault behavior have been developed. All are based on the assumptions that "the pattern of surface deformation during earthquakes is linked to the pattern of strain release on the underlying fault plane," and that there is a relationship between the amount of time between events and the amount of strain released (McCalpin, 1996).

Two elegant models, proposed by Shimazaki and Nakata (1980), are known as the time-predictable and the slip-predictable models. The time-predictable model suggests that earthquakes occur when a certain amount of strain has accumulated. Strain accumulation is dependent on the slip rate and the length of time since and the magnitude of the last slip event. One can then calculate the amount of time until the next slip event. The slip-predictable model suggests that all rupture events release enough energy to drop the stress back to a particular level. Therefore, the amount of slip occurring in the next earthquake can be predicted based on the slip rate and the time since the previous event (Shimazaki and Nakata, 1980; McCalpin, 1996).

The Shimazaki and Nakata models do not take into consideration that slip varies along the fault strike. Several models have been developed to take into consideration that slip rates and earthquake size are not necessarily constant along the length of the fault,

including: variable slip, uniform slip, coupled, overlap, and characteristic earthquake models (Berryman and Beanland, 1991). The variable slip model indicates that earthquake size and displacement per event vary unpredictably, but the slip rate is constant for the entire fault (Berryman and Beanland, 1991). The uniform slip model assumes that the overall slip rate is constant along the fault, there is constant displacement per event at a given point on the fault, and that constant-size large earthquakes are interspersed with more-common moderate-sized ones (McCalpin, 1996). The uniform slip model does not assume that ruptures are limited to single segments. The coupled model is nearly identical to the uniform slip model, except that ruptures are confined to single segments (McCalpin, 1996). The overlap model considers that slip can be variable along the length of the fault, displacement is constant at a point, and that large earthquakes occur with constant size. The overlap model pays particular attention to the amount of displacement occurring on overlapping rupture edges (McCalpin, 1996).

The characteristic earthquake model was developed by Schwartz and Coppersmith (1984). Their classic (and frequently-cited) study involved the compilation of paleoseismic data from the Wasatch and San Andreas fault zones, through which they concluded that "individual faults and fault segments tend to generate essentially same size or characteristic earthquakes having a relatively narrow range of magnitudes near the maximum," (Schwartz and Coppersmith, 1984). The implication is that there is not (as has been previously suggested) a log-linear relationship between recurrence and earthquake magnitude, and that the biggest earthquakes are not always the least frequent. The only major flaw with this study is that they (understandably) chose fault zones with large amounts of available data, which in this situation biased their study to the behavior of very large and persistent fault systems.

Since Schwartz and Coppersmith (1984) was published, several other studies have investigated the applicability of the characteristic earthquake model (e.g. Youngs and

Coppersmith, 1985; Berryman and Beanland, 1991; Hecker and Schwartz, 1994) with varying success. Hecker and Schwartz (1994) find evidence of characteristic earthquake behavior on many different faults. Berryman and Beanland (1991) determine that small normal faults in New Zealand seem to display widely variable fault behavior and that characteristic models do not seem to accurately describe these faults. Youngs and Coppersmith (1985) compare the characteristic and log-linear models to the behavior of faulting in the Transverse Ranges, and determine that each shows a reasonable match. They recommend that the characteristic earthquake model is valid for estimating recurrence only on major faults, and that model application should be considered on a case-by-case basis.

Finally, virtually all paleoseismic studies, whether they focus on segmentation, behavior models, or recurrence intervals, state that a greater quantity of precise paleoseismic data are needed. Currently, the vast majority of information comes from either historic ruptures or fault trenches where faults deform unconsolidated sediment and conditions are conducive to the preservation of organic material. None of the paleoseismic methods are effective for determining numerical ages of bedrock fault scarps. A method for determining paleoseismic histories from bedrock fault scarps (such as cosmogenic nuclide dating) will allow the study of fault behavior and fault segmentation in regions where conventional methods are not applicable.

CHAPTER 3: Article for the Journal of Geophysical Research

Displacement history of a limestone normal fault scarp, northern Israel, from
cosmogenic ^{36}Cl

¹S. E. Gran,

²A. Matmon,

¹P. R. Bierman,

²Y. Enzel,

³M. Caffee,

⁴D. Rizzo

¹ Geology Department
University of Vermont
Burlington, Vermont 05405

² Institute of Earth Sciences
Hebrew University
Jerusalem, Israel 91904

³ Center for Accelerator Mass Spectrometry
Lawrence Livermore National Laboratory
Livermore, California 94550

⁴ Civil and Environmental Engineering
University of Vermont
Burlington, Vermont 05405

[Stewart, 1996], but such features often cannot be used to resolve seismic history in detail

Abstract

Cosmogenic ^{36}Cl , measured in 41 limestone samples from a 9 m-high bedrock fault scarp, allows us to construct the 14 kyr-long displacement history of the Nahef East normal fault, northern Israel (300 m asl, 33° latitude). The Nahef East fault is one of a series of fault scarps located along the 700 m-high Zurim Escarpment, a major geomorphic feature in northern Israel. ^{36}Cl concentrations in the samples range from 79 to 11×10^4 atoms $(\text{gm rock})^{-1}$. Samples at the top of the scarp have the highest nuclide concentrations; samples at the base have the lowest. Using chemical data from the samples, Nahef East fault scarp geometry, and surface and subsurface production rates for the ^{36}Cl -producing reactions, we have constructed a numerical model that calculates ^{36}Cl accumulation on a scarp through time, given a series of unique displacement histories. The resultant modeled ^{36}Cl concentrations are compared to those measured in the scarp samples. Displacement histories that result in a good match between measured and modeled ^{36}Cl abundances show three distinct periods of fault activity during the past 14 kyr, with over 6 meters of displacement occurring during a 3 kyr time period in the middle Holocene. Smaller amounts of displacement occurred at 12 ± 2 kya and 1.5 ± 1.5 kya. The episodic behavior of the Nahef East fault indicates that the displacement rate of this fault system has varied through time.

1. Introduction

Few methods can decipher the seismic history and displacement rate of a fault if the only remaining evidence of seismic activity is a bedrock scarp [McCalpin, 1996]. Weathering features on limestone scarps may reflect relative ages of displacement events

[Stewart, 1996], but such features often cannot be used to resolve seismic history in detail sufficient to distinguish paleoseismic events or calculate recurrence intervals.

We have determined the displacement history of a limestone normal fault scarp located in northern Israel, using in-situ produced cosmogenic ^{36}Cl . The increasing precision of cosmogenic isotope measurements and continued refinement of ^{36}Cl depth-production models [Liu et al., 1994; Dep et al., 1994; Stone et al., 1996; Phillips et al., 1996; Stone et al., 1998] and production rates [Zreda et al., 1991; Stone et al., 1996, Phillips et al., 1996] allow estimation of the rate at which a limestone surface becomes exposed on Earth's surface due to normal faulting [Noller et al., 1996; Zreda and Noller, 1998]. The sampling, analytical, and numerical method detailed here has potential for constraining scarp exposure ages and fault displacement rates anywhere Ca-containing bedrock is exposed as a result of normal faulting.

In this study, we measured ^{36}Cl in 41 limestone samples taken from and near the Nahef East normal fault scarp, located in northern Israel (46 analyses total, including 5 replicates). Most of our samples are from a single scarp transect and are spaced closely downdip, every 30 cm. Using the geometry of the fault scarp and the chemical and isotopic data collected from these samples, we employ a numerical model to determine the faulting scenarios consistent with the measured ^{36}Cl abundances.

1.1 Study area

The Nahef East fault scarp is located in the Beit-Hakerem Valley, Galilee region, northern Israel (Figure 1). This region has been undergoing N-S extension since the Miocene, though there has been very little historic seismicity [Freund, 1965; Freund, 1970; Garfunkel et al., 1980; Ron et al., 1984; van Eck and Hofstetter, 1990]. The Nahef East fault scarp is one of several relatively short (2 to 6 km-long), en-echelon scarps that

extend sub-parallel to the large (700 meter-high) Zurim escarpment (Figures 1B and 1C). Morphometric analysis of Zurim Escarpment slope profiles indicates that it began forming c. 6 Mya and reached approximately today's relief by 4 Mya (Matmon et al., 1998). The small bedrock scarps, therefore, represent a relatively recent renewal of the extensional tectonic and seismic activity that has affected this region for the past few million years.

1.2 Fault The Nahef East fault scarp can be traced for about 5 km and its vertical throw varies from 1.5 to 11.1 meters (Figure 2). At its western edge, the fault is directly beneath the town of Nahef (population 4000). The footwall consists of variably dolomitized limestone of the Turonian to Cenomanian Sakhnin Formation; the hanging wall consists of Senonian chalk from the Mt. Scopus Group [Freund, 1965]. Based on the stratigraphic thicknesses of these two units, the total vertical offset on the Nahef East fault is 50 to 300 meters [Freund, 1959; Kafri, 1997]; however, only the last few meters of this offset is represented by today's topography. As is common in other carbonate fault scarp systems, displacement on the Nahef East scarp is distributed across more than one fault plane in places [Stewart and Hancock, 1991].

A critical consideration in this study is the process by which the scarp was exposed. For in-situ cosmogenic nuclides to provide paleoseismic information on a bedrock scarp, it is essential that the scarp was exposed due to faulting rather than other processes, such as differential erosion of the hanging wall. Field observations support exposure resulting from faulting rather than weathering. First, the surface drainage system in this Mediterranean zone (700 mm precipitation yr⁻¹ [Survey of Israel, 1985]) on the hanging wall chalk is poorly developed, especially near the sample transect, which is located near the drainage divide. There are no streams or stream channels in the vicinity, and surface flow from the steep slopes above the chalk enters the limestone karst surface. Second, near the sample transect, the fault bends into the footwall, offsetting the Sakhnin

limestone. This offset creates a sharp, 2 m-high limestone scarp that separates two limestone surfaces of equal composition and erodability. Finally, for the 9 m-high scarp to have been created by erosion within the past 14 kyr (as our dating shows below), the erosion rate of the chalk would have had to have been at least 750 m My^{-1} , over twenty times higher than the erosion rate of the limestone we measured (29 m My^{-1}).

1.2 Fault scarp dating and scarp-earthquake relationships

We use our numerical model to find faulting histories that result in ^{36}Cl abundances consistent with measured Nahef East fault scarp data. Using this technique, one can constrain the probable timing and magnitude of normal fault activity for faults that cannot be dated using standard paleoseismological methods [McCalpin, 1996]. Numerous researchers have measured normal fault scarp ages in sediments using methods such as scarp degradation modeling and dating of colluvial wedge sediments exposed in trenches [e.g. Wallace, 1977; Bucknam and Anderson, 1979; Mayer, 1984; Berryman and Beanland, 1991; Machette et al., 1991; McCalpin et al., 1993; McCalpin, 1996; Bell et al., 1999]; however, these methods cannot be applied to bedrock scarps. Studies on relative weathering patterns of bedrock scarps may be able to distinguish different seismic events, but do not provide sufficient age resolution for detailed paleoseismology studies [Stewart, 1996; Zreda and Noller, 1998]. Bedrock surfaces can, however, be dated using cosmogenic nuclides [e.g. Nishiizumi et al., 1991; Handwerger et al., 1999]. Paired with an interpretive numerical model, cosmogenic ^{36}Cl data can provide earthquake age and displacement constraints for bedrock scarps that lack any distinct weathering profiles.

Once the timing and size of faulting are constrained from ^{36}Cl data, we use empirical relationships between rupture characteristics (maximum displacement and

moment magnitude) to calculate possible earthquake moment magnitudes [Wells and Coppersmith, 1994; Bonilla et al., 1984]. Earthquake magnitudes we calculate are inherently minima because we have data from only one scarp transect; offset could have been larger elsewhere, where data were not collected.

1.3 Recurrence intervals, characteristic earthquakes, and fault segmentation

Paleoseismic information is often used to predict the timing, size, and location of future earthquakes [Schwartz and Coppersmith, 1984; McCalpin, 1996]. Several fault behavior models, including recurrence intervals, characteristic earthquakes, and fault segmentation, are used to constrain these parameters. The recurrence interval, or average time between earthquakes, is calculated by dividing the average displacement per event by the long-term seismic slip rates [Wallace, 1970]. Slip rates can be measured from offset geomorphic features or by dating individual earthquakes. However, if paleoseismic evidence indicates that earthquake activity was episodic or highly variable through time, an average recurrence interval becomes an ineffective parameter for prediction purposes [Sieh et al., 1989; Berryman and Beanland, 1991]. Earthquake size can be constrained using the characteristic earthquake model, posed by Schwartz and Coppersmith (1984). They suggest that earthquakes of a particular magnitude recur repeatedly on individual faults; if past earthquakes have all been of equal magnitude, it is likely that future earthquakes will be similarly sized.

Large fault systems are often divided into discrete fault *segments*, or sections of fault walls of the fault system. To measure surficial vertical displacement along the fault, we surveyed 30 cross sections, each 50 to 300 meters long and oriented perpendicular to and across the scarp (Figure 3). From these cross sections, we measured the vertical displacement along the fault scarp (Figures 2 and 4).

Large fault systems are often divided into discrete fault *segments*, or sections of fault walls of the fault system. To measure surficial vertical displacement along the fault, we surveyed 30 cross sections, each 50 to 300 meters long and oriented perpendicular to and across the scarp (Figure 3). From these cross sections, we measured the vertical displacement along the fault scarp (Figures 2 and 4).

Large fault systems are often divided into discrete fault *segments*, or sections of fault walls of the fault system. To measure surficial vertical displacement along the fault, we surveyed 30 cross sections, each 50 to 300 meters long and oriented perpendicular to and across the scarp (Figure 3). From these cross sections, we measured the vertical displacement along the fault scarp (Figures 2 and 4).

Large fault systems are often divided into discrete fault *segments*, or sections of fault walls of the fault system. To measure surficial vertical displacement along the fault, we surveyed 30 cross sections, each 50 to 300 meters long and oriented perpendicular to and across the scarp (Figure 3). From these cross sections, we measured the vertical displacement along the fault scarp (Figures 2 and 4).

White, 1989; de Polo et al., 1991; Machette et al., 1991; Crone and Haller, 1991; Wu and Bruhn, 1994; Koning and Pazzaglia, 1998]. Determining seismic risk from complex normal fault systems is difficult because extensive paleoseismic data are needed to determine the faulting behavior of each individual segment before the faulting behavior of the entire system can be understood.

To assess the seismic risk of a normal fault system accurately, one must know the slip rate, the average earthquake size, and the distribution of rupture among segments (if there are multiple segments). If the slip rate or earthquake magnitude vary through time, or if there are insufficient data from all segments in a fault system, it can be difficult or impossible to predict when or where the next earthquake will occur [Berryman and Beanland 1991; Koning and Pazzaglia, 1998]. However, if a long-term seismic pattern for a region can be detected, it may be possible to estimate the seismic risk of the region as a whole, if not for individual faults.

2. Methods

2.1 Field methods

In winter 1998, we measured the Nahef East fault geometry and collected samples. Using a Trimble 4400 real time kinematic (RTK) global positioning system (GPS), we surveyed several thousand topographic data points on both the hanging and foot walls of the fault system. To measure surficial vertical displacement along the fault, we surveyed 30 cross sections, each 50 to 300 meters long and oriented perpendicular to and across the scarp (Figure 3). From these cross sections, we measured the vertical displacement along the fault scarp (Figures 2 and 4).

We chose a sample location near the northwest end of the scarp (1260404 N, 180372 E, Israel Map Grid) (Figure 5). At this location, the scarp is planar, and displays only minor modification by weathering. This weathering includes rills ≤ 4 cm deep, as well as some pitting, but no block failure. In the sample location, the scarp is 9 vertical m high and dips 51° (Figures 2 and 4). Where we sampled, displacement is accommodated on a single fault plane.

Samples were taken from the scarp face at 30-cm downdip intervals using a rock drill (Table 1). Three samples were taken from beneath a 30 cm-thick piece of chalk covering the footwall, located at the base of the scarp (SG-030, SG-060 and SG-090) (Figure 4B). The extracted cores were 2.54 cm in diameter and ranged from 4- to 10-cm long. At each 30-cm interval, we took 3 or 4 cores resulting in ≥ 150 grams of sample. At two elevations on the scarp, we took a replicate set of samples about one meter to the west of the main sample transect (SG300R and SG600R). Two samples (SGTOP and the three TOP replicates), taken from the upper foot wall surface, were used to estimate the long-term erosion rate of the limestone (Figures 1 and 4). We also measured the density of a sample from the hanging wall chalk for cosmic-ray shielding calculations.

The thin (30 cm) chalk slab covering the lowest meter of the scarp, was removed to collect the lowest samples (SG-030, SG-060 and SG-090). This chalk slab extends in patches of roughly equal height (about one meter) for nearly a hundred meters of scarp length. This chalk slab is probably the result of the most recent surface rupture, where the fault plane extended through the chalk unit instead of breaking at the boundary between the chalk and the limestone (Figure 4).

2.2 Analytical methods

Four different analyses of the limestone samples are necessary in order to measure ^{36}Cl and parameterize ^{36}Cl production rates. Chlorine extraction procedures were modified from Stone et al. (1996). We processed samples in batches of eight, including two full procedural blanks in each batch. $^{36}\text{Cl}/\text{Cl}$ ratios of the AgCl precipitate from rock samples were measured using accelerator mass spectrometry (AMS) at Lawrence Livermore National Laboratory. These blanks have consistently low $^{36}\text{Cl}/\text{Cl}$ ratios (7.0×10^{-15} to 1.7×10^{-16}) compared to the measured sample ratios (7.1×10^{-13} to 1.0×10^{-13}) (Tables 1 and 2). Four full laboratory replicates (TOP250B, SG780D, SG540D, SG480D) were processed by dissolving the same rock in two different batches in order to determine measurement precision ($\mu = 74.1 \pm 6.8$, 39.4 ± 5.4 , 27.1 ± 2.4 , and 25.5 ± 2.8 , $\times 10^4$ atoms ^{36}Cl (gm rock) $^{-1}$, respectively) (Figure 6). SG-030 and SG-030b are two separate rock cores taken from the same position and processed separately ($\mu = 13.2 \pm 1.3 \times 10^4$ atoms ^{36}Cl (gm rock) $^{-1}$). TOP125 is a smaller grain-size rock aliquot from the same sample that produced TOP250A and TOP250B.

Total chloride in each sample was measured using mercury (II) thiocyanate absorbance spectroscopy [Florence and Farrar, 1971] with a Lachat Quik-Chem automated ion analyzer. The chloride concentrations of the samples were measured twice and calibrated with six internal standards via two different methods; hand-digitized peak area and the calibration internal to the Quik-Chem (also based on peak area). Blanks contained an average of $0.2 \pm 0.1 \mu\text{g g solution}^{-1}$ chloride. Chloride measured in the sample solutions was corrected for the amount of chloride contained in the batch-specific blanks.

Major element chemistry (Ca and Mg) was measured on dissolved rock aliquots using a Perkin-Elmer Optima 3000 inductively-coupled plasma atomic emission

spectrometer (ICPAE). Potassium was also measured, and was below detection limits in every sample, $< 0.1 \mu\text{g (g solution)}^{-1}$. Ca and K were each measured using a single wavelength (317.933 and 766.491 nanometers, respectively). Mg was quantified using four different wavelengths (279.079, 279.553, 280.270, and 285.213 nanometers); the reported Mg concentration for each sample is an average. Each sample was analyzed twice at two different dilutions; the low dilution samples were used to quantify Mg and K and the more highly diluted samples were used to quantify Ca. Each procedural blank was analyzed at the low dilution, and each contained less than 0.1% of the Ca and Mg measured in the rock samples. For each dilution, Ca and Mg values were corrected using a set of three internal standards. We used these ICPAE measurements of Ca and Mg and stoichiometric relationships to ensure the quality of our analyses. Whole-rock yields from the ICPAE data averaged $100.8 \pm 5.3\%$. Samples with a yield 5% greater or less than 100% were re-analyzed. The normalized amounts of Ca and Mg from the second analysis were similar to the original analysis, even if the yield was significantly different. We infer that the error was in dilution, not in the ICPAE measurement of Ca and Mg. We then normalized the calculated Ca and Mg content in each sample to the actual measured mass of dissolved rock, considering limestone stoichiometry. Normalized Ca and Mg contents of the three replicate samples agree well (average $1\sigma = 0.37\%$).

Trace elements (U, Th, B, Gd, Sm, and Li) were measured at Dartmouth College using ICP-mass spectrometry (ICP-MS). Separate rock aliquots for each sample were dissolved using ultra-pure HNO_3 in acid-washed HDPE vials. A blank of the ultra-pure acid and nanopure water was below detection limits for all analyzed elements.

3. Data (Wombeyan Park Reserve, Australia, 34°, 620 m asl) have ^{36}Cl concentrations of 93 to 124×10^4 atoms (gm rock) $^{-1}$, reflecting the limestone in Israel is eroding more quickly than the limestone in Australia [Stone et al., 1998].

3.1 Fault displacement data

Vertical displacement on the Nahef East fault scarp varies from 1.5 to 11.5 meters (Figure 2). The greatest amount of displacement occurs near the west end of the fault, where the trace is lost beneath the town of Nahef. In most places, the Nahef East fault separates the Cenomanian-Turonian carbonates from Senonian chalk; however, in places the fault bends and cuts through the Sakhnin Formation. Though the fault trace is usually a single surface, it sometimes becomes a fault array with smaller amounts of displacement distributed among several different planes.

3.2 Isotopic and chemical data

Isotopic, major, and minor element data were collected from the 41 samples, as well as 5 replicates (Table 1). ^{36}Cl is most abundant in the samples collected from the upper limestone surface (SGTOP, TOP250A TOP250B, and TOP125). In general, ^{36}Cl content decreases down the scarp, from 79 to 11×10^4 atoms (gm rock) $^{-1}$. Samples with a Ca content lower than their neighbors generally have a correspondingly low ^{36}Cl content (Table 1 and Figure 6). In order to determine lateral consistency of ^{36}Cl measurements, two sets of samples were taken one meter apart but at the same elevation (300 and 300R; 600 and 600R). Each pair has consistent ^{36}Cl values when corrected for Ca content ($\mu = 20 \pm 0.9$ and $27 \pm 0.8 \times 10^4$ atoms ^{36}Cl (gm Ca) $^{-1}$, respectively). The two rock samples taken from the upper limestone surface (SGTOP and the average of all TOP samples) agree fairly well, containing 70.2 ± 0.8 and $71.3 \pm 6.8 \times 10^4$ atoms ^{36}Cl (gm rock) $^{-1}$, respectively. In comparison, limestone samples from a surface of similar altitude and

latitude (Wombeyan Park Reserve, Australia, 34°, 620 m asl) have ^{36}Cl concentrations of 93 to 124 $\times 10^4$ atoms (gm rock) $^{-1}$, indicating the limestone in Israel is eroding more quickly than the limestone in Australia [Stone et al., 1998].

Mass percent Ca ranges from 25 to 40 ($\mu = 36.2 \pm 4.0\%$) and mass percent Mg ranges from 11 to 0.3 ($\mu = 2.8 \pm 2.9\%$). Chloride content in the rock samples ranges from 35 to 5 $\mu\text{g g}^{-1}$ ($\mu = 10.3 \pm 9.0 \mu\text{g g}^{-1}$). More than half of the samples have less than 10 $\mu\text{g g}^{-1}$ chloride. These chloride values are significantly less than those measured at the Wombeyan site, where several samples have $> 100 \mu\text{g g}^{-1}$ Cl [Stone et al., 1998]. Chloride in the Nahef East samples are also less than the average Cl concentration (150 $\mu\text{g g}^{-1}$) in carbonates worldwide [Fabryka-Martin, 1988]. Boron in the Nahef East fault scarp samples is low; samples average $0.7 \pm 0.8 \mu\text{g g}^{-1}$ and many are below ICP-MS detection limits. Sm, Gd, and Th are all $< 0.2 \mu\text{g g}^{-1}$. U ranges from 6.9 to 1.7 $\mu\text{g g}^{-1}$, averaging $4.3 \pm 0.9 \mu\text{g g}^{-1}$.

4. Numerical modeling of ^{36}Cl accumulation on an active fault scarp

To model ^{36}Cl accumulation beneath a dynamic surface, we must consider how its production rate is affected by sample depth and target chemistry. Chlorine-36 is produced in calcite by seven different cosmogenic and radiogenic reactions (Appendix 1). Reactions with calcium include spallation of ^{40}Ca by neutrons and negative muon capture by ^{40}Ca [Stone et al., 1996; Stone et al., 1998]. Five different reactions create thermal neutrons for capture by ^{35}Cl : spallation by secondary neutrons, muon capture, gamma radiation from fast muons, (α, n) reactions from U and Th decay, and ^{238}U -fission [Fabryka-Martin, 1988; Liu et al., 1994]. Each of these reactions have different relationships between chemistry, shielding, and production rate (Figure 7). Because of the

low Cl content of most samples, the ^{40}Ca reactions (spallation and muon capture) dominate ^{36}Cl production at and below the surface.

Because of the complexity of sub-surface ^{36}Cl accumulation beneath an active normal fault, measured nuclide abundances cannot be resolved into a unique displacement history using the analytical expressions typically employed for surface exposure dating. Therefore, we have created a numerical model, written in *MATLAB 5.6*, that calculates ^{36}Cl accumulation on the scarp face under a variety of erosion and displacement scenarios. This model numerically integrates the different ^{36}Cl production rates for each sample as they become exposed on the scarp face, integrating over ten year time steps. The model specifically considers the geometry and chemistry of each sample collected from the Nahef East fault scarp, as well as the erosion rate calculated from the upper surface samples. The *MATLAB 5.6* model can be downloaded via FTP from geology.uvm.edu. To evaluate the validity of each scenario, model ^{36}Cl values for each scenario are compared to measured sample values. We find that there are numerous different displacement histories for the Nahef East normal fault that are consistent with the measured nuclide abundances

4.1 Steady-state erosion rate of upper limestone surface and pre-faulting nuclide abundance

The ^{36}Cl inventory on a steadily-eroding surface is in equilibrium with ^{36}Cl production and nuclide loss by erosion and radio-decay (Figure 8) [Dockhorn et al., 1991; Bierman et al., 1995]. We have calculated iteratively ^{36}Cl concentrations expected in the two upper surface samples for different erosion rates until the calculated abundance of ^{36}Cl is equal to the average ^{36}Cl content measured in both rock samples, including the

three replicates ($71 \pm 6 \times 10^4$ atoms (gm rock)⁻¹). Such a calculation suggests that the upper limestone surface is eroding 29 ± 2 m My⁻¹ (Appendix 1).

To calculate the accumulation of ³⁶Cl on the Nahef fault scarp during faulting, we first estimate the ³⁶Cl concentration of each sample before displacement begins. Using the calculated steady-state erosion rate (29 m My⁻¹) and the equations described in Appendix 1, we solve for the initial ³⁶Cl concentrations in each sample, given each samples' depth below the surface at the start of faulting. Such calculations assume that, before faulting begins, the samples are brought towards the surface beneath a steadily-eroding, horizontal rock-air interface. The numerical model also contains a simple geometric correction for sample thickness (thickness = 5 ± 1 cm), and scales production rates to the altitude and latitude of the sample locality (33°, 300 m) [Lal, 1988].

4.2 ³⁶Cl accumulation on tilted surfaces

Nuclide production rates on tilted surfaces are less than production rates on horizontal surfaces. A tilted surface receives cosmic rays directly from only a fraction of the sky. For example, a vertical cliff will receive direct cosmic rays from one-half the hemisphere; the production rate of cosmogenic nuclides on a vertical surface is therefore one-half that of a horizontal surface. The neutron flux has an angular intensity that varies due to atmospheric thickness, and the muon flux varies angularly both in intensity and energy spectrum. A proportion of the cosmic ray flux will strike a tilted surface directly, while cosmic rays from the remaining portion of the sky can travel through the "back side" e.g., through the footwall of a normal fault scarp, before reacting with rock on the scarp surface. The fraction of cosmic-rays interacting directly with a tilted surface is a function of the surface angle and the angle-flux relationships for each of the different cosmic ray particles [Stone et al., 1998; Dunne et al., 1999].

The Nahef East fault scarp dips 51° at the sample location (Figure 4). Based on the surface angle/neutron flux relationships, 88.5% of neutrons travel through the chalk or strike the surface directly, and the remaining 11.5% travel through the limestone before reaching the surface [J. Stone, pers. comm, 1999]. The tilt scaling for muons is more complicated than the scaling for neutrons because muons hitting Earth's surface vary in both abundance and energy depending on the incidence angle. More muons strike Earth's surface from the zenith, but muons arriving from the horizon have higher energies and can therefore travel further underground before stopping [Stone et al., 1998; Crookes and Rastin, 1973; Bilokon et al., 1989]. Geometric calculations were made to correct for ^{36}Cl production rates from muons on tilted surfaces based on the muon flux information found in Stone et al. (1998). Based on these calculations, approximately 90.5% of muons reaching the scarp surface had to travel first through the hanging wall, while only 9.5% must first travel through the footwall.

4.3 ^{36}Cl accumulation during faulting

We have constructed our ^{36}Cl accumulation model with the premise that cosmic rays travel through both the hanging and foot walls to reach the fault scarp surface to dose the samples we later collected. The shielding depth as a function of time with respect to the hanging wall (chalk) is dependent on both the rate of chalk erosion (which we assume to be the same as the limestone erosion rate) and fault displacement because the chalk is moving down to reveal rock on the scarp face. The model does not take into account the slab of chalk covering the lowest meter of the scarp; its presence slightly reduces ^{36}Cl concentrations in the lowest three samples. The shielding depth with respect to the foot wall (limestone) is dependent only on the erosion rate because rock on the scarp face does not change position with respect to the upper limestone surface when

displacement occurs (Figure 9). Because of the small amount of weathering observed on the scarp face, we assume that the scarp face itself does not erode.

Considering the depth dependence of each of the seven different production pathways detailed in Appendix 1, the model calculates the accumulation of ^{36}Cl throughout every displacement history. Each history is unique in terms of event magnitude and age. Every model run results in the observed total displacement (9 m) and generates a ^{36}Cl abundance value for each sample on the scarp.

4.4 Model results

We have generated six distinct series of displacement scenarios, differing in the number of events used to generate the observed displacement ($n = 1$ to 6). Within each series, event sizes are identical. We varied the timing of events in each series in an attempt to match the measured data (within the 2σ error bounds from the accelerator analyses). The smallest time interval between events was 500 years. We calculated a “goodness of fit” parameter (χ^2) for each scenario by summing the absolute difference between model and measured ^{36}Cl values. We have designated a 95% confidence level for the entire profile by summing the 2σ error limits for the samples. Therefore, all displacement histories resulting in a χ^2 less than the calculated 95% confidence limit are considered viable displacement histories. Several samples were excluded from this analysis, including the samples taken from the upper limestone surface (these samples were never affected by faulting), and three laboratory replicates (SG780D, SG540D, and SG480D). These replicates never closely matched in scenarios that fit most other points quite well.

Seven and fifteen scenarios were run for the one- and two-event series, respectively, none of which produced a ^{36}Cl profile resulting in an acceptable χ^2 value.

We conclude from these results that the scarp probably formed in more than two events. We ran 15 scenarios for the three-event series, resulting in six scenarios within the error limit. All three-event scenarios generate ^{36}Cl concentrations that fit poorly the top and bottom of the scarp profile. This poor fit leads us to believe that the scarp probably records more than three events. For the four-, five-, and six-event series, we ran 180, 205 and 235 scenarios, respectively; the vast majority of these scenarios fit within 95% confidence bounds.

A histogram of the number of scenarios ($4 \leq n \leq 6$) containing events occurring in different 500-year intervals indicate that displacement events occur in three discrete time periods (Figure 10). The best-fitting 25% of acceptable histories in each series help constrain the boundaries of these three time periods (Figure 10). The best-fit histories from the different series ($n > 3$) strongly suggest three distinct periods of seismic activity and a variable displacement rate on the Nahef East fault (Figure 11). Displacement scenarios resulting from a single event or steady-state creep throughout the past 15 kyr result in model ^{36}Cl values that are clearly less consistent with measured data than the model results from the best-fit six-event scenario (Figure 12).

The lowest x^2 value for each series indicates that the overall degree of fit can become markedly better when the number of modeled events increases from one to five, but the difference in the lowest x^2 value between the five- and six-event series is minor in comparison (Figure 13). This result may indicate that increasing the number of events further, at least while retaining a 500 year minimum time interval between events, will not necessarily result in more precisely defined displacement histories.

5 Discussion

^{36}Cl analysis of Nahef East fault scarp samples constrains the fault's seismic history and earthquake potential. This information allows us to consider the uplift pattern of the Zurim Escarpment and the applicability of recurrence interval models for fault behavior in extensional terranes.

5.1 Nahef East fault behavior deduced from ^{36}Cl data and supporting evidence for the timing of fault motion

Regardless of whether the four-, five- or six-event scenario is considered, it appears that the Nahef East fault has undergone three distinct periods of seismic activity (Figures 10 and 11). The slip rate on the Nahef East fault has varied through time, with a distinct peak in the rate of surface offset occurring in the middle Holocene (4 to 7 kya) (Figure 10). There were lesser but significant periods of movement in the late Pleistocene (~12 kya) and late Holocene (~1.5 kya) as well. Our finding is not unique; many other paleoseismic studies have found episodic or clustering behavior in fault systems [e.g. Sieh et al., 1989; Schwartz, 1989; Niemi and Hall, 1992; Grant and Sieh, 1994].

Strong supporting evidence of significant middle-Holocene earthquake activity in the immediate area of the Nahef East fault was recently discovered in a cave on the Zurim Escarpment. This cave, located only 4 km to the north of the Nahef East fault, contains earthquake-damaged artifacts and human remains of the Chalcolithic era (6000 to 7000 BP). U-Th dating of samples collected from the bases of stalagmites found on cave debris, currently thought to be coseismic; dating indicates that strong shaking and subsequent damage occurred just prior to 6200 BP [M. Bar-Matthews, pers. comm, 1999].

The presence of the discontinuous, one-meter-high chalk slab covering the base of the scarp supports our ^{36}Cl -based inference of a late Holocene earthquake. This slab could represent the most recent motion on the Nahef East fault; during this last displacement event, the fault plane extended through the chalk instead of at the border between the chalk and the limestone. In order for this chalk slab to still be preserved on the scarp face, it only needs to have resisted erosion for 1.5 kyr.

5.2 Testing models of fault behavior

Nuclide data from the Nahef East fault indicate that the slip rate on this particular segment has varied greatly during the past 14 kyr. The simplest models of earthquake recurrence assume that slip rates remain constant through time; strain builds at a constant rate and is released periodically (as an earthquake) in either a time-predictable or slip-predictable manner [Shimazaki and Nakata, 1980]. Because the behavior of the Nahef East fault violates the constant slip assumption, there is not a single, average recurrence interval that accurately models earthquake occurrence through time. However, the three periods of fault activity appear to be relatively evenly-spaced (though the quiescent interval is different for each different series of displacement scenarios), allowing us to quantify the average amount of time that passes between active episodes (Figures 10 and 11). The average quiescent interval for the six event series is 4.1 ± 1.6 kyr.

Another widely applied earthquake model considers that, "individual faults and fault segments tend to generate essentially same size or characteristic earthquakes having a relatively narrow range of magnitudes near the maximum," [Schwartz and Coppersmith, 1984]. This characteristic earthquake model proposes that rupture occurs when the fault strain reaches a fixed intensity, resulting in an earthquake of a correspondingly fixed magnitude [Schwartz and Coppersmith, 1984; Hecker and

Schwartz, 1994]. The characteristic earthquake model does not assume a constant slip rate; if the slip rate varies through time, the recurrence interval between same-size earthquakes will vary correspondingly, such as our data show. Evidence from other regions indicate that earthquake size for intraplate normal fault systems is too variable to show characteristic earthquake behavior [Berryman and Beanland, 1991]. Our model displacement histories utilize constant earthquake size and are able to produce model ^{36}Cl values within 95% confidence limits. However, we can increase the displacement of a single mid-Holocene event to nearly 4.5 meters, or create clusters of small (10 cm) events within 500-year periods and still generate model scenarios within 95% confidence limits (these scenarios continue to result in the same three distinct periods of activity as the same-size models). Because multiple displacement scenarios are consistent with measured data, we cannot verify or refute the characteristic earthquake model for the Nahef East Fault.

5.3 The role of the Nahef East fault in the evolution of the Zurim Escarpment

Our numerical model allows us to focus on understanding the temporal pattern of past fault activity, and how it relates to both the development of the Zurim Escarpment and the development of the relatively young fault scarps seen today. The Nahef East fault is the youngest-looking (least weathered) of several similarly-sized and similarly-oriented fault scarps on the Zurim Escarpment, each separated from the other by structural gaps (Figure 1). The majority of the Zurim Escarpment topography was built between 6 and 4 Mya by extensional activity on these faults [Matmon et al., 1998]. If we calculate an average displacement rate through time for the Nahef East fault scarp, assume that earlier faulting on the Zurim Escarpment occurred in a similar manner, and consider the long-

term erosion rate of the bedrock in the region, we can estimate the growth rate of the escarpment as a geomorphic feature.

Based on our best-fit histories from the four-, five-, and six-event series, it took between 10 and 12 kyr for the Nahef East fault scarp to form. Maximum and minimum average rock displacement rates calculated from these values are 0.9 to 0.75 m kyr⁻¹, respectively. If uplift on the escarpment occurred at the same average displacement rate as the Nahef East fault, 700 m of relief could be built in as few as 0.8 to 1.0 My (including the 29 m My⁻¹ lost to erosion); these recent displacement rates are similar to the rates required to form the Zurim escarpment between 6 and 4 Mya [Matmon et al., 1998].

There are several short-term (tens of thousands of years) patterns of tectonic activity that could result in the inferred displacement history of the Nahef East fault scarp, the presence of other, more highly degraded scarps in the near vicinity, and the observation that there has been no recorded seismic activity on any faults in the region (Figure 14). It is clear from the Nahef East fault data that the displacement rate of a single fault varies through time. If the overall displacement rate along the Zurim escarpment were constant, the variability of displacement on single scarps could be explained by activity being accommodated on other segments. However, if this were the case, displacement would be taking place somewhere in the region today (Figure 14A). The absence of any recorded seismicity in a long historic record implies that the overall displacement and uplift rates in fact vary through time.

On a 10 kyr timescale, the variation in displacement rate on the Nahef East fault appears to be episodic, with episodes of seismic activity separated by a few thousand years of quiescence. The sizes of these episodes differ, with the middle-Holocene episode incorporating greater and more rapid surface rupture than the late Pleistocene or late Holocene deformation periods. There are several possible explanations for the fluctuation

of seismic activity on this single segment. The Nahef East fault segment could have a distinct life cycle, with faulting beginning slowly, increasing to a peak displacement rate in mid-cycle, then decreasing until the segment is no longer active (Figure 14B). Fault motion is then transferred elsewhere, possibly after some period of quiescence while strain builds again. If this hypothesis is correct, then the Zurim Escarpment is now in that period of quiescence and the Nahef East fault does not pose a significant seismic risk (if displacement were to occur again, it would be less intense than the late Holocene seismic episode). Conversely, offset could occur on different segments at the same time; when the displacement rate is lower on the Nahef East fault, motion is, at the same time, accommodated on different faults elsewhere in the region (Figure 14A). Or, a combination of these two mechanisms could be taking place, with the displacement on individual faults fluctuating through time, and occasional accommodation of displacement among different segments (Figure 14C). We prefer the first and last explanations because they are both supported by the observation that there is no seismicity today, and that the scarps along the Zurim Escarpment range in a continuum from very fresh (Nahef East fault) to extremely weathered (other nearby scarps).

The amount of relief and stratigraphic throw shown by the faults on the Zurim Escarpment hints at a longer-wavelength periodicity in seismic activity. As with many escarpments, the cumulative vertical relief of the various scarps (< 50 m) does not come close to the vertical relief of the Zurim Escarpment (700 m). This discrepancy supports the morphometric evidence that the majority of escarpment topography formed long ago, creating scarps that had 4 My to erode before the recent renewal of tectonic activity created the scarps seen today [Matmon et al., 1998]. Based on stratigraphic offset, there are at least 50 meters of vertical displacement between units in the hanging wall and footwall of the Nahef East fault, five times the surface offset observed today. The Nahef

East fault must have been active in the past, forming scarps that eroded before the next long-term cycle of seismic activity began.

5.4 Seismic hazard of the Zurim Escarpment fault system

Earthquakes occurring in northern Israel (on the Dead Sea Transform fault, not on extensional faults) in recent centuries (e.g. the $M = 6.4$ Safed earthquake of 1837, and the $M = 6.2$ Jericho earthquake of 1927) caused serious damage in populated regions [van Eck and Hofstetter, 1990; Ben-Menahem, 1981]. Considering that over 80,000 people live within 30 km of the Zurim Escarpment (and the many other similar escarpments located throughout the Galilee), the potential for severe damage and loss of life is quite high.

Characteristics of Nahef East fault behavior indicate that the Zurim Escarpment is an area of potential seismic hazard, particularly in the long term. Rapid, large-scale displacement has occurred in the region. It is also evident (especially from the size and morphology of the escarpment and the presence of old, weathered scarps) that the region has been seismically active for 10^5 to 10^6 years [Matmon et al., 1998]. These two observations indicate that seismic activity is likely to occur in the future. However, the region is currently seismically quiescent. Our data suggest that several thousand years pass between active episodes on the Nahef East fault, a single segment on the Zurim Escarpment. However, we do not know how much time passes between active episodes on different segments. Once fault motion begins again, however, our data and the discovery of the rapid, mid-Holocene displacement suggest that more earthquakes could soon follow.

As stated before, the ^{36}Cl data are consistent with many different surface rupture scenarios. However, all scenarios consistent with the measured ^{36}Cl data suggest that a

great amount of displacement (up to 6 m) occurred during a 3000-year period in the middle Holocene. Using the maximum vertical displacement method for calculating earthquake magnitudes, described in Wells and Coppersmith (1994), and the largest individual displacement event that still results in a good-fitting ^{36}Cl profile (4.7 m), the resulting maximum earthquake on the Nahef East fault would be $M = 7.1$ (moment magnitude scale). An earthquake resulting from the events in the six-event series (1.6 m) would have a moment magnitude of 6.8.

5.5 Prospects for cosmogenic isotope dating

The paucity of pre-historic earthquake displacement data limit our ability to determine seismic risk and study fault behavior in active fault systems [Berryman and Beanland, 1991; dePolo et al., 1991; Stewart, 1996]. This and other studies show that measuring ^{36}Cl in samples collected from Ca- or Cl-rich bedrock scarps is an effective method for determining the age of motion on normal faults [Noller et al., 1996; Zreda and Noller, 1998]. Fault scarp dating is not limited to ^{36}Cl ; bedrock scarps containing quartz (i.e. sandstone, granite, quartzite, or rhyolite) could be dated using ^{10}Be and ^{26}Al [e.g. Nishiizumi et al., 1991; Bierman, 1994]. Scarps exposing olivine or pyroxene could be dated using ^3He [Kurz et al., 1990]. Cosmogenic ^{14}C has also been applied to fault scarps in carbonate rocks [Handwerger et al., 1999]. Any planar, uneroded bedrock scarp with a simple exposure history (without burial or non-tectonic exhumation) is a candidate for cosmogenic nuclide dating.

Provided that exposure histories are simple and scarps are in good condition, cosmogenic dating will determine scarp ages more precisely and more accurately than measuring relative weathering characteristics. Nuclide measurement can constrain the timing of displacement, even when geomorphic clues (such as distinct weathering

horizons) are absent. If discrete displacement events can be seen in the morphology of the scarp face, modeling the ages of events from nuclide abundances becomes much simpler because displacement size can be estimated independently. However, a model is still required to calculate sub-surface isotope accumulation during the development of the scarp. Calculating ages directly from the scarp surface, without such a model, will overestimate the age of rupture events, especially for carbonate rocks in which subsurface production from muons can account for a large portion of the measured ^{36}Cl .

5.6 Implications for paleoseismology

Detailed and precise nuclide dating of fault scarps will greatly improve models of fault segmentation and fault behavior. As Sieh et al. [1989] concluded in their study of the Pallet Creek site, California, detailed paleoseismic chronologies do not always allow for more accurate recurrence interval calculations or seismic risk prediction, because they tend to show the irregularity inherent to natural systems. Detailed chronologies do, however, allow study of the temporal and spatial behavior of complex fault systems. An exciting future prospect for nuclide dating would be to obtain nuclide profiles from many nearby scarps to determine the temporal and spatial distribution of fault activity along a segmented fault system (Figure 14).

Understanding fault behavior and segmentation characteristics depends upon knowing which segments ruptured at what time. The study of fault and earthquake segmentation is limited by the resolution and accuracy of fault-scarp dating and resultant paleoseismic investigations [McCalpin, 1996]. Fault-behavior models and the concepts of earthquake and fault segmentation provide us with a framework for understanding earthquake recurrence and seismic risk; however, it appears that fault systems need to be analyzed individually before evaluating them in the context of a particular model. Several

studies have shown that fault systems do not all display characteristic behavior, and that earthquake ruptures are not always limited to fault segments defined from structural and paleoseismic criteria [Berryman and Beanland, 1991; dePolo et al, 1991; Hecker and Schwartz, 1994]. Our data show that in appropriate settings, cosmogenic nuclides can be used to provide the temporal and spatial dating resolution needed to understand better the long-term behavior of individual normal fault systems in complex extensional environments.

Acknowledgements

This research was funded by Hebrew University, an Israeli Atomic Energy Commission grant to Enzel, a University of Vermont SUGR/FAME grant to Gran and Bierman, and an NSF Graduate Research Fellowship to Gran. C. Massey and D. Gluek assisted in the field. ICP-MS samples were run by B. Klaue at Dartmouth College, with support from J. Blum. J. Larsen assisted with Cl and ICP analyses. ³⁶Cl measurements were made at Lawrence Livermore National Laboratory (under DOE contract W-7405-ENG-48). J. Stone greatly assisted with the geometric and chemistry corrections for the numerical model.

References

- Ben-Menahem, A., Variation of slip and creep along the Levant Rift over the past 4500 years. *Tectonophysics*, 80, 183-197, 1981.
- Bell, J. W., C. M. dePolo, A. R. Ramelli, A. M. Sarna-Wojcicki, and C. E. Meyer, Surface faulting and paleoseismic history of the 1932 Cedar Mountain Earthquake area, west-central Nevada, and implications for modern tectonics of the Walker Lane. *Geological Society of America Bulletin*, 111, 791-807, 1999.
- Berryman, K. R., and S. Beanland, Variation in fault behavior in different tectonic provinces of New Zealand. *Journal of Structural Geology*, 13, 177-189, 1991.

- Bierman, P. R., Using in situ cosmogenic isotopes to estimate rates of landscape evolution: a review from the geomorphic perspective. *Journal of Geophysical Research*, 99, 13885-13896, 1994.
- Bierman, P. R., A. Gillespie, M. Caffee, and D. Elmore, Estimating erosion rates and exposure ages with ^{36}Cl produced by neutron activation. *Geochimica et Cosmochimica Acta*, 59, 3779-3798, 1995.
- Bilokon, H., G. Cini-Castagnoli, A. Castellina, B. Piazzoli, G. Mannocci, E. Meroni, P. Picchi, and S. Vernetto, Flux of the vertical negative muons stopping at depths 0.35 –1000 hg/cm². *Journal of Geophysical Research*, 94, 12145-12152, 1989.
- Bonilla, M. G., R. K. Mark, and J. J. Lienkaemper, Statistical relations among earthquake magnitude, surface rupture length, and surface fault displacement. *Bulletin of the Seismological Society of America*, 74, 2379-2411, 1984.
- Bucknam, R. C., and R. E. Anderson, Estimation of fault scarp ages from a scarp-height-slope-angle relationship. *Geology*, 7, 11-14, 1979.
- Charalambus, S., Nuclear transmutation by negative stopped muons and the activity induced by cosmic-ray muons. *Nuclear Physics*, A166, 145-161, 1971.
- Crone, A. J., and M. N. Machette, Surface faulting accompanying the Borah Peak earthquake, central Idaho. *Bulletin of the Seismological Society of America*, 77, 737-770, 1987.
- Crone, A. J., and K. M. Haller, Segmentation and the coseismic behavior of Basin and Range normal faults: examples from east-central Idaho and southwestern Montana, USA. *Journal of Structural Geology*, 13, 151-164, 1991.
- Crookes, J. N., and B. C. Rastin, The absolute intensity of muons at 31.6 hg cm⁻² below sea level. *Nuclear Physics*, B58, 93-109, 1973.
- Dep, L., D. Elmore, J. Fabryka-Martin, J. Masarik, and R. Reedy, Production rate systematics of in-situ-produced cosmogenic nuclides in terrestrial rocks: monte carlo approach of investigating $^{35}\text{Cl}(n,\gamma)^{36}\text{Cl}$. *Nuclear Instruments and Methods in Physics Research*, B92, 321-325, 1994.
- dePolo, C. M., D. G. Clark, D. B. Slemmons, and A. R. Ramelli, Historic surface faulting in the Basin and Range province, western North America: implications for fault segmentation. *Journal of Structural Geology*, 13, 123-136, 1991.
- Dockhorn, B., S. Neumaier, F. J. Hartmann, C. Petitjean, H. Faestermann, G. Korschinek, H. Morinaga, and E. Nolte, Determination of erosion rates with cosmic ray produced ^{36}Cl . *Hadrons and Nuclei*, 341, 117-119, 1991.
- Dunne, J., D. Elmore, and P. Muzikar, Scaling factors for the rates of production of cosmogenic nuclides for geometric shielding and attenuation at depth on sloped surfaces. *Geomorphology*, 27, 3-12, 1999.
- Fabryka-Martin, J. T., Production of radionuclides in the Earth and their hydrogeologic significance, with emphasis on chlorine-36 and iodine-129. Ph.D. dissertation, University of Arizona, Tucson, 400 p., 1988.
- Florence, T. M., and Y. J. Farrar, Spectrophotometric determination of chloride at the parts-per-billion level by mercury (II) thiocyanate method. *Analytical Chimica Acta*, 54, 373-377, 1971.

- Freund, R., On the stratigraphy and tectonics of the Upper Cretaceous in the western Galilee, *Bulletin of the Research Council of Israel*, G8, 43-50, 1959.
- Freund, R., A model of the structural development of Israel and adjacent areas since Upper Cretaceous times. *Geology Magazine*, 102, 189-205, 1965.
- Freund, R., The geometry of faulting in the Galilee. *Israel Journal of Earth Sciences*, 19, 117-140, 1970.
- Garfunkel, Z., I. Zak, and R. Freund, Active faulting in the Dead Sea Rift. *Tectonophysics*, 80, 1-26, 1980.
- Grant, L. B., and K. Sieh, Paleoseismic evidence of clustered earthquakes on the San Andreas fault in the Carizzo Plain, California. *Journal of Geophysical Research*, 99, 6819-6841, 1994.
- Handwerker, D. A., T. E. Cerling, and R. L. Bruhn, Cosmogenic ^{14}C in carbonate rocks. *Geomorphology*, 27, 13-24, 1999.
- Hecker, S., and D. P. Schwartz, The characteristic earthquake revisited: Geological evidence of the size and location of successive earthquakes on large faults. *U.S. Geological Survey Open File Report*, 94-568, 79-80, 1994.
- Jackson, J. A., and N. J. White, Normal faulting in the upper continental crust. *Journal of Structural Geology*, 11, 15-36, 1989.
- Kafri, U., Neogene to Quaternary drainage systems and their relationship to young tectonics: lower Galilee, Israel. *Geological Survey of Israel*, Report GSI/1/97, 1997.
- Knight, J. D., C. J. Orth, M. E. Schillaci, R. A. Naumann, F. J. Hartmann, J. J. Reidy, and H. Schnewly, Coulomb capture ratios of negative muons in $\text{N}_2 + \text{O}_2$, NO and CO. *Physics Letters*, 79A, 377-379, 1980.
- Koning, D. J., and F. J. Pazzaglia, Paleoseismicity, fault segmentation and persistence of mountain-front landforms in a continental rift setting, Alamogordo fault, southern New Mexico. *Geological Society of America, Abstracts with Programs*, 30, A329, 1998.
- Kurz, M. D., D. Colander, T. W. Trull, R. B. Moore, and K. O'Brien, Cosmic ray exposure dating with in situ produced cosmogenic ^3He : results from young Hawaiian lava flows. *Earth and Planetary Science Letters*, 97, 177-189, 1990.
- Lal, D., In situ-produced cosmogenic isotopes in terrestrial rocks. *Annual Reviews of Earth and Planetary Science*, 16, 355-388, 1988.
- Lal, D., Cosmic ray labeling of erosion surfaces: In situ production rates and erosion models. *Earth and Planetary Science Letters*, 104, 424-439, 1991.
- Liu, Beiling, F. M. Phillips, J. T. Fabryka-Martin, M. M. Fowler, and W. D. Stone, Cosmogenic ^{36}Cl accumulation in unstable landforms 1. Effects of the thermal neutron distribution. *Water Resources Research*, 30, 3115-3125, 1994.
- Machette, M. N., S. F. Personius, A. R. Nelson, D. P. Schwartz, and W. R. Lund, The Wasatch fault zone, Utah—segmentation and history of Holocene earthquakes. *Journal of Structural Geology*, 13, 137-149, 1991.
- Maserik, J., and R. C. Reedy, Terrestrial cosmogenic-nuclide production systematics calculated from numerical simulations. *Earth and Planetary Science Letters*, 136, 381-396, 1995.

- Matmon, A., E. Zilberman, and Y. Enzel, Morphometric analysis for determining the age of escarpments: an example from the Galilee, northern Israel. *Geological Survey of Israel*, Report GSI/31/98, 1998.
- Matmon, A., Y. Enzel, E. Zilberman, and A. Heimann, Late Pliocene and Pleistocene reversal of drainage systems in northern Israel: tectonic implications. *Geomorphology*, 28, 43-59, 1999.
- Mayer, L., Dating Quaternary fault scarps in alluvium using morphological parameters. *Quaternary Research*, 22, 300-313, 1984.
- McCalpin, J. P., *Paleoseismology*. Academic Press: San Diego. 588 p., 1996.
- McCalpin, J. P., W. Zuchiewicz, and L. C. A. Jones, Sedimentology of fault-scarp-derived colluvium from the 1983 Borah Peak rupture, central Idaho. *Journal of Sedimentary Petrology*, 63, 120-130, 1993.
- Niemi, T. M., and N. T. Hall, Late Holocene slip rate and recurrence of great earthquakes on the San Andreas fault in northern California. *Geology*, 20, 195-198, 1992.
- Nishiizumi, K., C. P. Kohl, J. R. Arnold, J. Klein, D. Fink, and R. Middleton, Cosmic ray produced ^{10}Be and ^{26}Al in Antarctic rocks: exposure and erosion history. *Earth and Planetary Science Letters*, 104, 440-454, 1991.
- Noller, J., M. G. Zreda, and W. R. Lettis, Use of cosmogenic Cl-36 to date late Quaternary activity of the Hebgen Lake Fault, Montana. *Geological Society of America, Abstracts with Programs*, 28, 300, 1996
- Phillips, F. M., M. G. Zreda, M. R. Flinsch, D. Elmore, and P. Sharma, A reevaluation of cosmogenic ^{36}Cl production rates in terrestrial rocks. *Geophysical Research Letters*, 23, 949-951, 1996.
- Ron, H., R. Freund, Z. Garfunkel, and Z. Nur, Block rotation by strike-slip faulting: structural and paleomagnetic evidence (Israel). *Journal of Geophysical Research*, 89, 6256-6270, 1984.
- Schwartz, D. P., and K. J. Coppersmith, Fault behavior and characteristic earthquakes: examples from the Wasatch and San Andreas fault zones. *Journal of Geophysical Research*, 89, 5681-5698, 1984.
- Schwartz, D. P., Paleoseismicity, persistence of segments, and temporal clustering of earthquakes; examples from the San Andreas, Wasatch, and Lost River fault zones. In: *Proceedings of Conference XLV; a workshop on fault segmentation and controls of rupture initiation and termination*, USGS Open File Report, 361-375, 1989.
- Shimazaki, K., and T. Nakata, Time-predictable recurrence model for large earthquakes. *Geophysical Research Letters*, 7, 279-282, 1980.
- Sieh, K., M. Stuiver, and D. Brillinger, A more precise chronology of earthquakes produced by the San Andreas Fault in southern California. *Journal of Geophysical Research*, 94, 603-623, 1989.
- Spannagel, G., and E. L. Fireman, Stopping rate of negative cosmic ray muons near sea level. *Journal of Geophysical Research*, 77, 5351-5359, 1972.
- Stewart, I. S., and P. L. Hancock, Neotectonic normal fault zones in the Aegean region. *Journal of Structural Geology*, 13, 191-204, 1991.

- Stewart, I. S., A rough guide to limestone fault scarps. *Journal of Structural Geology*, 18, 1259-1264, 1996.
- Stone, J. O., G. L. Allan, L. K. Fifield, and R. G. Cresswell, Cosmogenic chlorine-36 from calcium spallation. *Geochimica et Cosmochimica Acta*, 60, 679-692, 1996.
- Stone, J. O., J. M. Evans, L. K. Fifield, G. L. Allan, and R. G. Cresswell, Cosmogenic chlorine-36 production in calcite by muons. *Geochimica et Cosmochimica Acta*, 62, 433-454, 1998.
- Survey of Israel, *Atlas of Israel: Cartography, Physical and Human Geography*. Macmillian Publishing Company: New York, 1985.
- Swanson, T. W., R. C. Finkel, L. Harris, and J. Southon, Application of ^{36}Cl dating based on the deglaciation history of the Cordilleran ice sheet in Washington and British Columbia. *Geological Society of America, Abstracts with Programs*, 26, 512 p., 1994.
- van Eck, T., and A. Hofstetter, Fault geometry and spatial clustering of micro earthquakes along the Dead Sea-Jordan rift fault zone. *Tectonophysics*, 180, 15-27, 1990.
- von Egidy, T., and F. J. Hartmann, Average muonic coulomb capture probabilities for sixty-five elements. *Physics Review A*, 26, 2355-2360, 1982.
- Wallace, R. E., Earthquake recurrence intervals on the San Andreas fault. *Geological Society of America Bulletin*, 81, 2875-2890, 1970.
- Wallace, R. E., Profiles and ages of young fault scarps, north-central Nevada. *Geological Society of America Bulletin*, 88, 1267-1281, 1977.
- Wells, D. L., and K. J. Coppersmith, Empirical relationships among magnitude, rupture length, rupture area, and surface displacement. *Bulletin of the Seismological Society of America*, 82, 974-1002, 1994.
- Wu, D., and R. L. Bruhn, Geometry and kinematics of active normal faults, South Oquirrh Mountains, Utah: implications for fault growth. *Journal of Structural Geology*, 16, 1061-1075, 1994.
- Yokoyama, Y., J. L. Reyss, and F. Guichard, Production of radionuclides by cosmic rays at mountain altitudes. *Earth and Planetary Science Letters*, 36, 44-50, 1977.
- Zreda, M. G., F. M. Phillips, D. Elmore, P. Kubik, P. Sharma, and R. Dorn, Cosmogenic chlorine-36 production rates in terrestrial rocks. *Earth and Planetary Science Letters*, 105, 94-109, 1991.
- Zreda, M., and J. Noller, Ages of prehistoric earthquakes revealed by cosmogenic chlorine-36 in a bedrock fault scarp at Hebgen Lake. *Science*, 292, 1097-1099, 1998.

Appendix 1—³⁶Cl production mechanisms

There are seven different reactions that create ³⁶Cl in carbonate rocks. The relationships between rock chemistry, sample depth, and ³⁶Cl production rates are discussed in this appendix. Symbol definitions and units can be found in Table A1.

Spallation of ⁴⁰Ca

In the upper 3 meters of the Earth's surface, spallation of ⁴⁰Ca atoms by fast secondary neutrons is the dominant ³⁶Cl-creating reaction in calcite. These neutrons react with ⁴⁰Ca nuclei, producing ³⁶Cl. The rate at which this spallation occurs depends on the flux of secondary neutrons at the surface, which is a function of the altitude and latitude of the sample [Lal, 1991].

Although surface production rates of ³⁶Cl by ⁴⁰Ca spallation ($P_{sp}(0)$) have been calibrated by a number of researchers (Table A2), some disagreement remains. We have chosen to use the production rates of Stone et al. (1996) and Stone et al., (1998) because the calibrations were done on Ca-rich mineral separates and carbonates and thus are based on Ca reactions exclusively. We have not considered changes in production rates over time due to fluctuations in Earth's magnetic field because the associated error is less significant than the other errors inherent to our model and data.

³⁶Cl production from ⁴⁰Ca spallation decreases exponentially with depth (eq. A1). Production at depth due to ⁴⁰Ca spallation ($P_{sp}(z)$) is dependent on the surface production rate ($P_{sp}(0)$), the mass fractional concentration of target element, $[Ca]$, the shielding depth (z), (g cm^{-2}), which is the depth in cm multiplied by the rock density (2.75 g cm^{-3} , measured in 5 limestone samples), and an attenuation length ($\Lambda_{sp} = 160 \text{ g cm}^{-2}$) for cosmic-ray neutrons,

$$P^{36}Cl_{sp}(z) = P_{sp}(0)[Ca] \exp^{-z/\Lambda_{sp}} \text{ atoms } ^{36}\text{Cl yr}^{-1}. \quad (\text{A1})$$

^{36}Cl concentrations resulting from ^{40}Ca spallation at depth (z) below a steadily-eroding surface will eventually reach an equilibrium between ^{36}Cl production and loss of ^{36}Cl by radioactive decay and erosion of the upper surface (eq. A2). The erosion rate, ε (cm yr^{-1}), results in a nuclide abundance ($N^{36}Cl_{(Ca)}$) from ^{40}Ca spallation:

$$N^{36}Cl_{(Ca)} = \frac{P_{sp}(0)[Ca] \exp^{-z/\Lambda_{sp}}}{\lambda + \varepsilon\rho/\Lambda_{sp}} \text{ atoms } ^{36}\text{Cl (gm rock)}^{-1} \text{ yr}^{-1}. \quad (\text{A2})$$

Muon capture by ^{40}Ca

Whereas ^{40}Ca spallation is the predominant ^{36}Cl production mechanism in the very shallow subsurface (< 3 meters), negative muons are less-reactive than neutrons and therefore penetrate further into rocks [Spannagel and Fireman, 1972; Charalambus, 1971]. Three meters and deeper beneath the surface, negative muon capture by ^{40}Ca is the dominant ^{36}Cl production mechanism in low-chlorine rocks such as we sampled (eq. A3). The production rate of ^{36}Cl at depth from muons ($P_{(\mu^-,Ca)}(z)$), has been parameterized by Fabryka-Martin, (1988) and Stone, et al. (1998):

$$P_{(\mu^-,Ca)}(z) = \Psi_{\mu^-}(z)[Ca]Y_{Ca} \text{ atoms } ^{36}\text{Cl (gm rock)}^{-1} \text{ yr}^{-1}, \quad (\text{A3})$$

where Ψ_{μ^-} is the negative muon stopping rate (stopped $\mu^- \text{ g}^{-1} \text{ yr}^{-1}$) at depth (z), $[Ca]$ is the mass fraction of Ca in the rock, and Y_{Ca} is the number of atoms ^{36}Cl produced per stopped μ^- in each respective sample [Stone et al., 1998]. Y_{Ca} was scaled for each sample using the muon capture probabilities of each of the major elements in carbonate rocks (Ca, Mg, O, and C) and the calibrated Y_{Ca} value of $0.012 \text{ atoms } ^{36}\text{Cl (gm rock)}^{-1} \text{ yr}^{-1}$ for pure calcite [von Egidy and Hartmann, 1982; Knight et al., 1980; Stone et al., 1998].

The stopping rate of negative muons with respect to depth is approximated by Stone et al. (1998), with a 5th order polynomial, which follows the form (eq. A4):

$$\log_{10}[\Psi_{\mu^-}(z)] = a + b \log_{10}(z) + c[\log_{10}(z)]^2 + \dots f[\log_{10}(z)]^5 \quad (\text{A4})$$

for the coefficients defined in Stone et al. (1998). This polynomial approximation becomes inaccurate for $z < 100 \text{ g cm}^{-2}$; we assign the 100 g cm^{-2} value of Ψ_{μ} to all $z < 100 \text{ g cm}^{-2}$. The surface production rate of ^{36}Cl due to negative muon capture in pure calcite is $2.1 \pm 0.4 \text{ atom } ^{36}\text{Cl g (calcite)}^{-1} \text{ yr}^{-1}$ at sea level and high latitude [Stone et al., 1998].

Thermal neutron capture by ^{35}Cl

Chlorine-36 can also be produced by the incorporation of a thermal (low energy) neutron into a ^{35}Cl nucleus. The production rate of ^{36}Cl by thermal neutron capture is dependent on the percentage of thermal neutrons absorbed by ^{35}Cl , a factor known as f_{35} , as well as the abundance of thermal neutrons moving through the rock. There are many different reactions that produce thermal neutrons, including spallation, muon capture, Bremsstrahlung reactions (γ -radiation), and radiogenic U-fission and U-Th (α) decay [Fabryka-Martin, 1988; Liu et al., 1994; Bierman et al., 1995; Stone et al., 1998]. For rocks such as ours with low chlorine ($< 10 \mu\text{g g}^{-1}$), ^{36}Cl production from thermal neutron activation is less significant than production from spallation and muon capture of ^{40}Ca .

Spallation thermal neutrons. The spallation of atoms in the atmosphere and rock by secondary fast neutrons releases additional neutrons. These neutrons eventually lose their kinetic energy through collisions with other atoms and become thermalized. Liu (1994) describes ^{36}Cl production at depth from spallation thermal neutrons ($P_{(sp,n)}(z)$) (eq. A5),

$$P_{(sp,n)}(z) = P_{n,sp}(0) f_{35} (k_1 \exp^{-z/\Lambda_{sp}} + k_2 \exp^{-z/L_{th}}). \quad (\text{A5})$$

Neutrons near the rock/atmosphere interface tend to escape the rock before they can be thermalized, therefore thermal neutron production decreases sharply in the tens of centimeters nearest the rock surface (k_1 and k_2 are pre-exponential terms that account for

the change in production rate just below the surface; L_{th} is the neutron diffusion length in limestone, g cm^{-2}) [Bierman et al., 1995; Dep et al., 1994; Liu et al., 1994]. The equilibrium concentration of ^{36}Cl due solely to spallation thermal neutrons based on nuclide production and decay ($N^{36}\text{Cl}_{(sp,n)}$), at a given erosion rate (ϵ) is quantified in eq. A6,

$$N^{36}\text{Cl}_{(z,\epsilon)} = P_{(sp,n)}(0) f_{35} \left(\frac{k_1 \exp^{-z/\Lambda_{sp}}}{\lambda + \epsilon\rho/\Lambda_{sp}} + \frac{k_2 \exp^{-z/L_{th}}}{\lambda + \epsilon\rho/L_{th}} \right). \quad (\text{A6})$$

Negative muon capture. When negative muons are captured by elements such as Cl, C, Ca, and O, the nucleus releases neutrons that are then thermalized [Fabryka-Martin, 1988; Bierman et al., 1995; Stone et al., 1998]. The production of thermal neutrons at depth by muon capture ($P_{(\mu-,Ca)}(z)$) is dependent on the rate at which muons are stopped in the rock ($\Psi_{\mu-}(z)$), the neutron yield per stopped muon (Y_s), and the percent of thermal neutrons captured by ^{35}Cl , (f_{35}) (eq.A7),

$$P_{(\mu-,Ca)}(z) = \Psi_{\mu-}(z) Y_s f_{35} \text{ atoms } ^{36}\text{Cl} (\text{gm rock})^{-1} \text{ yr}^{-1}. \quad (\text{A7})$$

Because samples collected for this study contained only trace amounts of ^{35}Cl , the contribution to ^{36}Cl production by muon capture-produced thermal neutrons are $\leq 5\%$ at the surface and 20% at 2000 g cm^{-2} .

Bremsstrahlung radiation. The slowing of high energy muons in rock produces bremsstrahlung gamma-photon radiation. This radiation can cause nuclear disintegrations, releasing thermal neutrons [Fabryka-Martin, 1988; Stone et al., 1998]. The production of ^{36}Cl beneath the surface via this reaction ($P_{(\mu-, \gamma)}(z)$) is dependent on the flux of high energy muons traveling through the rock at the given depth ($\Phi(z)$), the amount of gamma radiation produced by the flux, the number of neutrons produced by that flux (Y_f) (currently assumed to be 1 neutron per disintegration), and the fraction of neutrons captured by ^{35}Cl (f_{35}) (eq. A8, from Stone et al., 1998),

$$P_{(\mu-, \gamma)}(z) = 5.8 \times 10^{-6} Y_f \ln(0.104z) \Phi_{\mu^{\pm}}(z) f_{35} \text{ atoms } ^{36}\text{Cl} (\text{gm rock})^{-1} \text{ yr}^{-1} \quad (\text{A8})$$

where Φ is approximated by Stone et al. (1998), with another 5th order polynomial. Again, because of the low Cl levels in the Nahef East fault scarp samples (and the low production rate of thermal neutrons from bremsstrahlung radiation), fast muon-produced thermal neutrons contribute only a very small amount of ³⁶Cl to the samples. Because of the low f_{35} of the Nahef East fault scarp samples, and the relatively few ³⁶Cl atoms produced from bremsstrahlung radiation, we did not calculate a correction factor for the ³⁶Cl produced from the slowing of fast muons on tilted surfaces. Instead, we assumed that an equal number of fast muons are received from all angles in the upper hemisphere and that 28.3% of the flux travels through the footwall and 71.7% travels through the hanging wall ($51^\circ/180^\circ$ and $(180^\circ-51^\circ)/180^\circ$, respectively).

Radiogenic neutrons. U-Th alpha decay, with its sub-sequent (α,n) reactions, and ²³⁸U-fission produce thermal neutrons that can be captured by ³⁵Cl. Because this neutron production is non-cosmogenic and is dependent solely on the chemical composition of the rock, the resulting ³⁶Cl concentrations are independent of sample depth and erosion rate (eqs. A9 and A10).

For (α,n) reactions, neutron production ($PN_{(\alpha,n)}$) depends on the concentration of U and Th, and various light elements in the rock [Fabryka-Martin, 1988],

$$PN_{(\alpha,n)} = X[U] + Y[Th] \text{ n yr}^{-1}, \quad (\text{A9})$$

where (X) and (Y) are neutron-yield factors calculated using methods described by Fabryka-Martin (1988).

($PN_{(n,238U)}$) is the rate at which neutrons are produced by ²³⁸U-fission. This rate is determined by the atomic concentration of ²³⁸U (N_{238}), its decay constant (λ_{sf}), and the average number of neutrons released per spontaneous fission ($\bar{\nu}$) [Fabryka-Martin, 1988]:

$$PN_{(n,^{238}\text{U})} = N_{238} \lambda_{sf} \bar{D} \quad \text{n yr}^{-1}, \quad (\text{A10})$$

where the number of ^{36}Cl atoms produced per year from radiogenic reactions ($P_{(rad)}$) is the product of the radiogenic neutron production rate and f_{35} (eq. A11):

$$P_{(rad)} = PN_{(n,^{238}\text{U})} PN_{(n,\alpha)} f_{35} \text{ atoms } ^{36}\text{Cl (g rock)}^{-1} \text{ yr}^{-1}. \quad (\text{A11})$$

The steady-state, background concentrations of ^{36}Cl in each sample resulting from these two radiogenic sources is calculated by determining the concentration of ^{36}Cl at which radioactive decay equals production. For these low Cl, low U rocks, radiogenic nuclide contribution is less than 5% of the total ^{36}Cl content, even in the deepest samples collected for this study.

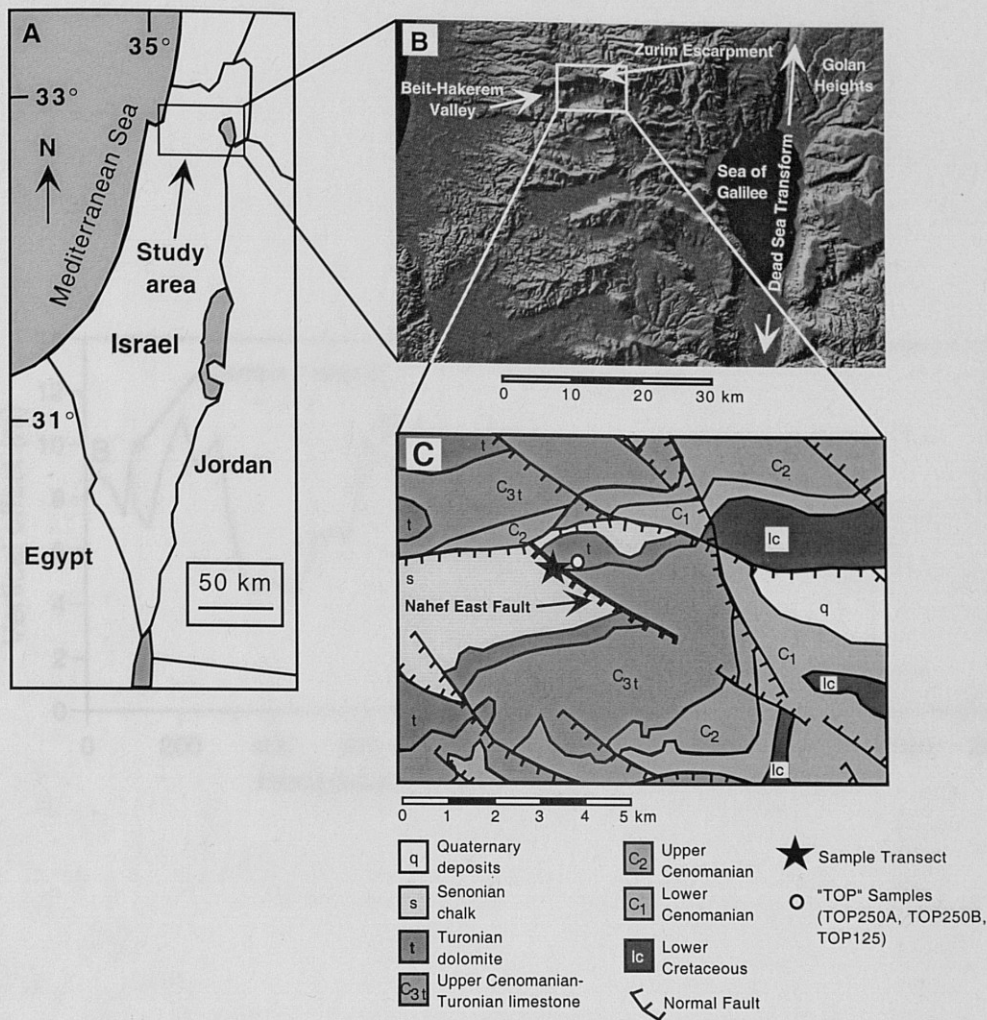


Figure 1. A) Location, B) topography and C) geology of the Nahef East fault scarp. Location of "TOP" sample shown by the open circle in C. Digital shaded relief image from J. Hall, Israel Geologic Survey Shaded Image Relief Map, 1:500,000, 1991; geologic map after Geologic Survey of Israel Geological Map, 1: 250,000, 1965.

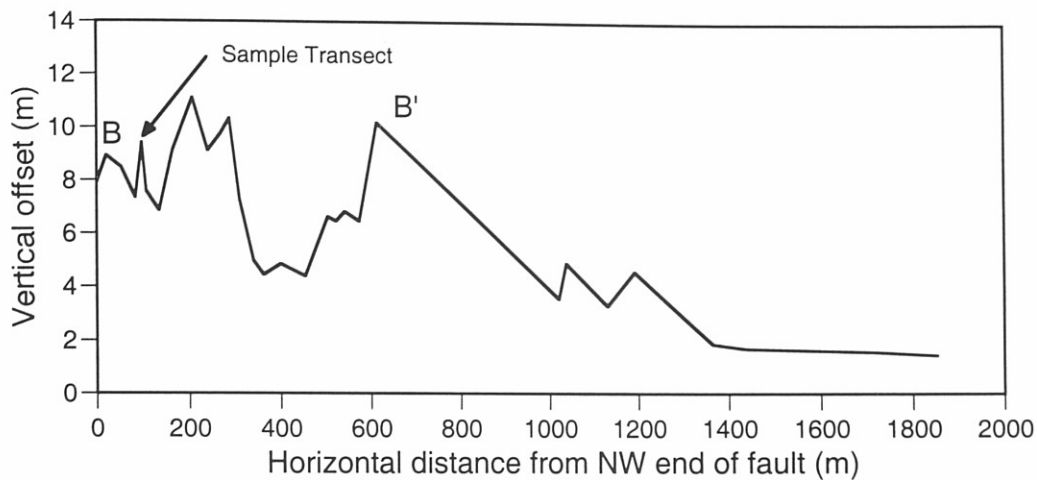


Figure 2. Characteristics of the Nahef East fault scarp. B to B' corresponds to Figure 3. *Vertical offset* is the difference in elevation between the top and bottom of the scarp. The sample transect was not taken from the scarp where the vertical offset was highest because in that location the scarp was slightly degraded. In the region from 1000 m and eastward, the fault divides into several different scarps; only the most distinct of these scarps was surveyed. Only 2 km of scarp were surveyed because the town of Nahef covers the western portion of the fault.

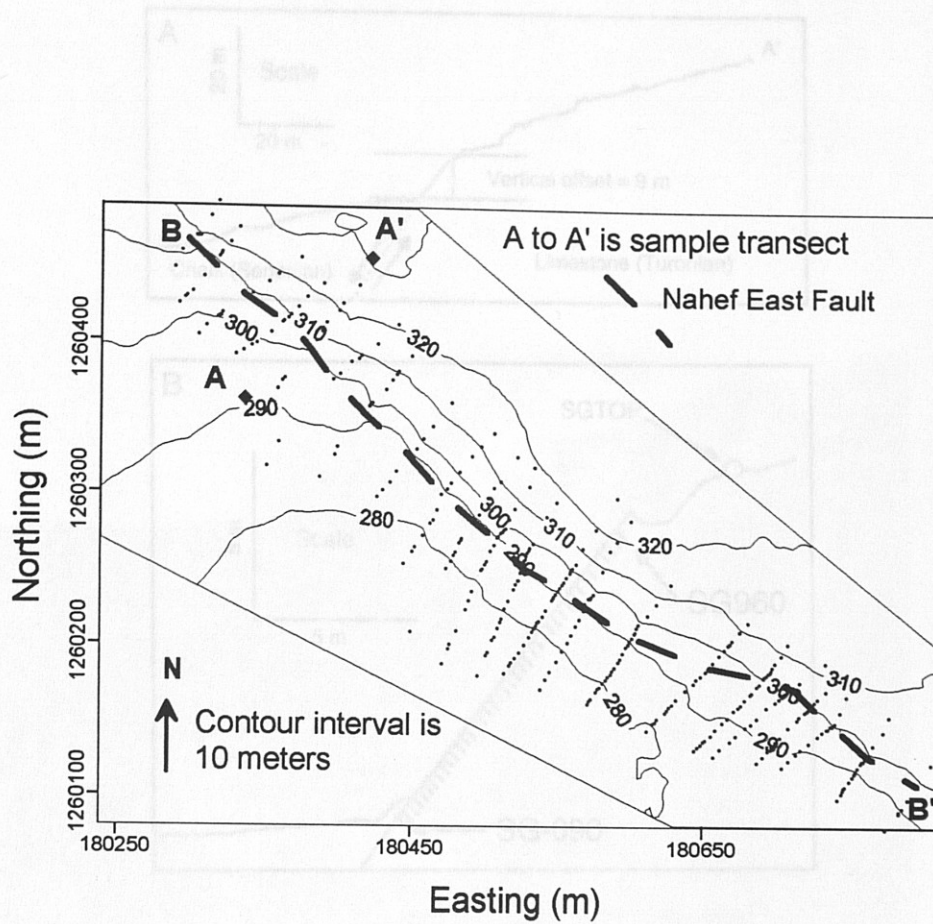


Figure 3. Topography of the Nahef East fault scarp and the surrounding area (Israel Map Grid, contours in meters asl). Constructed from GPS data points. A to A' are the ends of the scarp cross section sampled for ^{36}Cl (Figure 4), B to B' are marked on the displacement vs. distance diagram (Figure 2). Small dots are transects used to measure scarp displacement (Figure 2).

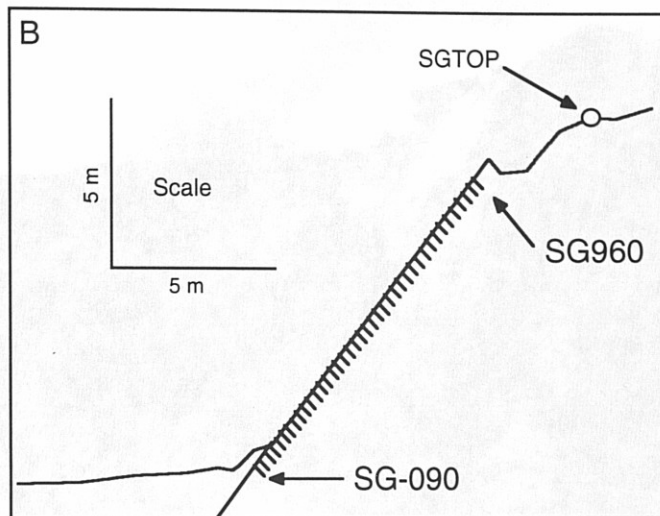
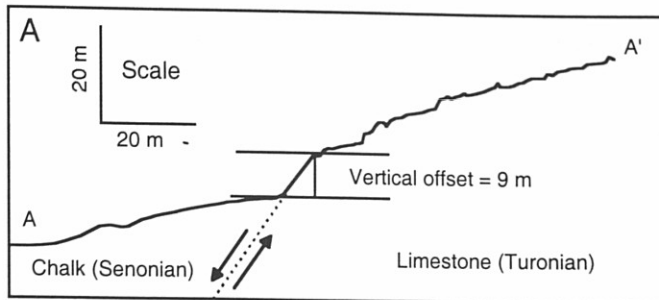


Figure 4. A. Scarp cross section at sampling location. Vertical offset is calculated by measuring the vertical distance between the top and bottom of the scarp (Figure 2). Section A to A' is shown on Figure 3. B. Close up diagram of the Nahef East fault scarp, showing a small slab of chalk covering the base of the scarp. Scarp sample locations are marked by tick-marks, and sample SGTOP is marked with an open circle.



Figure 5. Photograph of the Nahef East fault scarp, near the sample location. Photo taken looking to the northwest. The Zurim Escarpment is in the distance (upper left). Note the houses located directly above the fault scarp. Geologist in lower left is 1.6 m for scale.

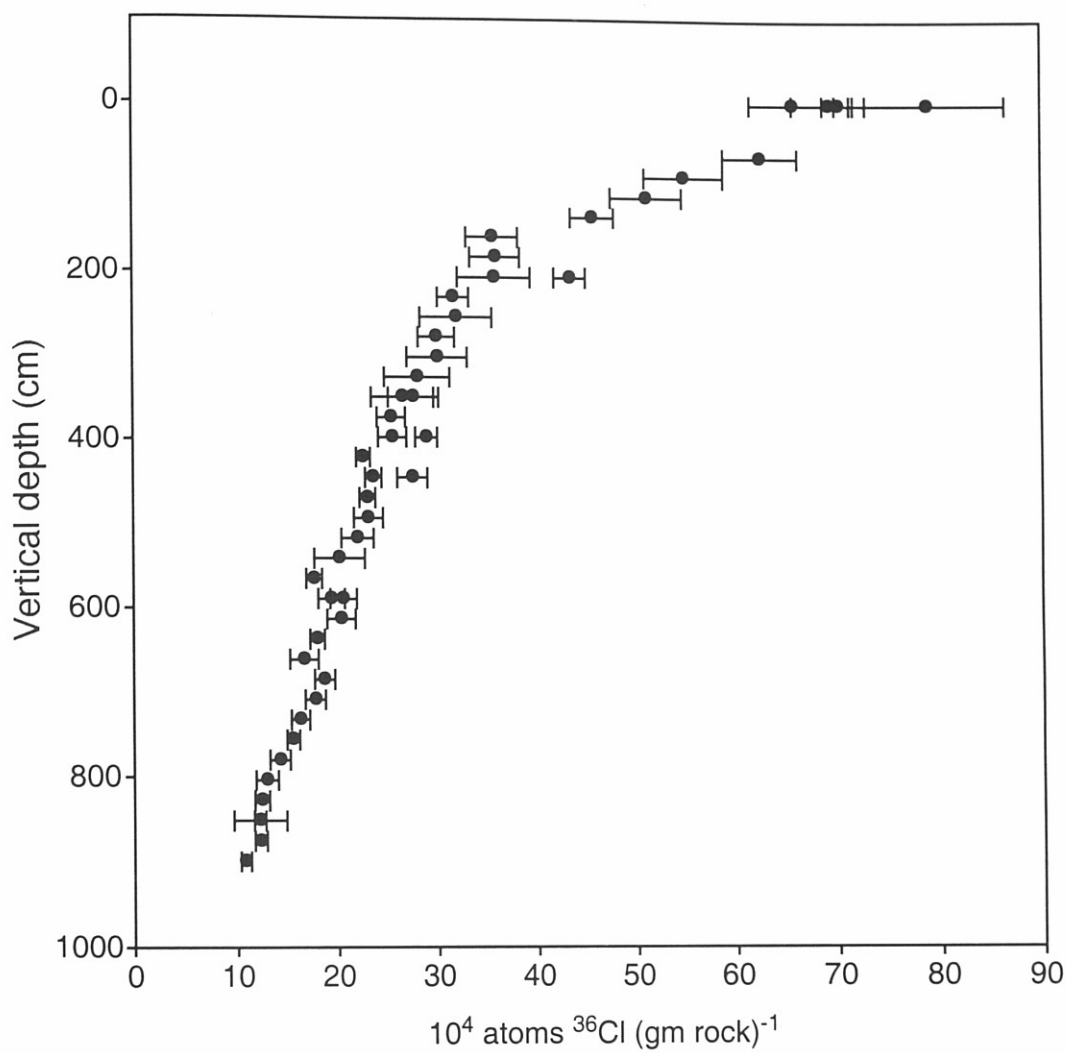


Figure 6. Measured ^{36}Cl abundance (10^4 atoms ^{36}Cl (gm rock) $^{-1}$) as a function of depth in Nahef East limestone samples. Error bars are 2σ AMS analytical error.

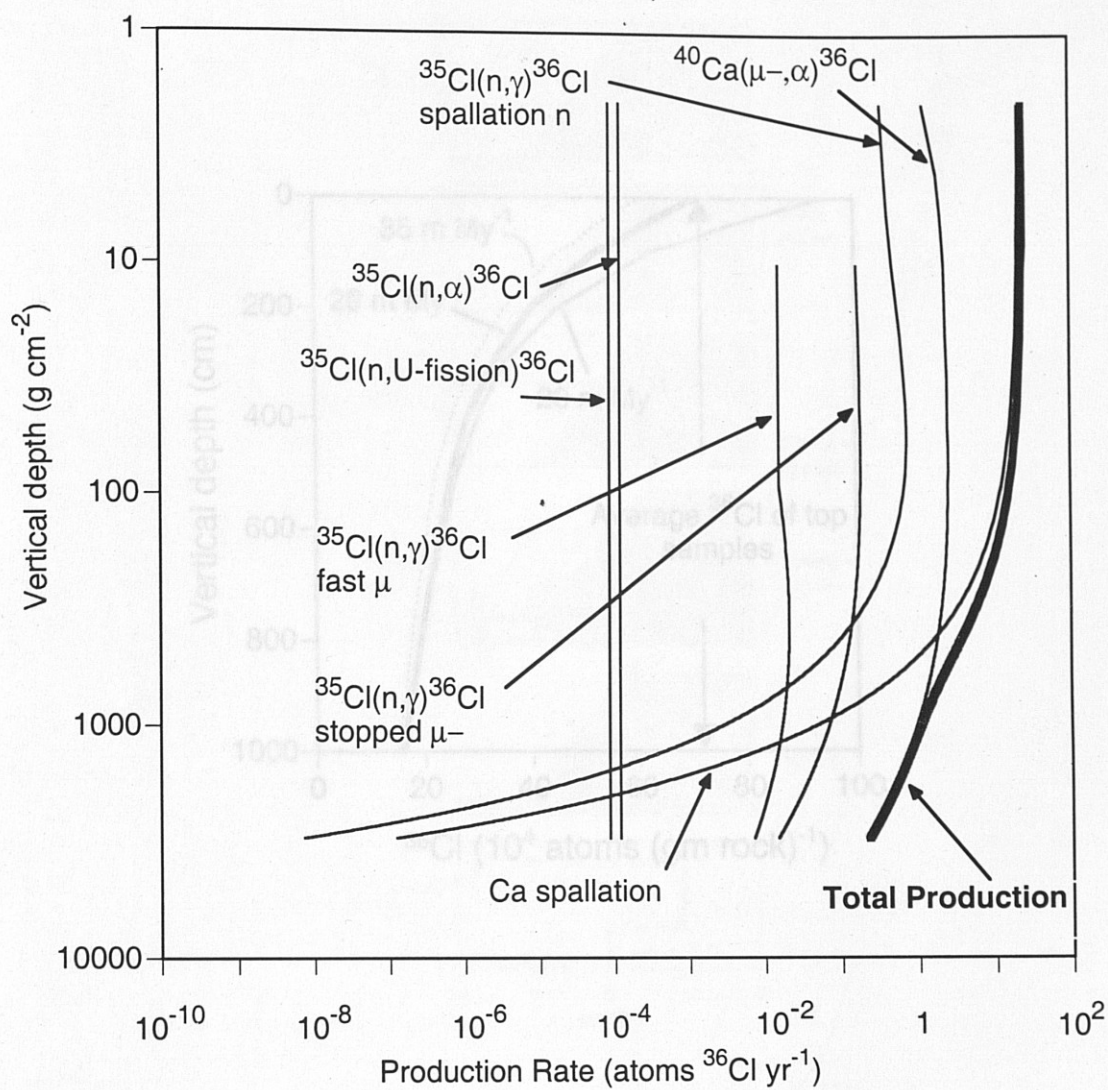


Figure 7. ^{36}Cl production rates at depth for the seven production pathways, assuming 10 ppm Cl in pure calcite (CaCO_3). ^{40}Ca spallation is the dominant production pathway in the upper 3 m, ^{40}Ca muon capture dominates below 3 m (Section 4). Actual production rates for individual samples vary according to chemical composition. Figure after Stone et al., 1998.

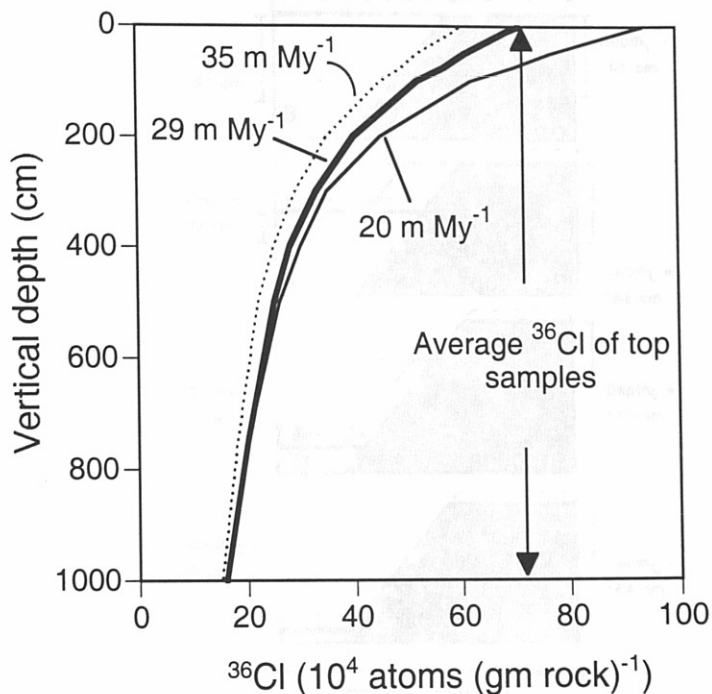


Figure 8. ^{36}Cl in the upper samples as they are exhumed at different erosion rates. An erosion rate of 29 m My^{-1} results in a ^{36}Cl concentration of 71×10^4 atoms $(\text{gm rock})^{-1}$, the measured value. Samples were taken from an elevation of 300 m, and a latitude of 33° . All seven production pathways (Figure 7) were used to calculate the erosion rate.

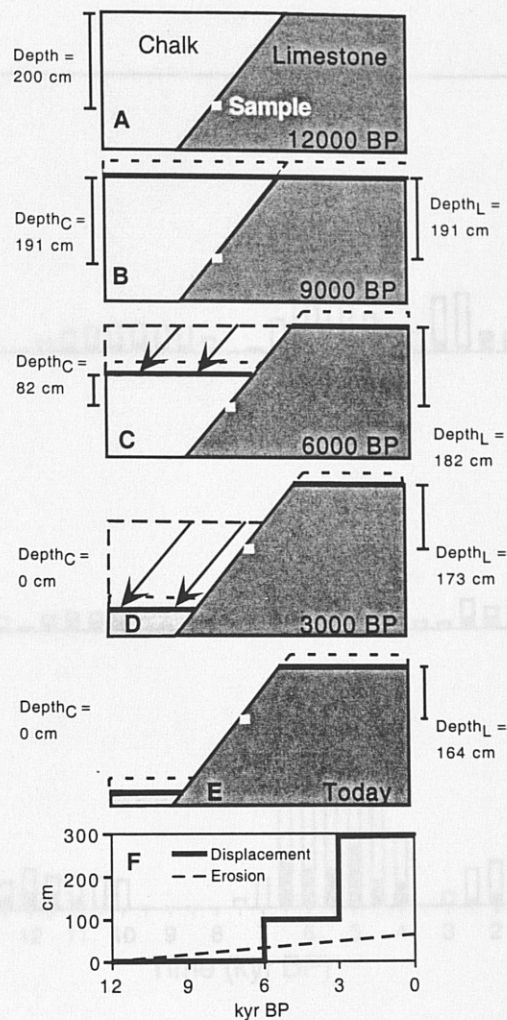


Figure 9. Sample shielding depth throughout time with respect to each fault block for a hypothetical, 12 kyr, two-event exposure history. In this situation, erosion rate is 29 m My^{-1} . A. 12 kya, sample depth is 200 cm with respect to both chalk and limestone. B. 9 kya, 9 cm of both chalk and limestone have eroded, resulting in a sample depth of 191 cm. C. 6 kya, 9 cm of erosion, faulting event 1 = 100 cm vertical displacement. Sample depth is now 182 cm for limestone, 82 cm for chalk. D. 3 kya, 9 cm erosion, faulting event 2 = 200 cm vertical displacement. Sample depth is 173 cm for limestone, 0 cm for chalk (fully exposed). E. "Today," 9 cm erosion, sample depth 164 cm for limestone, 0 cm for chalk. F. Centimeters of exhumation resulting from erosion and displacement through time. Only erosion affects sample depth for limestone; both erosion and displacement affect sample depth for chalk.

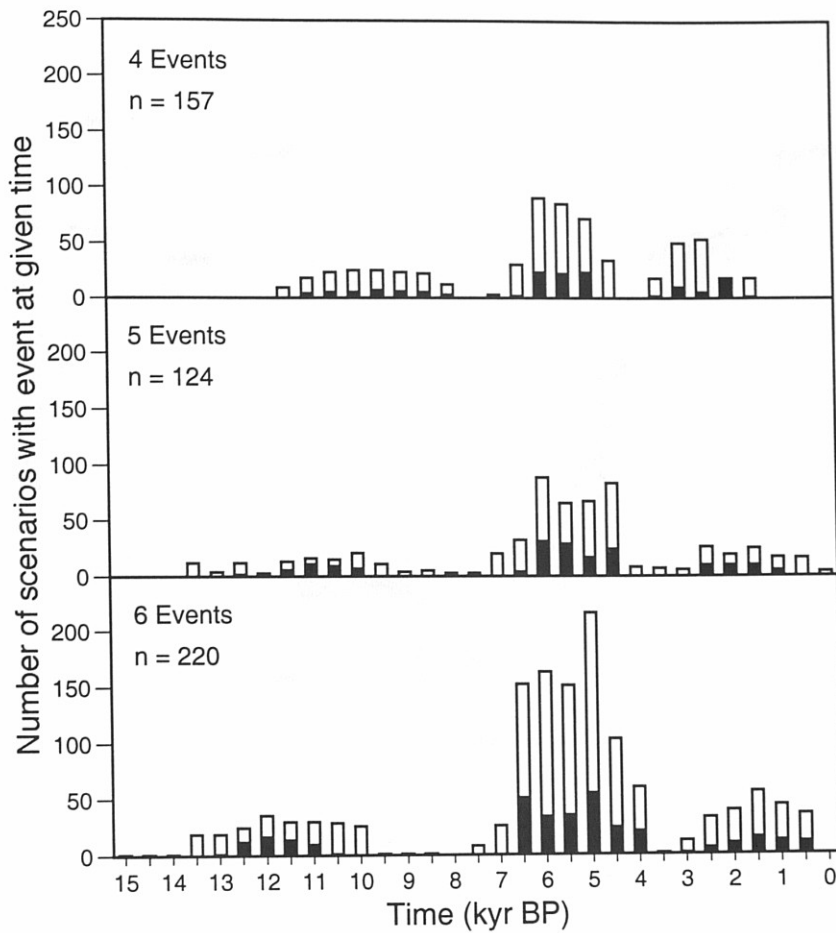


Figure 10. Distribution of displacement events occurring through time, for the four-, five- and six-event series. All displacement scenarios shown have an acceptable χ^2 value. The number of acceptable scenarios (n) for each series is included in each histogram. The height of each bar corresponds to the number of scenarios containing an event happening in each time interval. The best 25% of scenarios for each series (scenarios with the lowest χ^2) are shown in black. All three series show a large amount of displacement between 4 and 7 kya.

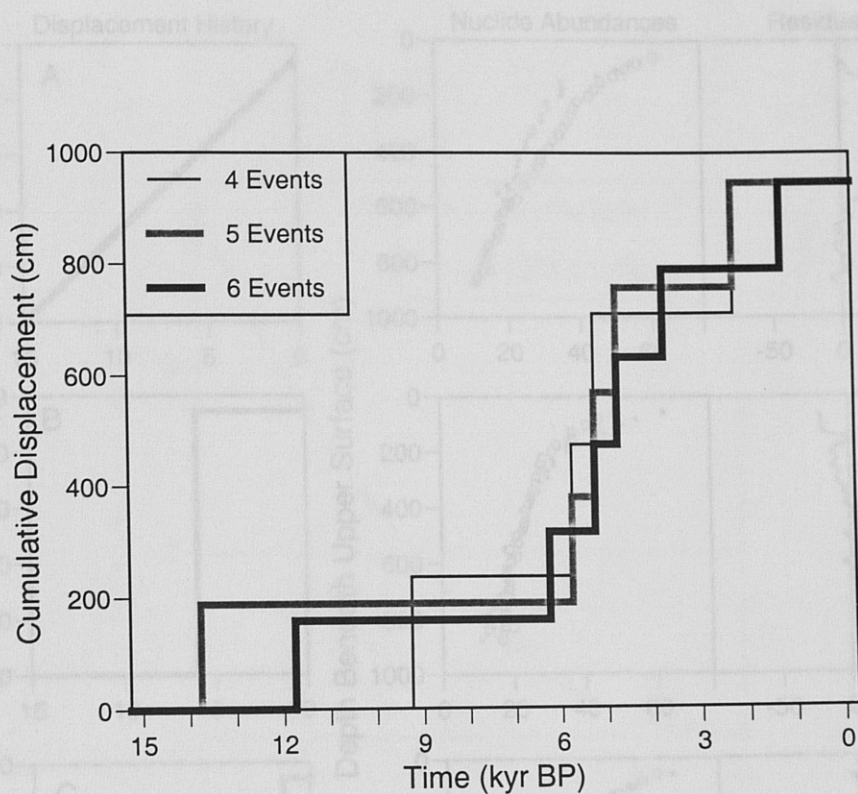


Figure 11. Cumulative displacement versus time for best fit histories of 4, 5, and 6 events. All three of these histories show most displacement occurs for a relatively short period of time, centered around 5 kyr BP. Lesser amounts of displacement occur between 14 to 11 and 1 to 2 kyr BP.

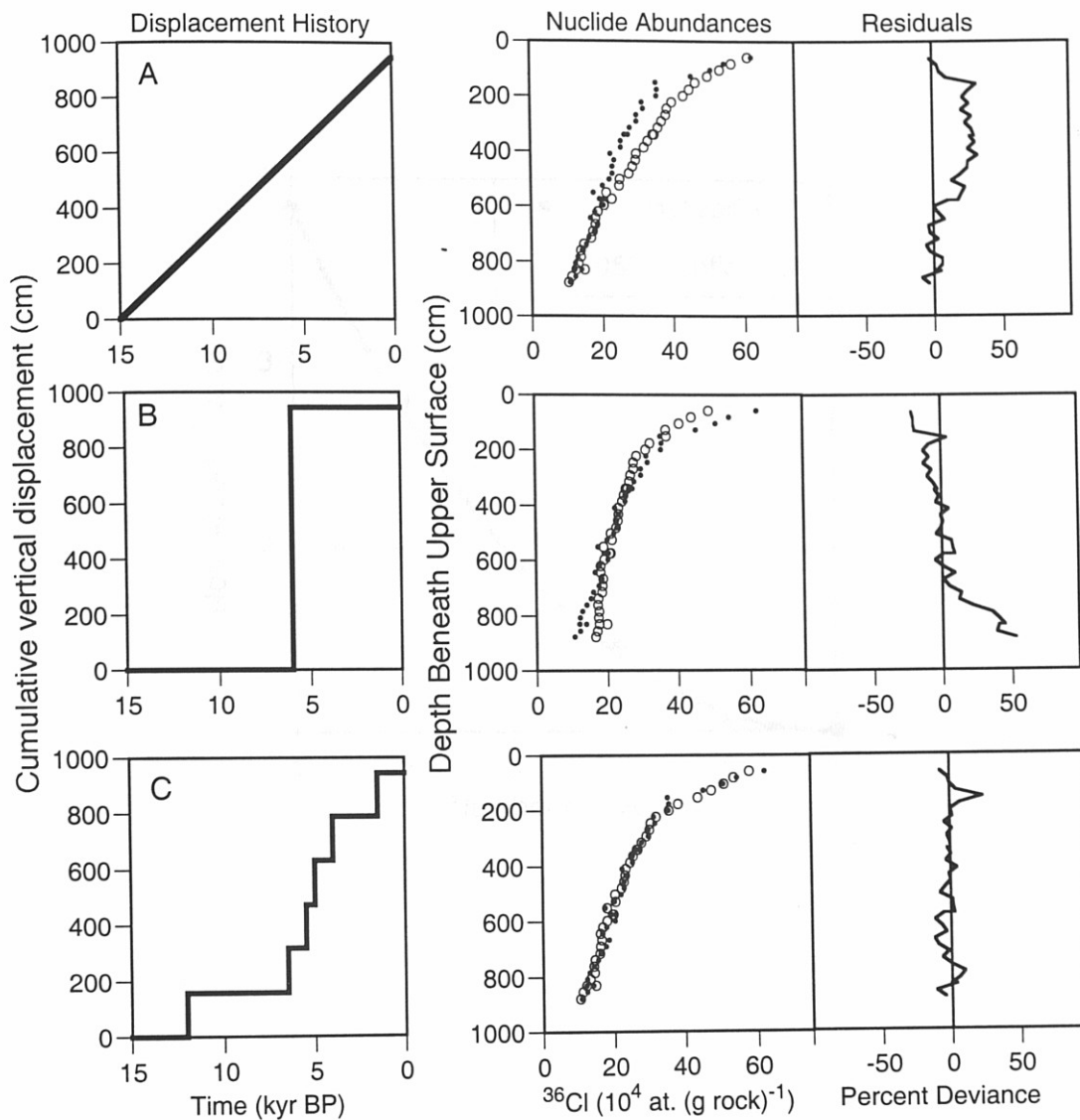


Figure 12. Three different displacement scenarios with resulting model ^{36}Cl values and residuals (percent difference between measured and model ^{36}Cl values). Model ^{36}Cl are open circles, measured ^{36}Cl data are small dots. A. Steady creep from 15 kya to the present results in model ^{36}Cl values that are too high for much of the scarp. B. A single rupture event occurring at 6.5 kya results in model ^{36}Cl values that are too low at the top of the scarp and too high at the base. C. The best fit scenario from the six-event series (with maximum displacement in the mid-Holocene) results in a reasonable fit down the entire profile.

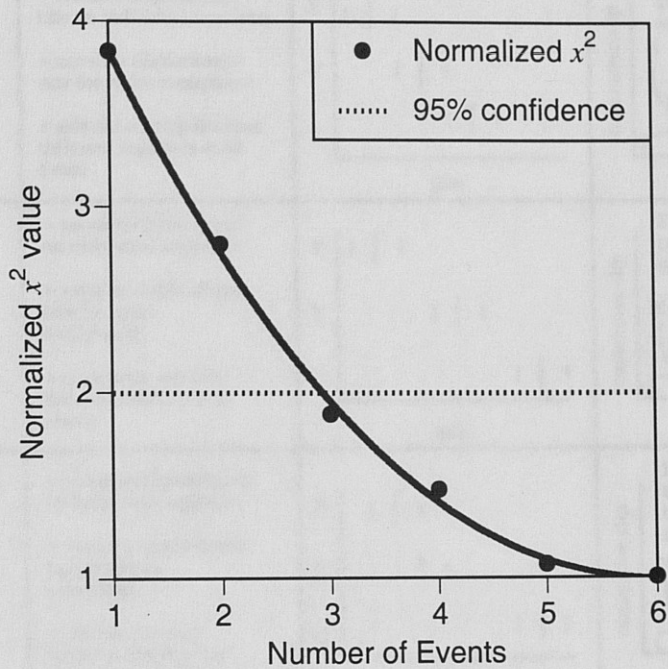


Figure 13. Lowest residual (x^2) value for each displacement history series. For comparison, x^2 values have been normalized to the lowest residual. Higher numbers of events results in better x^2 values; however, the change in x^2 decreases with an increasing number of events.

Scenario	Framework	Space-time diagram for segment behavior	displacement vs. time for individual segments
A	<ul style="list-style-type: none"> + variable displacement rate on individual segments + constant displacement rate for entire escarpment + seismic overlap between different segments at all times 		<p>Displacement occurs regularly</p>
B	<ul style="list-style-type: none"> + variable displacement on individual segments + variable displacement rate for entire escarpment + no seismic overlap between different segments 		<p>Displacement varies, no two segments active at once</p>
C	<ul style="list-style-type: none"> + variable displacement on individual segments + variable displacement rate for entire escarpment + seismic overlap between different segments at some times 		<p>Displacement varies, there may or may not be two active segments at once</p>

Figure 14. Space-time and displacement rate diagrams of different short- and long-term models of tectonic activity resulting in the behavior pattern of the Nahef East fault and the geomorphologic expression of other nearby scarps. X, Y and Z represent individual fault segments. A. Displacement rate variable on single segments, constant for entire escarpment. B. Displacement rate variable for entire escarpment, no seismic overlap between different segments. C. Displacement rate variable for entire escarpment, different segments are active at the same time.

Table 1. Chemical data for the limestone Nahef East fault scarp samples (33° latitude, 300 m above sea level; E 180373, N 1260404 Israel Map Grid coordinates).

*Sample ID	^b Depth g cm ⁻²	Sample mass (g)	Mass % Ca	Mass % Mg	^c Rock Cl µg g ⁻¹	^d Total Cl µg g ⁻¹	^e f ₃₅	^f 10 ⁴ at. ³⁶ Cl (g rock) ⁻¹	^g ³⁶ Cl/Cl ratio (10 ⁻¹³)	B µg g ⁻¹	Sm µg g ⁻¹	Gd µg g ⁻¹	Th µg g ⁻¹	U µg g ⁻¹
SGTOP-8	0	23.35	25.0	10.82	26.9	84.7	0.00839	70.2 ± 0.8	4.88 ± 0.05	2.26	0.02	0.04	0.03	5.92
TOP250A-2	0	19.06	24.7	11.07	28.3	104.3	0.00892	69.3 ± 1.8	3.91 ± 0.10	h	-	-	-	-
TOP250B-2	0	19.16	24.7	11.07	29.7	115.8	0.00937	78.9 ± 3.8	4.01 ± 0.19	-	-	-	-	-
TOP125-2	0	18.38	23.9	11.61	33.4	123.5	0.01075	65.7 ± 2.1	3.13 ± 0.10	-	-	-	-	-
SG960-5	172	25.95	39.6	0.30	3.3	51.6	0.00072	62.5 ± 1.9	7.13 ± 0.21	BDL	0.02	0.04	0.03	5.92
SG930-5	236	26.16	39.0	0.74	4.6	59.7	0.00102	54.8 ± 2.0	5.41 ± 0.20	0.15	0.04	0.09	0.09	6.86
SG900-5	301	26.29	38.4	1.22	6.9	55.1	0.00115	51.0 ± 1.8	5.44 ± 0.20	0.21	0.05	0.08	0.10	4.30
SG870-4	365	27.27	39.6	0.30	3.2	54.8	0.00069	45.5 ± 1.1	4.89 ± 0.12	BDL	0.04	0.07	0.08	4.83
SG840-5	430	25.44	27.0	9.41	33.6	85.4	0.00940	35.4 ± 1.3	2.44 ± 0.09	2.25	0.04	0.08	0.14	6.39
SG810-5	494	26.15	39.1	0.67	2.5	51.5	0.00056	35.7 ± 1.3	4.08 ± 0.14	0.11	0.02	0.04	0.04	3.64
SG780-5	559	25.97	39.1	0.67	3.3	52.5	0.00073	35.6 ± 1.2	3.99 ± 0.20	BDL	0.02	0.05	0.07	3.60
SG780D-10	559	17.03	39.1	0.65	5.7	85.5	0.00125	43.2 ± 0.8	2.97 ± 0.05	-	-	-	-	-
SG750-6	623	25.55	37.8	1.60	5.6	48.6	0.00127	31.5 ± 0.8	3.82 ± 0.01	0.16	0.03	0.06	0.08	3.96
SG720-6	688	25.35	38.0	1.42	5.9	50.5	0.00132	31.8 ± 1.8	3.70 ± 0.21	0.28	0.03	0.06	0.09	4.23
SG690-4	752	25.92	39.0	0.73	2.9	57.2	0.00065	29.8 ± 0.9	3.07 ± 0.01	BDL	0.01	0.04	0.03	3.49
SG660-6	817	29.09	39.6	0.31	3.1	44.5	0.00067	29.9 ± 1.5	3.96 ± 0.20	BDL	0.03	0.05	0.06	3.98
SG630-6	881	25.48	39.7	0.27	3.6	57.7	0.00079	27.9 ± 1.6	2.85 ± 0.17	BDL	0.04	0.07	0.10	4.82
SG600-6	946	25.80	39.6	0.31	3.3	52.3	0.00071	26.4 ± 1.5	2.97 ± 0.13	BDL	0.02	0.04	0.05	3.94
SG600R-6	946	25.75	39.6	0.33	5.7	55.2	0.00124	27.5 ± 1.2	2.94 ± 0.03	0.17	0.04	0.08	0.10	4.40
SG570-7	1010	28.79	39.6	0.30	3.1	43.5	0.00068	25.3 ± 0.7	3.43 ± 0.10	BDL	0.03	0.06	0.08	4.37
SG540-4	1075	28.38	39.7	0.29	3.8	50.6	0.00083	25.4 ± 0.7	2.96 ± 0.08	BDL	0.02	0.06	0.08	4.44
SG540D-10	1075	24.88	39.6	0.30	4.7	56.8	0.00103	28.8 ± 0.6	2.99 ± 0.06	-	-	-	-	-
SG510-7	1139	27.60	35.2	3.51	11.9	53.1	0.00283	22.4 ± 0.3	2.49 ± 0.04	0.42	0.03	0.07	0.12	4.18
SG480-7	1204	25.00	39.6	0.30	4.1	52.4	0.00090	23.5 ± 0.4	2.64 ± 0.04	BDL	0.04	0.08	0.09	4.32
SG480D-10	1204	25.25	39.6	0.31	6.3	60.4	0.00139	27.4 ± 0.7	2.67 ± 0.07	-	-	-	-	-
SG450-7	1268	25.82	39.6	0.31	5.5	51.5	0.00120	22.9 ± 0.4	2.62 ± 0.05	BDL	0.04	0.07	0.09	4.18
SG420-7	1333	27.13	39.6	0.30	5.5	53.4	0.00121	23.0 ± 0.7	2.53 ± 0.08	BDL	0.03	0.07	0.07	4.07
SG390-7	1397	27.06	37.6	1.75	6.7	57.1	0.00152	22.0 ± 0.8	2.26 ± 0.08	0.21	0.04	0.08	0.10	4.14
SG360-4	1461	25.05	39.7	0.27	2.8	55.9	0.00061	20.1 ± 1.2	2.12 ± 0.07	0.13	0.03	0.07	0.10	3.76
SG330-8	1526	26.02	30.9	6.61	15.3	70.0	0.00395	17.6 ± 0.3	1.48 ± 0.03	1.56	0.02	0.05	0.07	4.39
SG300-8	1590	22.79	30.4	6.97	26.3	83.1	0.00677	19.3 ± 0.6	1.37 ± 0.05	1.55	0.02	0.03	0.04	4.83

Table 1, continued

Sample ID	Depth g cm ⁻²	Sample mass (g)	Mass % Ca	Mass % Mg	Rock Cl µg g ⁻¹	Total Cl µg g ⁻¹	<i>f</i> ₃₅	10 ⁴ at. ³⁶ Cl (g rock) ⁻¹	³⁶ Cl/Cl ratio (10 ⁻¹³)	B µg g ⁻¹	Sm µg g ⁻¹	Gd µg g ⁻¹	Th µg g ⁻¹	U µg g ⁻¹
SG300R-8	1590	25.01	39.6	0.29	3.4	56.5	0.00075	20.5 ± 0.6	2.14 ± 0.07	0.18	0.03	0.05	0.06	3.18
SG270-8	1655	24.58	35.1	3.55	7.4	58.7	0.00177	20.3 ± 0.7	2.04 ± 0.07	0.79	0.03	0.05	0.07	3.60
SG240-8	1719	24.94	33.1	4.97	9.8	68.1	0.00242	17.9 ± 0.3	1.54 ± 0.03	1.08	0.02	0.04	0.06	3.54
SG210-4	1784	26.31	35.8	3.08	3.3	58.7	0.00079	16.6 ± 0.7	1.66 ± 0.07	0.51	0.02	0.05	0.05	1.71
SG180-9	1848	25.52	35.7	3.14	9.2	59.1	0.00215	18.6 ± 0.5	1.85 ± 0.05	0.79	0.03	0.05	0.06	3.54
SG150-9	1913	26.32	33.0	5.09	23.1	82.6	0.00588	17.7 ± 0.5	1.26 ± 0.04	1.77	0.02	0.03	0.04	3.23
SG120-9	1977	25.96	29.5	7.59	24.8	75.4	0.00652	16.2 ± 0.4	1.27 ± 0.03	2.26	0.01	0.02	0.01	3.90
SG090-9	2042	26.95	34.6	3.89	10.4	58.1	0.00247	15.5 ± 0.3	1.57 ± 0.03	1.12	0.03	0.06	0.07	4.20
SG060-9	2106	25.24	35.0	3.62	6.2	57.6	0.00147	14.2 ± 0.5	1.45 ± 0.05	0.96	0.06	0.11	0.12	4.65
SG030-4	2171	31.56	33.4	4.81	16.4	56.8	0.00393	13.0 ± 0.5	1.34 ± 0.06	2.17	0.04	0.08	0.08	4.83
SG000-9	2235	29.29	31.0	6.49	20.0	62.5	0.00503	12.4 ± 0.4	1.17 ± 0.04	1.97	0.03	0.06	0.05	6.04
SG(-030)-10	2300	31.21	33.4	4.79	18.5	68.0	0.00445	12.2 ± 0.3	1.05 ± 0.03	1.81	0.03	0.04	0.04	4.50
SG(-030B)-3	2300	23.79	30.9	6.61	35.7	107.9	0.00445	14.1 ± 1.3	0.77 ± 0.07	-	-	-	-	-
SG(-060)-10	2364	29.87	33.2	4.90	17.3	64.2	0.00421	12.3 ± 0.3	1.12 ± 0.03	1.58	0.04	0.08	0.06	3.64
SG(-090)-10	2429	36.65	31.1	6.44	20.2	59.3	0.00515	10.8 ± 0.2	1.07 ± 0.04	1.79	0.03	0.05	0.06	4.08

^a Number at end separated by a hyphen indicates batch number (e.g. SG210-4 is from Batch 4)

^b Sample depth is vertical depth beneath upper surface multiplied by limestone density ($\rho = 2.75 \text{ g cm}^{-3}$)

^c Blank corrected Cl values for rock samples

^d Total chloride from all sources (rock, carrier, and blank)

^e *f*₃₅ is the probability that a thermal neutron will be captured by a ³⁵Cl nucleus.

^f Error is 1 σ AMS analytical uncertainty, based on counting statistics

^g Ratios and uncertainties for AgCl samples including carrier

^h "TOP" samples assumed to have same trace element content as SGTOP

ⁱ Trace elements were only measured once for each replicate pair

Table A1. Symbols and Units

Table 2. Isotope and chemical data from procedural blanks.

^a Blank ID	^b ³⁶ Cl/Cl ratio x 10 ⁻¹⁵	^c Average Cl in blank (μg g solution ⁻¹)	^d Cl added as carrier μg (g solution ⁻¹)
B4a	7.6 ± 0.06	0.24	3.8
B4b	1.6 ± 0.01	0.18	4.8
B5a	8.0 ± 0.01	0.15	6.4
B5b	4.6 ± 0.01	0.23	7.5
B6a	5.3 ± 0.02	0.16	6.5
B6b	4.6 ± 0.03	0.20	8.1
B7a	3.3 ± 0.02	0.17	4.9
B7b	0.5 ± 0.02	0.12	6.6
B8a	2.1 ± 0.01	0.59	7.6
B8b	2.1 ± 0.02	0.35	7.7
B9a	3.7 ± 0.04	0.25	4.7
B9b	1.4 ± 0.02	0.15	4.8
B10a	0.2 ± 0.01	0.12	5.8
B10b	2.0 ± 0.02	0.20	5.8

^a Number in blank ID indicates batch

^b Ratio error from AMS uncertainty only

^c Some Cl was measured in blank solutions before carrier addition, though this was only a small percentage of the Cl added as carrier

^d Carrier is a weak NaCl solution, about 2 gm of carrier were added to each blank after aliquot removal but before AgCl precipitation

Table A1. Symbols and Units

Symbol Value assigned and units

General Symbols

z	depth (g cm ⁻²)
ρ	density (2.75 g cm ⁻³)
ϵ	erosion rate (cm yr ⁻¹)
λ	2.303 x 10 ⁻⁶ yr ⁻¹ (³⁶ Cl decay constant)
t_{36Cl}	3.01 x 10 ⁶ yr (³⁶ Cl half-life)
³⁶Cl from ⁴⁰Ca spallation	
$P_{(sp)}(0)$	48.8 atoms yr ⁻¹ (surface production rate of ³⁶ Cl from ⁴⁰ Ca spallation) (see table 4)
Λ_{sp}	160 g cm ⁻² attenuation of neutrons in rock [Liu et al., 1994]
³⁶Cl from ³⁵Cl thermal neutron capture	
$P_{(n,sp)}(0)$	560 fast n (g air) ⁻¹ yr ⁻¹ (stopping rate of neutrons at ground level) [Liu et al., 1994]
f_{35}	fraction of thermal neutrons captured by ³⁵ Cl
k_1	1.17 Pre-exponential term for production of neutrons in pure calcite [Liu et al., 1994]
k_2	-0.89 Pre-exponential term for production of neutrons in pure calcite [Liu et al., 1994]
L_{th}	33.0 ± 0.8 (g cm ⁻²) Characteristic length for neutron diffusion in limestone
³⁶Cl from negative muon capture on ⁴⁰Ca	
$P_{(\mu,ca)}$	production rate of ³⁶ Cl from muon capture (surface production rate = 5.0 atoms yr ⁻¹ [Stone et al., 1998])
$\Psi_{\mu^-}(z)$	stopped μ^- (g rock) ⁻¹ yr ⁻¹ intensity of stopped muons at depth z
Y_{Ca}	0.012 atom (stopped μ^-) ⁻¹ ³⁶ Cl yield from captured muons in pure calcite
Neutron production following negative μ^- capture	
$P_{(n,\mu^-)}$	atoms yr ⁻¹ (production rate of ³⁶ Cl from thermal neutrons from muon capture)
Y_s	0.44 ± neutron (stopped μ^-) ⁻¹ (average neutron yield from μ^- capture in calcite)
³⁶Cl production by fast muons ($P^{36}Cl_{n,f}$)	
$P_{(n,f)}$	atoms yr ⁻¹ (production rate of ³⁶ Cl from thermal neutrons from fast muon slowing (bremsstrahlung))
$\Phi_{\mu^\pm}(z)$	muon cm ⁻² yr ⁻¹ (fast muon flux at depth z)
Y_f	1 neutron (disintegration) ⁻¹ (average neutron yield per photodisintegration)
³⁶Cl production by (α,n) reactions and U-fission	
$P_{(rad)}$	³⁶ Cl production from (α,n) reactions and U fission (atom (g rock) ⁻¹ yr ⁻¹)
λ_{sf}	8.49 ± 0.14 x 10 ⁻¹⁷ yr ⁻¹ decay constant of U ²³⁸
ν	2.00 ± 0.03 average neutrons emitted per spontaneous fission of U ²³⁸
X	n yr ⁻¹ (neutron yield from U-produced α -radiation)
Y	n yr ⁻¹ (neutron yield from Th-produced α -radiation)

Table A2. Production rates from Ca spallation (after Stone et al., 1996)

Study	Site	Altitude	Latitude	Duration	^a Production Rate atoms (g Ca) ⁻¹ yr ⁻¹
Ca spallation only					
Yokoyama et al. (1977)	Aiguille du Midi	3840 m	47°	Modern	68 ± 14
Masarik and Reedy (1995)	high latitudes	sea level	> 60°	Modern	64.6
Stone et al. (1996)	Tabernacle Hill	1445 m	41°	17.3 ka to present	48.8 ± 1.7
Total production from Ca					
Zreda et al. (1991)	Tabernacle Hill	1445 m	39°	17.3 ka to present	54.8 ± 5.0
Swanson et al. (1994)	Puget Sound	sea level	48°	15.5 ka to present	89.5 ± 5.6
Stone et al. (1996)	Tabernacle Hill	1445 m	41°	17.3 ka to present	53.6 ± 1.8
^b Phillips et al. (1996)	various locations	s.l. to 2600	20° to 80°	60 ka – 2 ka	52.8 ± 2

^a Scaled to sea level and high latitude

^b Phillips et al. (1996) took many samples at varying elevations, latitudes, and spanning a range of exposure ages. The other studies focused on a single outcrop.

COMPREHENSIVE BIBLIOGRAPHY

- Aitken, M. J., *Thermoluminescence dating*: New York, Academic Press, 351 p., 1985.
- Anderson, R. S., J. L. Repka, and G. S. Dick, Explicit treatment of inheritance in dating depositional surfaces using in situ ^{10}Be and ^{26}Al . *Geology*, 25, 47-51, 1996.
- Atwater, B. F., Evidence for great Holocene earthquakes along the outer coast of Washington State. *Science*, 236, 942-944, 1987.
- Atwater, B. F., Geologic evidence for earthquakes during the past 2000 years along the Copalis River, southern coastal Washington. *Journal of Geophysical Research*, 97, 1901-1919, 1992.
- Bell, J. W., C. M. dePolo, A. R. Ramelli, A. M. Sarna-Wojcicki, and C. E. Meyer, Surface faulting and paleoseismic history of the 1932 Cedar Mountain Earthquake area, west-central Nevada, and implications for modern tectonics of the Walker Lane. *Geological Society of America Bulletin*, 111, 791-807, 1999.
- Ben-Menahem, A., Variation of slip and creep along the Levant Rift over the past 4500 years. *Tectonophysics*, 80, 183-197, 1981.
- Bentley, H. W., F. M. Phillips, and S. N. Davis, Chapter 10, Chloride in the terrestrial environment, in: *Handbook of Environmental Isotopes, Volume 2, Part B, The Terrestrial Environment* (P. Fritz and J-Ch. Fontes, eds.) Elsevier: New York, 1986.
- Berryman, K. R., and S. Beanland, Variation in fault behavior in different tectonic provinces of New Zealand. *Journal of Structural Geology*, 13, 177-189, 1991.
- Bierman, P. R., Using in situ cosmogenic isotopes to estimate rates of landscape evolution: a review from the geomorphic perspective. *Journal of Geophysical Research*, 99, 13885-13896, 1994.
- Bierman, P. R., A. R. Gillespie, and M. W. Caffee, Cosmogenic ages for earthquake recurrence intervals and debris flow fan deposition, Owens Valley, California. *Science*, 270, 447-450, 1995a.
- Bierman, P. R., A. Gillespie, M. Caffee, and D. Elmore, Estimating erosion rates and exposure ages with ^{36}Cl produced by neutron activation. *Geochimica et Cosmochimica Acta*, 59, 3779-3798, 1995b.
- Bierman, P. R., and E. Steig, Estimating rates of denudation and sediment transport using cosmogenic isotope abundances in sediment. *Earth Surface Processes and Landforms*, 21, 125-139, 1996.
- Bierman, P. R., K. A. Marsella, C. J. Patterson, P. T. Davis, and M. Caffee, Mid-Pleistocene cosmogenic minimum-age limits for pre-Wisconsinan glacial surfaces in southwestern Minnesota and southern Baffin Island: a multiple nuclide approach. *Geomorphology*, 27, 25-39, 1999.
- Bilokon, H., G. Cini-Castagnoli, A. Castellina, B. Piazzoli, G. Mannocci, E. Meroni, P. Picchi, and S. Vernetto, Flux of the vertical negative muons stopping at depths 0.35 -1000 hg/cm². *Journal of Geophysical Research*, 94, 12145-12152, 1989.
- Bolt, B., *Earthquakes*. New York: W. H. Freeman, 331 p., 1993.

- Bonilla, M. G., R. K. Mark, and J. J. Lienkaemper, Statistical relations among earthquake magnitude, surface rupture length, and surface fault displacement. *Bulletin of the Seismological Society of America*, 74, 2379-2411, 1984.
- Briner, J. P., and T. W. Swanson, Using inherited cosmogenic ^{36}Cl to constrain glacial erosion rates of the Cordilleran ice sheet. *Geology*, 26, 3-6, 1998.
- Bucknam, R. C., and R. E. Anderson, Estimation of fault scarp ages from a scarp-height-slope-angle relationship. *Geology*, 7, 11-14, 1979.
- Cerling, T., and H. Craig, Geomorphology and in-situ cosmogenic isotopes. *Annual Reviews of Earth and Planetary Science*, 22, 273-317, 1994.
- Charalambus, S., Nuclear transmutation by negative stopped muons and the activity induced by cosmic-ray muons. *Nuclear Physics*, A166, 145-161, 1971.
- Clark, D., P. R. Bierman, and P. Larsen, Improving in situ cosmogenic chronometers. *Quaternary Research*, 44, 366-376, 1995.
- Crone, A. J., and M. N. Machette, Surface faulting accompanying the Borah Peak earthquake, central Idaho. *Bulletin of the Seismological Society of America*, 77, 737-770, 1987.
- Crone, A. J., and K. M. Haller, Segmentation and the coseismic behavior of Basin and Range normal faults: examples from east-central Idaho and southwestern Montana, USA. *Journal of Structural Geology*, 13, 151-164, 1991.
- Crookes, J. N., and B. C. Rastin, The absolute intensity of muons at 31.6 hg cm^{-2} below sea level. *Nuclear Physics*, B58, 93-109, 1973.
- Davis, R., and O. A. Schaeffer, Chlorine-36 in nature. *Annals of the NY Academy of Science*, 62, 105-122, 1955.
- Dep, L., D. Elmore, M. Lipshutz, S. Vogt, F. Phillips, and M. Zreda, Depth-dependence of cosmogenic neutron-capture produced ^{36}Cl in a terrestrial rock. *Nuclear Instruments and Methods in Physics Research*, B92, 301-307, 1994a.
- Dep, L., D. Elmore, J. Fabryka-Martin, J. Masarik, and R. Reedy, Production rate systematics of in-situ-produced cosmogenic nuclides in terrestrial rocks: monte carlo approach of investigating $^{35}\text{Cl}(n,\gamma)^{36}\text{Cl}$. *Nuclear Instruments and Methods in Physics Research*, B92, 321-325, 1994b.
- dePolo, C. M., D. G. Clark, D. B. Slemmons, and A. R. Ramelli, Historic surface faulting in the Basin and Range province, western North America: implications for fault segmentation. *Journal of Structural Geology*, 13, 123-136, 1991.
- Dockhorn, B., S. Neumaier, F. J. Hartmann, C. Petitjean, H. Faestermann, G. Korschinek, H. Morinaga, and E. Nolte, Determination of erosion rates with cosmic ray produced ^{36}Cl . *Hadrons and Nuclei*, 341, 117-119, 1991.
- Dunne, J., D. Elmore, and P. Muzikar, Scaling factors for the rates of production of cosmogenic nuclides for geometric shielding and attenuation at depth on sloped surfaces. *Geomorphology*, 27, 3-12, 1999.
- Easterbrook, D. J., *Surface Processes and Landforms*. Macmillan Publishing Company: New York, 520 p., 1993.
- Ellenblum, R., M. Shmuel, A. Amotz, R. Thomas, and A. Boas, Crusader castle torn apart by earthquake at dawn, 20 May 1202. *Geology*, 26, 303-306, 1998.

- Elmore, D., Ultrasensitive radioisotope, stable-isotope, and trace element analysis in the biological sciences using tandem accelerator mass spectrometry. *Biological Trace Element Research*, 12, 231-245, 1987.
- Elmore, D., and F. M. Phillips, Accelerator mass spectrometry for measurement of long-lived radioisotopes. *Science*, 236, 543-550, 1987.
- Fabryka-Martin, J. T., Production of radionuclides in the Earth and their hydrogeologic significance, with emphasis on chlorine-36 and iodine-129. Ph.D. dissertation, University of Arizona, Tucson, 400 p., 1988.
- Florence, T. M., and Y. J. Farrar, Spectrophotometric determination of chloride at the parts-per-billion level by mercury (II) thiocyanate method. *Analytical Chimica Acta*, 54, 373-377, 1971.
- Forman, S. L., A. R. Nelson, J. McCalpin, Thermoluminescence dating of fault scarp derived colluvium: Deciphering the timing of paleoearthquakes on the Wasatch fault zone, north-central Utah. *Journal of Geophysical Research*, 96, 595-605, 1991.
- Freund, R., On the stratigraphy and tectonics of the Upper Cretaceous in the western Galilee, *Bulletin of the Research Council of Israel*, G8, 43-50, 1959.
- Freund, R., A model of the structural development of Israel and adjacent areas since Upper Cretaceous times. *Geology Magazine*, 102, 189-205, 1965a.
- Freund, R., Upper Cretaceous reefs in northern Israel. *Israel Journal of Earth Sciences*, 14, 108-121, 1965b.
- Freund, R., The geometry of faulting in the Galilee. *Israel Journal of Earth Sciences*, 19, 117-140, 1970.
- Friedlander, M. W., *Cosmic Rays*. Harvard University Press: Cambridge, 160 p., 1989.
- Frydman, S., and M. Talesnick, Analysis of seismically triggered slides off Israel. *Environmental Geology and Water Science*, 11, 21-26, 1988.
- Garfunkel, Z., I. Zak, and R. Freund, Active faulting in the Dead Sea Rift. *Tectonophysics*, 80, 1-26, 1980.
- Gillespie, A. R., and P. R. Bierman, Precision of terrestrial exposure ages and erosion rates estimated from analysis of cosmogenic isotopes produced in situ. *Journal of Geophysical Research*, 100, 24637-24649, 1995.
- Granger, D. E., J. W. Kirchner, and R. Finkel, Spatially-averaged long-term erosion rates measured from in-situ produced cosmogenic nuclides in alluvial sediment. *Journal of Geology*, 104, 249-257, 1996.
- Granger, D. E., J. W. Kirchner, and R. C. Finkel, Quaternary downcutting rate of the New River, Virginia, measured from differential decay of cosmogenic ^{26}Al and ^{10}Be in cave-deposited alluvium. *Geology*, 25, 107-110, 1997.
- Grant, L. B., and K. Sieh, Paleoseismic evidence of clustered earthquakes on the San Andreas fault in the Carrizo Plain, California. *Journal of Geophysical Research*, 99, 6819-6841, 1994.
- Hallet, B., and J. Putkonen, Surface dating of dynamic landforms; young boulders on aging moraines. *Science*, 265, 937-940, 1994.

- Handwerger, D. A., T. E. Cerling, and R. L. Bruhn, Cosmogenic ^{14}C in carbonate rocks. *Geomorphology*, 27, 13-24, 1999.
- Hanks, T. C., R. C. Bucknam, K. R. Lajoie, and R. E. Wallace, Modification of wave cut and faulting controlled landforms. *Journal of Geophysical Research*, 89, 5771-5790, 1984.
- Hanks, T. C., and D. P. Schwartz, Morphologic dating of the pre-1983 fault scarp on the Lost River fault at Doublespring Pass Road, Custer County, Idaho. *Bulletin of the Seismological Society of America*, 77, 837-846, 1987.
- Hecker, S., and D. P. Schwartz, The characteristic earthquake revisited: Geological evidence of the size and location of successive earthquakes on large faults. *U.S. Geological Survey Open File Report*, 94-568, 79-80, 1994.
- Jackson, J. A., and N. J. White, Normal faulting in the upper continental crust. *Journal of Structural Geology*, 11, 15-36, 1989.
- Kafri, U., Neogene to Quaternary drainage systems and their relationship to young tectonics: lower Galilee, Israel. *Geological Survey of Israel Report*, GSI/1/97, 1997.
- Knight, J. D., C. J. Orth, M. E. Schillaci, R. A. Naumann, F. J. Hartmann, J. J. Reidy, and H. Schnewly, Coulomb capture ratios of negative muons in $\text{N}_2 + \text{O}_2$, NO and CO. *Physics Letters*, 79A, 377-379, 1980.
- Koning, D. J., and F. J. Pazzaglia, Paleoseismicity, fault segmentation and persistence of mountain-front landforms in a continental rift setting, Alamogordo fault, southern New Mexico. *Geological Society of America, Abstracts with Programs*, 30, 329, 1998.
- Kurz, M. D., D. Colander, T. W. Trull, R. B. Moore, and K. O'Brien, Cosmic ray exposure dating with in situ produced cosmogenic ^3He : results from young Hawaiian lava flows. *Earth and Planetary Science Letters*, 97, 177-189, 1990.
- Lal, D., and B. Peters, Cosmic-ray produced radioactivity on the earth. In *Handbuch der Physik* (ed. S. Flugg). 46, 551-612, 1967.
- Lal, D., In situ-produced cosmogenic isotopes in terrestrial rocks. *Annual Reviews of Earth and Planetary Science*, 16, 355-388, 1988.
- Lal, D., Cosmic ray labeling of erosion surfaces: In situ production rates and erosion models. *Earth and Planetary Science Letters*, 104, 424-439, 1991.
- Leavy, B. D., F. M. Phillips, D. Elmore, P. W. Kubik, and E. Gladney, Measurement of cosmogenic $^{36}\text{Cl}/\text{Cl}$ in young volcanic rocks: an application of accelerator mass spectrometry in geochronology. *Nuclear Instruments and Methods in Physics Research*, B29, 246-250, 1987.
- Lide, D. R., ed., *CRC Handbook of Chemistry and Physics*, 75th edition. CRC Press: Boca Raton, 1994.
- Liu, B., F. M. Phillips, J. T. Fabryka-Martin, M. M. Fowler, and W. D. Stone, Cosmogenic ^{36}Cl accumulation in unstable landforms 1. Effects of the thermal neutron distribution. *Water Resources Research*, 30, 3115-3125, 1994.
- Machette, M. N., S. F. Personius, and A. R. Nelson, Quaternary geology along the Wasatch fault zone: Segmentation, recent investigations and preliminary conclusions. In *Assessment of Regional Earthquake Hazards and Risk along the*

- Phillips, M. G., and W. W. Hayes, eds., *Wasatch Front, Utah* (P. A. Gori and W. W. Hayes, eds.), U. S. Geological Survey Open File Report, 87-585-I, pp. A1-A72, 1987.
- Machette, M. N., S. F. Personius, A. R. Nelson, D. P. Schwartz, and W. R. Lund, The Wasatch fault zone, Utah—segmentation and history of Holocene earthquakes. *Journal of Structural Geology*, 13, 137-149, 1991.
- Maserik, J., and R. C. Reedy, Terrestrial cosmogenic-nuclide production systematics calculated from numerical simulations. *Earth and Planetary Science Letters*, 136, 381-396, 1995.
- Matmon, A., E. Zilberman, and Y. Enzel, Morphometric analysis for determining the age of escarpments: an example from the Galilee, northern Israel. *Geological Survey of Israel*, Report GSI/31/98, 1998.
- Matmon, A., Y. Enzel, E. Zilberman, and A. Heimann, Late Pliocene and Pleistocene reversal of drainage systems in northern Israel: tectonic implications. *Geomorphology*, 28, 43-59, 1999.
- Mayer, L., Dating Quaternary fault scarps in alluvium using morphological parameters. *Quaternary Research*, 22, 300-313, 1984.
- McCalpin, J. P., W. Zuchiewicz, and L. C. A. Jones, Sedimentology of fault-scarp-derived colluvium from the 1983 Borah Peak rupture, central Idaho. *Journal of Sedimentary Petrology*, 63, 120-130, 1993.
- McCalpin, J. P., *Paleoseismology*. Academic Press: San Diego. 588 p., 1996.
- McGill, S. F., and K. Sieh, Surficial offsets on the central and eastern Garlock Fault associated with prehistoric earthquakes. *Journal of Geophysical Research*, 96, 21597-21621, 1991.
- Nash, D. B., Morphologic dating of degraded normal fault scarps. *Journal of Geology*, 88, 353-360, 1980.
- Nash, D. B., Influence of scarp height on the accuracy of morphologic dating. *Abstracts with Programs, Geological Society of America*, 30, 329, 1998.
- Niemi, T. M., and N. T. Hall, Late Holocene slip rate and recurrence of great earthquakes on the San Andreas fault in northern California. *Geology*, 20, 195-198, 1992.
- Nishiizumi, K., C. P. Kohl, J. R. Arnold, J. Klein, D. Fink, and R. Middleton, Cosmic ray produced ^{10}Be and ^{26}Al in Antarctic rocks: exposure and erosion history. *Earth and Planetary Science Letters*, 104, 440-454, 1991.
- Noller, J., M. G. Zreda, and W. R. Lettis, Use of cosmogenic Cl-36 to date late Quaternary activity of the Hebgen Lake Fault, Montana. *Geological Society of America, Abstracts with Programs*, 28, 300, 1996.
- Phillips, F. M., B. D. Leavy, N. D. Jannik, D. Elmore, and P. W. Kubik, The accumulation of cosmogenic chlorine-36 in rocks: a method for surface exposure dating. *Science*, 231, 41-43, 1986.
- Phillips, F. M., M. G. Zreda, S. S. Smith, D. Elmore, P. W. Kubik, and P. Sharma, Cosmogenic chlorine-36 chronology for glacial deposits at Bloody Canyon, eastern Sierra Nevada. *Science*, 248, 1529-1532, 1990.
- Phillips, F. M., M. G. Zreda, M. R. Flinsch, D. Elmore, and P. Sharma, A reevaluation of cosmogenic ^{36}Cl production rates in terrestrial rocks. *Geophysical Research Letters*, 23, 949-951, 1996.

- Phillips, F. M., J. P. Ayarbe, B. Harrison, P. Sharma and D. Elmore, Calibration of fault-scarp diffusion models using cosmogenic nuclides. *Geological Society of America Abstracts with Programs*, 30, 298, 1998
- Reches, Z. and D. F. Hoexter, Holocene seismic and tectonic activity in the Dead Sea Rift. *Tectonophysics*, 80, 235-254, 1981.
- Ron, H., R. Freund, Z. Garfunkel, and Z. Nur, Block rotation by strike-slip faulting: structural and paleomagnetic evidence (Israel). *Journal of Geophysical Research*, 89, 6256-6270, 1984.
- Schwartz, D. P., and K. J. Coppersmith, Fault behavior and characteristic earthquakes: examples from the Wasatch and San Andreas fault zones. *Journal of Geophysical Research*, 89, 5681-5698, 1984.
- Schwartz, D. P., Paleoseismicity, persistence of segments, and temporal clustering of earthquakes; examples from the San Andreas, Wasatch, and Lost River fault zones. In: *Proceedings of Conference XLV; a workshop on fault segmentation and controls of rupture initiation and termination*, USGS Open File Report, 361-375, 1989.
- Shimazaki, K., and T. Nakata, Time-predictable recurrence model for large earthquakes. *Geophysical Research Letters*, 7, 279-282, 1980.
- Sieh, K., M. Stuiver, and D. Brillinger, A more precise chronology of earthquakes produced by the San Andreas Fault in southern California. *Journal of Geophysical Research*, 94, 603-623, 1989.
- Spannagel, G. and E. L. Fireman, Stopping rate of negative cosmic ray muons near sea level. *Journal of Geophysical Research*, 77, 5351-5359, 1972.
- Stewart, I. S., and P. L. Hancock, Neotectonic normal fault zones in the Aegean region. *Journal of Structural Geology*, 13, 191-204, 1991.
- Stewart, I. S., A rough guide to limestone fault scarps. *Journal of Structural Geology*, 18, 1259-1264, 1996.
- Stone, J. O., G. L. Allan, L. K. Fifield, and R. G. Cresswell, Cosmogenic chlorine-36 from calcium spallation. *Geochimica et Cosmochimica Acta*, 60, 679-692, 1996a.
- Stone, J. O., K. Lambeck, L.K. Fifield, J. M. Evans, and R. G. Cresswell, Late Glacial age for the Main Rock Platform, western Scotland. *Geology*, 24, 673-676, 1996b.
- Stone, J. O., J. M. Evans, L. K. Fifield, G. L. Allan, and R. G. Cresswell, Cosmogenic chlorine-36 production in calcite by muons. *Geochimica et Cosmochimica Acta*, 62, 433-454, 1998.
- Stuiver, M., S. W. Robinson, and I. C. Yang, ^{14}C dating to 60,000 years BP with proportional counters, in *Radiocarbon Dating, Proceedings of the Ninth International Conference, Los Angeles and La Jolla, 1976*, edited by R. Berger and H. E. Suess, pp. 202-215, University of California Press, Berkeley, 1979.
- Survey of Israel, *Atlas of Israel: Cartography, Physical and Human Geography*. Macmillian Publishing Company: New York, 1985.
- Swanson, T. W., R. C. Finkel, L. Harris, and J. Southon, Application of ^{36}Cl dating based on the deglaciation history of the Cordilleran ice sheet in Washington and British Columbia. *Geological Society of America, Abstracts with Programs*, 26, 512 p., 1994.

- van Eck, T. and A. Hofstetter, Fault geometry and spatial clustering of micro earthquakes along the Dead Sea-Jordan rift fault zone. *Tectonophysics*, 180, 15-27, 1990.
- von Egidy, T., and F. J. Hartmann, Average muonic coulomb capture probabilities for sixty-five elements. *Physics Review A*, 26, 2355-2360, 1982.
- Wallace, R. E., Earthquake recurrence intervals on the San Andreas fault. *Geological Society of America Bulletin*, 81, 2875-2890, 1970.
- Wallace, R. E., Profiles and ages of young fault scarps, north-central Nevada. *Geological Society of America Bulletin*, 88, 1267-1281, 1977.
- Wallace, R. E., Patterns and timing of late Quaternary faulting in the Great Basin province and relation to some regional tectonic features. *Journal of Geophysical Research*, 89, 5763-5769, 1987.
- Wells, D. L., and K. J. Coppersmith, Empirical relationships among magnitude, rupture length, rupture area, and surface displacement. *Bulletin of the Seismological Society of America*, 82, 974-1002, 1994.
- Wheeler, R. L., Persistent segment boundaries on basin-range normal faults. In *Fault Segmentation and Controls of Rupture Initiation and Termination* (D. P. Schwartz and R. H. Sibson, eds.), U. S. Geological Survey Open File Report, 89-315, pp. 432-444, 1989.
- Wilson, R. C., and D. K. Keefer, Dynamic analysis of a slope failure from the 6 August 1979, Coyote Lake, California earthquake. *Bulletin of the Seismological Society of America*, 73, 863-877, 1983.
- Wu, D., and R. L. Bruhn, Geometry and kinematics of active normal faults, South Oquirrh Mountains, Utah: implications for fault growth. *Journal of Structural Geology*, 16, 1061-1075, 1994.
- Yamaguchi, D. K., B. F. Atwater, D. E. Bunker, B. E. Benson, and M. S. Reid, Tree-ring dating the 1700 Cascadia earthquake. *Nature*, 389, 922-923, 1997.
- Yokoyama, Y., J. L. Reys, and F. Guichard, Production of radionuclides by cosmic rays at mountain altitudes. *Earth and Planetary Science Letters*, 36, 44-50, 1977.
- Youngs, R. R., and K. J. Coppersmith, Implications of fault slip rates and earthquake recurrence models to probabilistic seismic hazard estimates. *Bulletin of the Seismological Society of America*, 75, 939-964, 1985.
- Zhang, B., L. Yuhua, G. Shunmin, R. E. Wallace, R. C. Bucknam, and T. C. Hanks, Fault scarps related to the 1793 earthquake and seismicity of the Yinchuan graben, Ningxia Huizu Ziziqu, China. *Bulletin of the Seismological Society of America*, 76, 1253-1288, 1986.
- Zreda, M. G., F. M. Phillips, D. Elmore, P. Kubik, P. Sharma, and R. Dorn, Cosmogenic chlorine-36 production rates in terrestrial rocks. *Earth and Planetary Science Letters*, 105, 94-109, 1991.
- Zreda, M., and J. Noller, Ages of prehistoric earthquakes revealed by cosmogenic chlorine-36 in a bedrock fault scarp at Hebgen Lake. *Science*, 292, 1097-1099, 1998.
- Zreda, M. G., J. England, F. M. Phillips, D. Elmore, and P. Sharma, Unblocking of the Nares Strait by Greenland and Ellesmere ice-sheet retreat 10,000 years ago. *Nature*, 398, 139-142, 1999.

APPENDIX A—Sample Processing

(Modified from Stone et al., 1996a)

(1) *Sample preparation*

Trim cores of weathered surfaces (remove top 0.5 cm)
Measure length, weight of core
Break into 1 cm pieces
Grind in jaw crusher and plate grinder
Sieve, save 125-250 and 250-500 micron fractions
Rinse 250-500 micron fraction in DI water until all fines are washed away
Dry in oven overnight

(2) *Leaching (to remove meteoric ^{36}Cl)*

Tare and label clean 600 mL beaker
Add 20-25 g dry sample
Wet with about 100 mL DI water. In separate beaker, mix about 15 mL 2N HNO_3 and 50-100 mL DI (this is enough acid to dissolve about 1.5 g CaCO_3). Pour into rock sample beaker slowly (to avoid foaming). Try to get even dissolution of grain boundaries.
Once reaction has died down, cover and let sit for 12-24 hrs. Swirl occasionally.
Rinse 3-4 times with DI and repeat leaching procedure
Rinse thoroughly with DI (at least 5 times) to remove ALL $\text{Ca}(\text{NO}_3)_2$
Dry overnight. Sample should decrease in weight by about 3 g.

(3) *Sample loading*

Tare and label a clean 600 mL pyrex beaker
Add ~20 g of sample to beaker, weigh. Use more sample if Cl content is really low (to ensure sufficient Ag^{36}Cl yield at the end of the process).

(4) *Dissolution*

In fume hood, wet sample to a slurry with DI and gradually add 10 mL 2N HNO_3 per gram of sample. Avoid foaming (add only 10 mL at a time). It will take about 400 mL acid to dissolve 20 g sample.
Once dissolution is complete, swirl to homogenize and then allow insoluble fraction to settle overnight.
Weigh beaker, trying to avoid stirring up sediment.

(5) *Splitting for chloride analysis and carrier spiking*

Tare and label a clean 50 mL centrifuge tube.
Tare and label two 15 mL centrifuge tubes to receive Cl spectrophotometry aliquots
Tare and label 15 mL centrifuge tube for ICP fraction.
Transfer about 13 mL of solution to the 50 mL tube, weigh.
Divide this fraction between small centrifuge tubes for Cl analyses: 4 mL in one, 8 mL in the other. Weigh those tubes and calculate how much is left in 50 mL vial.
Dilute remainder to 40 mL, weigh.
Transfer 1 mL to ICP tube, weigh ICP tube.
Dilute ICP fraction to 10 mL.
Discard remainder of clear solution from 50 mL centrifuge tube.

Weigh carrier bottle

Pipette 2-3 mL carrier into sample beaker (make sure no carrier sticks in pipette).

Re-weigh carrier bottle, calculate amount removed. About 1 mg of Cl should be added to the dissolved rock sample.

(6) *Separation from dissolution residue*

Let sediment settle (if there is time, let it sit overnight again).

Decant as much supernatant as possible into a clean, labeled 600 mL beaker. Cover with watchglass.

Swirl sample, centrifuge remaining material in the 50 mL tube used earlier. Rinse beaker with DI to assure getting all sediment into centrifuge tube.

Rinse and re-suspend sediment, centrifuge again and transfer to beaker.

Rinse several more times, discarding supernatant.

Dry in oven overnight, and re-weigh to determine weight of insoluble fraction.

(7) *AgCl and Ag₂SO₄ precipitation*

Place the 600 mL beaker containing clear solution on hotplate (set at ~300-350 °F).

Let sit until actively convecting (2 hrs)

In dim room, add 1 mL 10% AgNO₃ solution, it should become cloudy and flecks of AgCl should appear.

Let sit on hotplate for an hour to flocculate. Do not disturb.

Tap to collect flecks in a pile on the base of the beaker. Let cool (and settle) in a dark cupboard overnight.

Decant and discard as much clear solution as possible.

Label a clean 50 mL centrifuge tube, centrifuge remaining solution (discarding supernatant). Be sure to rinse out beaker to assure maximum yield.

AgCl will stick in the point of the tube. Add 5 mL DI, re-suspend, re-centrifuge, discard supernatant.

(8) *Sulfate clean-up*

Dissolve precipitate in 2 mL 1:1 NH₃-H₂O solution. Dissolution will take about 5 minutes.

Transfer to 10 mL glass test tube (rinse the first vessel once in DI, pour rinse water into test tube as well).

Add 1 mL saturated BaNO₃ solution to the glass test tube, precipitate should form in the solution. Top off tube with DI, cover with parafilm, and let sit for at least 24 hours (the more the better-- up to a week is fine).

Tap precipitate into base of test tube, centrifuge for 5 minutes.

Using clean pipette, transfer clear solution to 15 mL centrifuge tube. Leave last 2 mL of solution in test tube to avoid transferring the BaSO₄ precipitate to the clean AgCl solution.

(9) *Final AgCl precipitation*

Place 15 mL centrifuge tube with dissolved AgCl into clean water bath, place on hotplate set at ~300-350 °F.

In separate beaker, put ~10 mL 2N HNO₃ per sample. Add about 1 mL AgNO₃ solution per sample to assure overabundance of silver. Cover with watchglass and place on hot plate.

Allow materials to heat to near boiling (~1hr.).

When hot, add about 10 mL acid/silver mixture to centrifuge tube. Tube will 'steam' and become cloudy.

When done steaming, re-cap and allow to sit and flocculate for ~1 hr.

Transfer to dark cabinet to cool and settle overnight.

Tap AgCl into base of tube, centrifuge and decant supernatant.

Rinse once, re-suspend, centrifuge and decant supernatant.

Dry in a DARK oven overnight (dry on side so bead of water does not sit on plug of AgCl—this will decrease drying time by about 10x).

Place samples in small, clean containers, wrap in tin foil, and keep stored out of the light.

APPENDIX B—Dissolution data

This appendix contains the raw data from AgCl precipitation and ICP and Cl analysis aliquot removal. Table B-1 contains the masses of the various components of the AgCl procedure, including the beaker, sample, and acid. In Table B-1 are the masses of the aliquots used to make Cl and ICP samples, and the mass of carrier added to each sample. Table B-2 shows ICP aliquot measurements; for each sample there is a set of aliquot values (mass of “original” solution) and a dilution value (total mass of aliquot after dilution).

Table B-1. Dissolution and carrier data

Sample ID	Beaker (gm)	Sample (gm)	Diss. sample (gm)	beaker and acid (gm)	Aliquot 1 for ICP and Cl(gm)	carrier added (gm)
top250A	170.5	19.1	19.064	390.5	15.354	2.41
top 250B	167.8	19.2	19.157	394.7	15.235	2.75
top 125	167.7	19.1	18.376	365.3	14.753	2.77
BlankA	166.9	0	0	361.6	14.255	3.15
BlankB	166.87	0	0	368	14.222	2.45
-030B	167.7	25.7	23.794	427.8	16.789	2.86
TestA	171.7	19.6	19.427	374.9	14.217	3.03
TestB	170.6	19.5	19.331	372.8	14.229	3.56
SGB1a	171.6	0	0	328.3	15.833	0.97
SGB2a	166.8	0	0	348.9	13.968	1.81
SGB3a	163.6	0	0	357.4	14.144	3.36
SGb1b	173.9	0	0	380.6	14.769	1.01
SGB2b	235.1	0	0	413.8	13.179	1.97
SGB3b	167	0	0	322.3	14.741	3.38
SGTC	172	30.1	29.833	567.1	13.828	1.56
SGTD	170.7	32.4	32.110	603	15.52	2.26
SGB4a	163.4	0	0	448.7	16.937	1.84
SG870	166.7	27.4	27.265	659.4	15.911	2.22
SG690	167.7	26.0	25.918	569.3	15.3	2.25
SG540	166.8	28.5	28.382	584.1	17.932	2.11
SG360	163.6	25.2	25.046	541.8	15.526	2.13
SG210	169.7	26.4	26.307	586.5	14.838	2.33
SG030	171.7	34.8	31.563	590.5	16.116	2.02
SGB4b	172.1	0	0	413.8	14.794	1.98

Table B-1, continued

Sample ID	Beaker (gm)	Sample (gm)	Diss. sample (gm)	beaker and acid (gm)	Aliquot 1 for ICP and Cl(gm)	carrier added (gm)
SG960	166.8	26.0	25.948	578.8	15.984	2.00
SG930	171.3	26.3	26.156	577.5	15.515	2.32
SG900	169.7	26.4	26.291	589.4	15	2.02
SG840	163.4	25.6	25.435	595.5	15.631	2.10
SG810	172	26.2	26.147	571.8	14.688	2.05
SG780	167.6	26.1	25.972	553	15.077	2.05
SGB5b	173.9	0	0	329.3	15.098	1.98
SGB6a	171.5	0	0	367.4	14.89	2.16
SG750	171.2	25.7	25.547	560.2	15.967	1.76
SG720	166.7	25.5	25.351	551.5	16.158	1.82
SG660	172.0	29.2	29.094	569.7	15.207	1.94
SG630	167.5	25.6	25.482	581.1	16.794	2.23
SG600	163.3	25.9	25.803	573.8	14.967	2.04
SG600R	166.8	25.9	25.75	562	16.102	2.06
SGB6b	169.6	0	0	333	14.534	2.26
SGB7a	163.6	0	0	412.4	11.409	2.08
SG570	166.7	29.0	28.790	616.8	14.286	1.85
SG510	167.6	27.8	27.601	610.7	15.527	1.81
SG480	171.3	25.1	24.995	612.5	13.798	1.93
SG450	172.0	26.0	25.820	611.1	13.924	1.90
SG420	170.6	27.3	27.125	592.2	15.052	2.09
SG390	166.9	27.2	27.058	625.1	14.869	2.19
SGB7b	173.9	0	0	417.4	14.533	2.73
SGB8a	172.0	0	0	344.1	14.053	2.22
SGTOP	167.5	23.4	23.353	503.9	15.069	2.03
SG330	166.9	26.3	26.017	535.8	13.870	2.13
SG300R	172.0	25.2	25.010	538.8	15.436	1.97
SG300	170.6	23.0	22.790	528.0	15.371	1.92
SG270	167.0	24.8	24.576	535.5	14.502	1.85
SG240	166.7	25.1	24.944	542.2	15.035	2.18
SGB8b	170.4	0	0	333.5	13.908	2.14
SGB9a	170.5	0	0	440.4	14.185	2.17
SG180	167.6	25.6	25.516	515.1	15.234	2.04
SG150	172.0	26.4	26.317	538.2	14.690	2.53
SG120	167.5	26.0	25.962	513.4	15.149	2.11
SG090	166.9	27.1	26.947	536.2	14.808	2.05
SG060	166.6	25.5	25.235	512.6	16.411	2.08
SG000	171.6	29.4	29.286	564.1	15.271	1.97
SGB9b	167.0	0	0	413.3	14.221	2.03

Table B-1, continued

Sample ID	Beaker (gm)	Sample (gm)	Diss. sample (gm)	beaker and acid (gm)	Aliquot 1 for ICP and Cl(gm)	carrier added (gm)
SGB10a	167.2	0	0	399.3	13.226	2.30
SG-030	166.6	31.3	31.206	610.4	14.982	2.53
SG-060	167.6	30.0	29.869	627.5	14.837	2.28
SG-090	166.9	36.9	36.647	685.8	13.659	2.32
SG480D	167.6	25.4	25.247	499.5	14.462	2.25
SG780D	172.0	17.1	17.025	505.7	14.329	2.24
SG540D	171.6	25.0	24.884	514.1	16.583	2.13
SGB10b	163.3	0	0	392.2	14.360	2.29

Samples for ICP analysis were diluted so solutions would be in the working concentration range for the equipment. Table B-2 contains dilution data for these solutions. "Aliquot" indicates the mass of material removed from the primary solution, "Dilution" indicates the final mass after DI water was added. "ICP aliquot 1" was removed from the primary dissolved limestone solution. Subsequent aliquots were removed from solutions diluted from the original sample.

Table B-2 ICP and Cl spectrophotometric aliquot data. All data are in grams.

Sample ID	Spec. 1 aliq. (gm)	spec. 2 aliq. (gm)	ICP aliquot 1 (gm)	ICP dilution 1 (gm)	ICP aliquot 2 (gm)	ICP dilution 2 (gm)	ICP aliquot 3 (gm)	ICP dilution 3 (gm)	ICP aliquot 4 (gm)	ICP dilution 4 (gm)
top250A	5.221	8.880	1.253	39.253	1.817	9.844				
top 250B	4.909	8.705	1.621	39.357	1.700	9.950				
top 125	4.640	8.815	1.298	40.164	1.411	9.750				
BlankA	5.093	8.409	0.753	39.493	1.757	9.939				
BlankB	4.278	8.423	1.521	40.307	1.362	9.945				
-030B	4.822	9.422	2.545	39.182	1.576	9.857	0.985	10.005		
TestA	4.422	8.352	1.443	39.944	1.947	10.273				
TestB	4.577	8.579	1.073	39.395	1.553	9.858				
SGB1a	4.154	8.755	2.924	39.236						
SGB2a	4.360	8.264	1.344	39.406						
SGB3a	4.567	7.852	1.725	38.833						
SGB1b	4.35	8.451	1.968	39.177						
SGB2b	4.398	6.982	1.799	40.008						
SGB3b	4.556	8.255	1.930	40.177						
SGTC	4.641	7.89	1.297	38.525	2.074	9.682				
SGTD	8.533	5.025	1.962	39.588	1.589	9.844				

Table B-2, continued

Sample ID	Spec. 1	spec. 2	ICP	ICP	ICP	ICP	ICP	ICP	ICP	ICP
	aliq.	aliq.	aliquot	dilution	aliquot	dilution	aliquot	dilution	aliquot	dilution
			1	1	2	2	3	3	4	4
SGB4a	3.838	9.219	3.880	40.284	2.200	9.803				
SG870	4.349	8.370	3.192	40.127	1.977	10.012	1.494	4.903	1.439	4.713
SG690	8.247	5.590	1.463	39.746	2.332	9.819	0.986	9.899		
SG540	4.349	10.22	3.363	40.439	1.785	9.818	0.985	9.765		
SG360	4.932	8.442	2.152	40.443	2.304	9.814	0.985	9.866		
SG210	4.050	8.303	2.485	38.718	1.735	9.879	0.987	9.991		
SG030	4.804	8.669	2.643	40.062	2.333	9.753	0.985	9.965		
SGB4b	4.754	8.725	1.315	38.541	1.732	9.861				
SGB5a	4.922	8.076	1.305	38.953	1.509	9.833				
SG960	4.669	8.427	2.888	40.153	1.295	9.640	0.983	9.787		
SG930	4.872	8.831	1.809	39.609	1.652	9.980	0.974	9.761		
SG900	4.777	8.498	1.729	38.794	1.914	9.781	0.988	9.727		
SG840	4.395	9.594	1.338	39.463	1.793	9.807	1.964	9.808		
SG810	4.362	8.779	1.546	38.974	1.578	9.797	1.963	9.882		
SG780	4.500	8.585	1.989	39.496	1.435	9.643	0.984	9.817		
SGB5b	4.516	8.334	2.251	39.95	1.509	9.808				
SGB6a	4.577	8.393	1.917	39.232	1.513	9.83				
SG750	4.369	8.737	2.854	40.233	1.341	9.932	0.984	10.007		
SG720	4.975	8.847	2.335	39.773	1.649	9.809	0.989	9.824		
SG660	4.906	8.849	1.453	39.609	1.654	9.999	1.961	9.926		
SG630	4.747	9.403	2.641	39.895	1.712	9.868	1.268	4.915	1.331	4.831
SG600	4.720	8.876	1.374	39.327	1.722	9.832	1.965	9.922		
SG600R	4.654	8.822	2.628	39.649	1.568	10.00	0.978	9.869		
SGB6b	4.806	8.111	1.619	39.248	1.392	9.904				
SGB7a	3.914	6.199	1.296	40.024	1.643	9.84				
SG570	3.964	8.511	1.811	40.113	1.679	10.00	1.929	9.876		
SG510	4.995	9.182	1.350	40.678	1.504	9.983	1.988	9.896		
SG480	4.323	8.027	1.448	39.622	1.320	9.902	1.970	9.863		
SG450	4.958	7.628	1.338	40.490	1.696	9.891	1.967	9.889		
SG420	5.069	8.654	1.329	39.042	1.475	9.954	1.966	10.002		
SG390	4.597	8.765	1.507	39.689	1.591	9.774	0.984	9.899		
SGB7b	4.230	8.864	1.439	39.609	1.550	9.819				
SGB8a	4.335	8.392	1.326	39.706	1.559	9.907				
SGTOP	4.404	8.754	1.911	39.599	1.425	10.209	1.962	9.987		
SG330	5.006	7.464	1.400	39.486	1.388	9.785	1.969	9.89		
SG300R	4.781	9.054	1.601	39.595	1.327	9.778	1.967	9.946		
SG300	4.797	8.973	1.601	39.998	1.114	9.811	1.961	9.858		
SG270	4.335	8.842	1.325	39.778	1.555	9.681	1.974	9.910		
SG240	4.667	9.038	1.330	39.317	1.337	10.156	1.972	9.845		
SGB8b	4.321	7.74	1.847	39.431	1.582	10.092				

Table B-2, continued

Sample ID	Spec. 1 aliq.	spec. 2 aliq.	ICP		ICP		ICP		ICP	
			aliquot 1	dilution 1	aliquot 2	dilution 2	aliquot 3	dilution 3	aliquot 4	dilution 4
SGB9a	3.973	8.333	1.879	39.205	1.38	10.086				
SG180	4.243	9.229	1.762	40.603	1.581	9.742	1.956	9.78		
SG150	4.710	8.431	1.549	39.836	1.409	9.816	1.898	9.914		
SG120	4.732	8.727	1.690	39.063	1.573	10.128	1.956	9.843		
SG090	4.231	8.626	1.951	40.115	1.45	9.631	1.958	9.894		
SG060	4.389	10.271	1.751	39.378	1.358	9.748	1.962	10.013		
SG000	4.215	9.335	1.721	40.081	1.711	9.774	1.965	9.731		
SGB9b	4.447	8.363	1.411	39.410	1.516	10.235				
SGB10a	4.301	7.595	1.330	39.872	1.348	9.689				
SG-030	4.253	8.674	2.055	41.283	1.685	9.775	1.629	4.979	1.645	4.901
SG-060	4.831	7.921	2.085	41.871	1.501	10.25	1.973	9.815		
SG-090	5.013	7.034	1.612	41.081	1.591	9.955	1.984	9.949		
SG480D	4.551	8.301	1.610	40.607	1.509	9.639	1.971	9.920		
SG780D	4.598	8.395	1.336	40.434	1.333	9.648	1.953	9.865		
SG540D	4.823	10.02	1.739	40.302	1.625	9.993	1.977	10.056		
SGB10b	4.500	7.963	1.897	39.314	1.583	9.772				

APPENDIX C—Chloride carrier information

Table D-1. Nahc East fault scarp major element data from ICP, including grams of each of the major elements (non-normalized), % yield from calculated rock mass (using stoichiometric relationships between Ca, Mg, C and O in carbonates, $(Ca,Mg)(CO_3)_2$).

Because the amount of chloride in the limestone was so small, chloride was added to the dissolved rock after aliquot removal and before AgCl precipitation. An NaCl solution was made using pure NaCl and nanopure water. Two batches of carrier were made (Table C-1), Carrier 1 was used in AgCl batches 1 to 8, Carrier 2 was used in batches 9 and 10.

Table C-1. Components of carrier solution

Carrier ID	NaCl (g)	Water (g)	Cl concentration (g Cl (g water) ⁻¹)
Carrier 1	0.125	129.43	5.859×10^{-4}
Carrier 2	0.123	127.90	5.834×10^{-4}

APPENDIX D—ICP major element data

Table D-1. Nahef East fault scarp major element data from ICP, including grams of each of the major elements (non-normalized), % yield from calculated rock mass (using stoichiometric relationships between Ca, Mg, C and O in carbonates, $(Ca,Mg(CO_3)_2)$).

Sample ID	g Ca	g Mg	g O	g C	g rock from ICP	g rock measured	% yield	mass % Ca	mass % Mg
top250A	4.57	2.05	9.52	2.38	18.52	19.06	97.15	24.67	11.07
top 250B	4.57	2.05	9.52	2.38	18.52	19.06	97.15	24.67	11.07
top 125	3.95	1.92	8.52	2.13	16.52	18.38	89.92	23.92	11.61
BlankB	-0.02	-0.01	-0.04	-0.01	-0.07	0.00			
-030B	7.73	1.66	12.53	3.14	25.05	23.79	105.30	30.86	6.61
TestA	7.35	0.04	8.87	2.22	18.47	19.43	95.08	39.77	0.20
TestB	6.63	0.03	8.00	2.00	16.65	19.23	86.59	39.79	0.18
SGTC	12.05	0.06	14.54	3.64	30.28	29.83	101.51	39.78	0.19
SGTD	12.79	0.06	15.42	3.86	32.13	32.11	100.05	39.80	0.17
SGB4a	-0.01	0.00	-0.01	0.00	-0.02	0.00			
SG870	11.03	0.08	13.38	3.35	27.85	27.27	102.13	39.63	0.30
SG690	10.45	0.19	12.89	3.23	26.76	25.92	103.25	39.06	0.70
SG540	11.61	0.08	14.07	3.52	29.28	28.38	103.18	39.65	0.29
SG360	10.18	0.07	12.33	3.08	25.66	25.05	102.44	39.67	0.27
SG210	9.83	0.82	13.39	3.35	27.39	26.31	104.11	35.88	3.00
SG030	10.76	1.55	15.94	3.99	32.24	31.56	102.13	33.37	4.81
SGB4b	0.00	0.00	-0.01	0.00	-0.02	0.00			
SGB5a	0.01	0.00	0.00	0.00	0.01	0.00			
SG960	10.37	0.08	12.58	3.15	26.18	25.95	100.89	39.63	0.30
SG930	10.16	0.19	12.55	3.14	26.04	26.16	99.54	39.02	0.74
SG900	10.38	0.33	13.08	3.27	27.06	26.29	102.94	38.35	1.22
SG840	8.39	2.99	15.94	3.99	31.31	25.44	123.09	26.79	9.54
SG810	10.21	0.18	12.58	3.15	26.11	26.15	99.87	39.11	0.67
SG780	10.08	0.17	12.41	3.11	25.77	25.97	99.23	39.11	0.67
SGB5b	0.00	0.00	0.00	0.00	0.00	0.00			
SGB6a	0.00	0.00	0.00	0.00	0.01	0.00			
SG750	9.80	0.41	12.56	3.14	25.92	25.55	101.46	37.82	1.60
SG720	9.86	0.37	12.53	3.14	25.90	25.35	102.16	38.07	1.42
SG660	11.61	0.09	14.08	3.52	29.30	29.09	100.70	39.62	0.31
SG630	10.55	0.07	12.78	3.20	26.61	25.48	104.41	39.65	0.28
SG600	10.08	0.08	12.23	3.06	25.45	25.80	98.62	39.61	0.31
SG600R	10.02	0.08	12.16	3.04	25.30	25.75	98.26	39.59	0.33
SGB6b	0.01	0.00	0.01	0.00	0.02	0.00			
SGB7a	0.01	0.00	0.00	0.00	0.01	0.00			
SG570	11.15	0.09	13.52	3.38	28.14	28.79	97.75	39.62	0.30
SG510	9.83	0.98	13.71	3.43	27.95	27.60	101.28	35.17	3.51
SG480	9.78	0.07	11.86	2.97	24.67	25.00	98.71	39.62	0.30
SG450	10.31	0.08	12.51	3.13	26.04	25.82	100.84	39.61	0.31
SG420	10.75	0.08	13.04	3.26	27.14	27.13	100.05	39.63	0.30
SG390	10.48	0.49	13.51	3.38	27.86	27.06	102.96	37.62	1.75
SGB7b	0.01	0.00	0.01	0.00	0.01	0.00			

Table D-1, continued.

Sample ID	g Ca	g Mg	g O	g C	g rock from ICP	g rock measured	% yield	mass % Ca	mass % Mg
SGB8a	0.00	0.00	0.00	0.00	0.00	0.00			
SGTOP	5.91	2.56	12.13	3.04	23.64	23.35	101.22	25.01	10.82
SG330	8.14	1.74	13.20	3.30	26.39	26.02	101.42	30.86	6.61
SG300R	10.53	0.08	12.78	3.20	26.60	25.01	106.35	39.61	0.31
SG300	7.37	1.57	11.93	2.98	23.85	22.79	104.66	30.90	6.58
SG270	8.57	0.87	11.98	3.00	24.41	24.58	99.33	35.12	3.55
SG240	8.41	1.26	12.56	3.14	25.36	24.94	101.69	33.14	4.97
SGB8b	0.00	0.00	0.00	0.00	0.01	0.00			
SGB9a	0.00	0.00	-0.01	0.00	-0.01	0.00			
SG180	8.98	0.79	12.32	3.08	25.17	25.52	98.66	35.68	3.14
SG150	8.04	1.63	12.85	3.22	25.74	26.32	97.79	31.22	6.35
SG120	7.55	1.94	12.87	3.22	25.58	25.96	98.53	29.50	7.59
SG090	9.16	1.01	12.96	3.24	26.37	26.95	97.86	34.74	3.82
SG060	8.64	0.88	12.08	3.02	24.63	25.24	97.58	35.10	3.56
SG000	9.00	1.76	14.26	3.57	28.59	29.29	97.62	31.49	6.16
SGB9b	0.00	0.00	-0.01	0.00	-0.01	0.00			
SGB10a	0.00	0.00	-0.01	0.00	-0.02	0.00			
SG-030	12.29	1.70	18.07	4.52	36.58	31.21	117.22	33.61	4.63
SG-060	9.65	1.42	14.37	3.60	29.04	29.87	97.24	33.23	4.90
SG-090	11.17	2.31	17.94	4.49	35.91	36.65	97.99	31.09	6.44
SG480D	10.16	0.08	12.32	3.08	25.64	25.25	101.57	39.62	0.31
SG780D	6.69	0.11	8.23	2.06	17.09	16.76	102.03	39.13	0.65
SG540D	9.73	0.07	11.80	2.95	24.55	24.88	98.66	39.63	0.30
SGB10b	0.00	0.00	0.00	0.00	-0.01	0.00			

Table D-2. Normalized masses of major elements of Nahef East limestone samples, from ICP data.

Sample ID	grams Ca	grams Mg	grams O	grams C
top250A	4.70	2.11	9.80	2.45
top 250B	4.70	2.11	9.80	2.45
top 125	4.40	2.13	9.48	2.37
-030B	7.34	1.57	11.90	2.98
TestA	7.73	0.04	9.33	2.33
TestB	7.65	0.03	9.23	2.31
SGTC	11.87	0.06	14.32	3.58
SGTD	12.78	0.06	15.42	3.86
SG870	10.80	0.08	13.10	3.28
SG690	10.12	0.18	12.49	3.12
SG540	11.25	0.08	13.64	3.41
SG360	9.94	0.07	12.03	3.01
SG210	9.44	0.79	12.86	3.22
SG030	10.53	1.52	15.61	3.91
SG960	10.28	0.08	12.47	3.12
SG930	10.21	0.19	12.60	3.15
SG900	10.08	0.32	12.71	3.18
SG840	6.81	2.43	12.95	3.24
SG810	10.23	0.18	12.59	3.15
SG780	10.16	0.17	12.51	3.13
SG750	9.66	0.41	12.38	3.10
SG720	9.65	0.36	12.27	3.07
SG660	11.53	0.09	13.98	3.50
SG630	10.10	0.07	12.24	3.06
SG600	10.22	0.08	12.40	3.10
SG600R	10.19	0.08	12.37	3.10
SG570	11.41	0.09	13.83	3.46
SG510	9.71	0.97	13.54	3.39
SG480	9.90	0.08	12.01	3.01
SG450	10.23	0.08	12.41	3.10
SG420	10.75	0.08	13.03	3.26
SG390	10.18	0.47	13.12	3.28
SGTOP	5.84	2.53	11.99	3.00
SG330	8.03	1.72	13.01	3.26
SG300R	9.91	0.08	12.02	3.01
SG300	7.04	1.50	11.40	2.85
SG270	8.63	0.87	12.06	3.02
SG240	8.27	1.24	12.35	3.09
SG180	9.10	0.80	12.49	3.12
SG150	8.22	1.67	13.14	3.29

Table D-2, continued

Sample ID	grams Ca	grams Mg	grams O	grams C
SG120	7.66	1.97	13.06	3.27
SG090	9.36	1.03	13.24	3.31
SG060	8.86	0.90	12.38	3.10
SG000	9.22	1.80	14.61	3.65
SG-030	10.49	1.45	15.42	3.86
SG-060	9.93	1.46	14.78	3.70
SG-090	11.39	2.36	18.31	4.58
SG480D	10.00	0.08	12.13	3.04
SG780D	6.56	0.11	8.07	2.02
SG540D	9.86	0.07	11.96	2.99

Table D-3 Duplicate runs of ICP analyses, mass % Ca and Mg, and % yields from each run.

Sample ID	% yield	mass % Ca	mass % Mg
-030ac (1)	108.53	33.18	4.94
-030ac (2)	117.22	33.61	4.63
000 (1)	96.63	30.56	6.83
000 (2)	97.62	31.49	6.16
060 (1)	98.06	34.92	3.69
060 (2)	97.58	35.10	3.56
090 (1)	99.20	34.54	3.96
090 (2)	97.86	34.74	3.82
150 (1)	86.07	34.73	3.82
150 (2)	97.79	31.22	6.35
210 (1)	101.47	35.65	3.16
210 (2)	104.11	35.88	3.00
300 (1)	104.39	29.83	7.35
300 (2)	104.66	30.90	6.58
300R (1)	100.18	39.66	0.28
300R (2)	106.35	39.61	0.31
570 (1)	95.26	39.62	0.31
570 (2)	97.75	39.62	0.30
630 (1)	103.90	39.67	0.27
630 (2)	104.41	39.65	0.28
690 (1)	100.19	39.00	0.75
690 (2)	103.25	39.06	0.70
840 (1)	121.86	27.14	9.29
840 (2)	123.09	26.79	9.54

Table D-4. Calcium and magnesium data from process duplicates—two rock aliquots from the same original sample, processed separately and run on the ICP. Despite differing yields, normalized Ca and Mg concentrations for two different aliquots are consistent.

Sample ID	% yield	% Ca	% Mg
SG480D	101.57	39.62	0.31
SG480	98.71	39.62	0.30
SG540D	98.66	39.63	0.30
SG540	103.18	39.65	0.29
SG780D	102.03	39.13	0.65
SG780	99.23	39.11	0.67

Table E-1. Internally-calibrated chloride concentrations for Nahel East limestone samples. Rock samples and blanks are corrected for average chloride concentrations (in italics) are uncorrected.

APPENDIX E—Chlorine data

Chloride was measured in undiluted aliquots of dissolved rock samples. Samples were run twice each on a Lachat QwikChem Automated Ion Analyzer. The Analyzer was calibrated using a series of six standards (blank, 0.1 $\mu\text{g g}^{-1}$ Cl, 0.25 $\mu\text{g g}^{-1}$ Cl, 0.5 $\mu\text{g g}^{-1}$ Cl, 1 $\mu\text{g g}^{-1}$ Cl, and 2 $\mu\text{g g}^{-1}$ Cl). These same standards were run with the actual samples, to check for analytical consistency and to provide an internal calibration. Data were processed in two different ways. First, the Analyzer produced chloride concentrations based on the initial calibration and spectral peak heights. Second, spectral peaks were printed out, digitized by hand, and calibrated using the internal standards. One run of half the samples produced an unprintable set of peaks (due to software problems). Both sets of data (Lachat and digitized peaks) were adjusted for the internal standard concentrations and averaged to calculate Cl concentrations; Cl concentrations in the rock samples (*not* standards) were corrected for the average chloride measured in the blanks from the same batch. Internally-calibrated chloride concentrations in both samples and standards, measured via the two different methods, are in Table E-1. Cl values used in calculating ^{36}Cl concentrations and in calculating f_{35} are in the "Ave. Cl" column.

Sample ID	Raw Cl ($\mu\text{g g}^{-1}$)	Raw Cl ($\mu\text{g g}^{-1}$)	Ave. Cl ($\mu\text{g g}^{-1}$)	St. Dev. ($\mu\text{g g}^{-1}$)
1	1.98	1.94	1.96	0.003
2	-0.04	-0.04	-0.04	0.003
3	0.19	0.18	0.19	0.016
4	0.76	0.77	0.77	0.011
5	0.31	0.30	0.30	0.009
6	0.43	0.43	0.43	0.004
7	-0.08	-0.07	-0.06	0.008
8	2.03	1.83	1.93	0.056
9	0.16	0.18	0.17	0.011
10	1.03	1.01	1.02	0.014
11	0.24	0.21	0.22	0.013
12	0.04	0.04	0.04	0.003
13	0.24	0.21	0.22	0.014

Table E-1. Internally-calibrated chloride concentrations for Nahef East limestone samples. Rock samples and blanks are corrected for chloride detected in blanks; standard concentrations (in italics) are uncorrected.

Sample ID	Run 1 Cl ($\mu\text{g/g}$)		Run 2 Cl ($\mu\text{g/g}$)		Ave. Cl ($\mu\text{g/g}$)	St. dev. ($\mu\text{g/g}$)
	Lachat	Digitized	Lachat	Digitized		
2	2.00	1.97	1.98	N/A	1.98	0.014
testb	error	0.34	0.31	N/A	0.32	0.020
blank a	-0.01	0.00	0.00	N/A	0.00	0.006
blank b	0.01	0.00	0.00	N/A	0.00	0.006
0.1	0.00	-0.02	-0.01	N/A	-0.01	0.012
-030B	3.31	3.25	3.34	N/A	3.30	0.044
250A	2.47	2.42	2.49	N/A	2.46	0.035
test a	0.35	0.38	0.39	N/A	0.37	0.019
0	0.13	0.15	0.14	N/A	0.14	0.010
125	3.06	2.98	3.04	N/A	3.03	0.039
250B	2.52	2.49	2.55	N/A	2.52	0.034
1	1.00	1.07	1.04	N/A	1.04	0.036
sgtc	0.17	0.23	0.17	N/A	0.19	0.031
sgtd	0.07	-0.05	0.10	N/A	0.04	0.082
0.5	0.48	0.46	0.45	N/A	0.46	0.014
2	2.00	2.01	1.99	N/A	2.00	0.010
B4a	0.04	0.02	0.02	N/A	0.03	0.014
870	0.17	0.18	0.18	N/A	0.17	0.006
0.1	0.21	0.21	0.19	N/A	0.20	0.012
690	0.22	0.17	0.20	N/A	0.20	0.027
540	0.26	0.25	0.27	N/A	0.26	0.010
0	-0.06	-0.05	-0.06	N/A	-0.06	0.003
360	0.17	0.18	0.20	N/A	0.18	0.013
210	0.23	0.19	0.23	N/A	0.22	0.022
1	0.99	0.94	1.00	N/A	0.98	0.028
030(ac)	1.33	1.16	1.32	N/A	1.27	0.094
B4b	-0.04	-0.02	-0.02	N/A	-0.03	0.014
0.25	0.22	0.24	0.23	N/A	0.23	0.007
2	1.98	1.99	1.99	N/A	1.98	0.008
B5a	-0.04	-0.04	-0.04	N/A	-0.04	0.003
960	0.19	0.22	0.19	N/A	0.20	0.016
0.1	0.16	0.17	0.18	N/A	0.17	0.011
930	0.31	0.30	0.29	N/A	0.30	0.009
900	0.43	0.43	0.44	N/A	0.43	0.004
0	-0.06	-0.07	-0.05	N/A	-0.06	0.008
840	2.02	1.93	2.04	N/A	1.99	0.056
810	0.16	0.16	0.18	N/A	0.17	0.011
1	1.03	1.01	1.02	N/A	1.02	0.014
780	0.24	0.21	0.22	N/A	0.22	0.013
B5b	0.04	0.04	0.04	N/A	0.04	0.003
0.25	0.24	0.25	0.22	N/A	0.24	0.014

Table E-1, continued.

Sample ID	Run 1 Cl ($\mu\text{g/g}$)		Run 2 Cl ($\mu\text{g/g}$)		Average Cl ($\mu\text{g/g}$)	St. dev. ($\mu\text{g/g}$)
	Lachat	Digitized	Lachat	Digitized		
2	<i>error</i>	1.98	2.01	N/A	2.00	0.017
B6a	-0.03	-0.01	-0.01	N/A	-0.02	0.012
750	0.37	0.36	0.39	N/A	0.37	0.014
0.1	0.12	0.11	0.13	N/A	0.12	0.011
720	0.39	0.39	0.38	N/A	0.39	0.005
660	0.19	0.25	0.21	N/A	0.22	0.030
0	32.65	-0.09	-0.07	N/A	10.83	18.894
630	0.25	0.22	0.20	N/A	0.22	0.026
600	0.22	0.21	0.18	N/A	0.20	0.023
1	0.94	0.96	0.95	N/A	0.95	0.011
600R	0.38	0.35	0.41	N/A	0.38	0.030
B6b	0.02	0.01	0.01	N/A	0.01	0.009
0.25	0.34	0.37	0.33	N/A	0.34	0.024
2	2.00	1.92	1.97	N/A	1.96	0.040
B7a	0.03	0.05	0.03	N/A	0.04	0.015
570	0.21	0.19	0.21	N/A	0.20	0.013
0.1	0.03	0.08	0.10	N/A	0.07	0.034
510	0.80	0.67	0.81	N/A	0.76	0.078
480	0.23	0.24	0.21	N/A	0.23	0.014
0	0.09	-0.10	-0.05	N/A	-0.02	0.099
450	0.35	0.30	0.33	N/A	0.33	0.026
420	0.40	0.33	0.37	N/A	0.37	0.034
1	1.01	1.11	1.05	N/A	1.05	0.050
390	0.45	0.37	0.40	N/A	0.40	0.039
B7b	-0.03	-0.05	-0.03	N/A	-0.04	0.015
0.25	0.22	0.35	0.28	N/A	0.28	0.064
2	2.00	2.02	1.99	1.96	1.99	0.013
B8a	0.12	0.09	0.12	0.09	0.10	0.018
330	1.09	1.04	1.09	1.09	1.08	0.028
0.1	0.30	0.29	0.31	0.32	0.30	0.013
300	1.71	1.54	1.73	1.73	1.68	0.107
300R	0.22	0.21	0.26	0.24	0.23	0.029
0.5	0.46	0.46	0.46	0.48	0.46	0.000
0	-0.12	-0.09	-0.13	-0.15	-0.12	0.021
270	0.52	0.48	0.53	0.45	0.49	0.023
240	0.69	0.58	0.69	0.63	0.65	0.062
1	0.92	0.95	0.93	0.96	0.94	0.015
SGTOP	2.06	1.96	2.08	1.38	1.87	0.065
B8b	-0.12	-0.09	-0.12	-0.09	-0.10	0.018
0.25	0.25	0.25	0.25	0.25	0.25	0.002

Table E-1, continued

Sample ID	Run 1 Cl ($\mu\text{g/g}$)		Run 2 Cl ($\mu\text{g/g}$)		Ave. Cl ($\mu\text{g/g}$)	St. dev. ($\mu\text{g/g}$)
	Lachat	Digitized	Lachat	Digitized		
2	1.95	2.03	1.95	1.95	1.97	0.047
B9a	0.05	0.14	0.05	0.04	0.07	0.050
180	0.71	0.59	0.72	0.68	0.67	0.074
0.1	0.06	0.13	0.07	0.08	0.08	0.041
150	1.68	1.62	1.70	1.64	1.66	0.042
120	1.88	1.83	1.88	1.86	1.86	0.031
0.5	0.49	0.53	0.44	0.51	0.49	0.044
0	-0.07	-0.02	-0.08	-0.06	-0.06	0.036
090	0.77	0.70	0.78	0.77	0.75	0.042
060	0.45	0.41	0.49	0.48	0.46	0.043
1	0.98	0.82	0.98	1.04	0.95	0.094
000	1.51	1.45	1.49	1.52	1.49	0.031
B9b	-0.05	-0.14	-0.05	-0.04	-0.07	0.050
0.25	0.26	0.33	0.28	0.30	0.29	0.033
2	1.98	2.01	1.97	2.00	1.99	0.021
B10a	-0.03	-0.03	-0.05	-0.03	-0.04	0.009
780D	0.25	0.26	0.30	0.34	0.29	0.029
0.1	0.12	0.11	0.11	0.16	0.12	0.005
540D	0.32	0.30	0.38	0.35	0.34	0.037
480D	0.45	0.46	0.48	0.53	0.48	0.015
0.5	0.50	0.55	0.51	0.49	0.51	0.025
0	-0.07	-0.05	-0.08	-0.05	-0.06	0.014
-030	1.34	1.47	1.31	1.07	1.30	0.081
-060	1.13	1.10	1.11	1.16	1.12	0.013
1	1.01	0.98	1.02	0.97	1.00	0.024
-090	1.47	1.36	1.45	1.42	1.43	0.060
B10b	0.03	0.03	0.05	0.03	0.04	0.009
0.25	0.31	0.29	0.31	0.30	0.30	0.013

Element	μ -capture probability relative to oxygen
Ca	1.90
Mg	0.93
O	1
C	0.77

(Capture probabilities are from von Egidy and Harman, 1982 and Knight et al., 1980)

f_{Ca} is calculated by dividing the product of the molar concentration of Ca and its muon capture probability by the sum of the products of all of the major element molar concentrations and probabilities. For pure limestone (CaCO_3), f_{Ca} is:

$$\frac{1.90}{(1.90) + (0.77) + (1.00)} = 0.3351 \quad (\text{F-1})$$

APPENDIX F— Y_{ca} scaling for muon capture reactions

The number of ^{36}Cl atoms created by muon capture by calcium in limestone (Y_{ca}) is dependent on the molar concentrations of the major elements in the rock (Ca, Mg, O, and C) [von Egidy and Hartman, 1982] and the fraction of negative muons stopped by Ca compared to those stopped by the other elements ($f_{c,ca}$). For pure limestone, Y_{ca} is 0.012 atoms ^{36}Cl (stopped μ^-)⁻¹ (Stone et al, 1998). The presence of Mg in the limestone will change Y_{ca} ; the presence of Mg in the crystal lattice dilutes the amount of Ca, decreasing Y_{ca} ; however, Mg is less likely to capture muons than Ca, so the scaling also uses the muon capture probabilities of the major elements in addition to their molar concentrations.

I have scaled Y_{ca} for the individual chemistry of each rock sample by first calculating $f_{c,ca}$ for each sample, and then scaling Y_{ca} for that given $f_{c,ca}$.

The negative muon capture probabilities for the major elements found in carbonate rocks are expressed in terms relative to the muon capture probability of oxygen.

Table F-1. Muon capture probabilities of major elements found in carbonates.

Element	μ^- capture probability relative to oxygen
Ca	1.90
Mg	0.93
O	1
C	0.77

(Capture probabilities are from von Egidy and Hartman, 1982 and Knight et al., 1980)

$f_{c,ca}$ is calculated by dividing the product of the molar concentration of Ca and its muon capture probability by the sum of the products of all of the major element molar concentrations and probabilities. For pure limestone (CaCO_3), $f_{c,ca}$ is:

$$\frac{1.90}{1(1.90) + 1(0.77) + 3(1.0)} = 0.3351. \quad (\text{F-1})$$

For pure dolomite ($\text{CaMg}(\text{CO}_3)_2$), $f_{c,\text{Ca}}$ is:

$$\frac{(1.90)}{(1.90) + (0.93) + 2(0.77) + 6(1.0)} = 0.1832. \quad (\text{F-2})$$

For all $f_{c,\text{Ca}}$ in between, the calculation follows the form:

$$f_{c,\text{Ca}} = \frac{x(1.90)}{x(1.90) + (2-x)(0.93) + 2(0.77) + 6(1.0)}. \quad (\text{F-3})$$

where x is the molar concentration of Ca in the limestone and $(2-x)$ is the molar concentration of the Mg. The combined molar concentration of Mg and Ca should be 2.

To scale Y_{ca} (which was calculated using the $f_{c,\text{Ca}}$ for pure limestone), I have done the following calculation:

$$Y_{Ca} = 0.012 \left(\frac{f_{c,\text{Ca}}}{0.3351} \right). \quad (\text{F-4})$$

Table F-2. Molar concentrations of major elements, $f_{c,Ca}$, and Y_{ca} for each sample

Sample ID	Molar fraction Ca	Molar fraction Mg	Molar fraction O	Molar fraction C	$f_{c,Ca}$	Y_{ca}
SGTOP	0.117	0.083	0.6	0.2	0.211	0.008
TOP250A	0.115	0.085	0.6	0.2	0.208	0.007
TOP250B	0.115	0.085	0.6	0.2	0.208	0.007
TOP125	0.111	0.089	0.6	0.2	0.201	0.007
SG960	0.198	0.002	0.6	0.2	0.332	0.012
SG930	0.194	0.006	0.6	0.2	0.327	0.012
SG900	0.190	0.010	0.6	0.2	0.321	0.012
SG870	0.198	0.002	0.6	0.2	0.332	0.012
SG840	0.126	0.074	0.6	0.2	0.225	0.008
SG810	0.195	0.005	0.6	0.2	0.327	0.012
SG780	0.195	0.005	0.6	0.2	0.327	0.012
SG780D	0.195	0.005	0.6	0.2	0.328	0.012
SG750	0.187	0.013	0.6	0.2	0.317	0.011
SG720	0.188	0.012	0.6	0.2	0.319	0.011
SG690	0.194	0.006	0.6	0.2	0.327	0.012
SG660	0.197	0.003	0.6	0.2	0.332	0.012
SG630	0.198	0.002	0.6	0.2	0.332	0.012
SG600	0.197	0.003	0.6	0.2	0.332	0.012
SG600R	0.197	0.003	0.6	0.2	0.331	0.012
SG570	0.198	0.002	0.6	0.2	0.332	0.012
SG540	0.198	0.002	0.6	0.2	0.332	0.012
SG540D	0.198	0.002	0.6	0.2	0.332	0.012
SG510	0.172	0.028	0.6	0.2	0.295	0.011
SG480	0.198	0.002	0.6	0.2	0.332	0.012
SG480D	0.197	0.003	0.6	0.2	0.332	0.012
SG450	0.197	0.003	0.6	0.2	0.332	0.012
SG420	0.198	0.002	0.6	0.2	0.332	0.012
SG390	0.186	0.014	0.6	0.2	0.315	0.011
SG360	0.198	0.002	0.6	0.2	0.332	0.012
SG330	0.148	0.052	0.6	0.2	0.259	0.009
SG300	0.148	0.052	0.6	0.2	0.260	0.009
SG300R	0.197	0.003	0.6	0.2	0.332	0.012
SG270	0.171	0.029	0.6	0.2	0.294	0.011
SG240	0.160	0.040	0.6	0.2	0.278	0.010
SG210	0.176	0.024	0.6	0.2	0.301	0.011
SG180	0.175	0.025	0.6	0.2	0.299	0.011
SG150	0.150	0.050	0.6	0.2	0.262	0.009
SG120	0.140	0.060	0.6	0.2	0.248	0.009
SG090	0.169	0.031	0.6	0.2	0.291	0.010
SG060	0.171	0.029	0.6	0.2	0.294	0.011
SG030	0.132	0.038	0.6	0.2	0.280	0.010
SG000	0.151	0.049	0.6	0.2	0.264	0.009
SG(-030)	0.163	0.037	0.6	0.2	0.282	0.010
SG(-030)B	0.148	0.052	0.6	0.2	0.259	0.009
SG(-060)	0.161	0.039	0.6	0.2	0.279	0.010
SG(-090)	0.149	0.051	0.6	0.2	0.261	0.009

APPENDIX G—Calculation of f_{35}

The ability of ^{35}Cl atoms to capture neutrons and form ^{36}Cl (f_{35}) in a rock depends on the concentration of ^{35}Cl and the ability of ^{35}Cl atoms to capture neutrons (compared to the ability of the other atoms nearby) (Fabryka-Martin, 1988; Liu et al., 1994). To calculate f_{35} in the Nahef East samples, I have measured the concentration of Cl, major elements (Ca, Mg, C, and O), and certain trace elements that have a strong ability to capture neutrons (B, Sm, Gd). f_{35} is expressed in terms of barns (10^{-24} g cm^{-2}). N is the number of atoms of a given element (expressed in ppm by atom). f_{35} is the capture cross section of ^{35}Cl divided by the total capture cross section for all elements (i) in the rock (equation G-1):

$$f_{35} = \frac{N_{^{35}\text{Cl}} \sigma_{^{35}\text{Cl}}}{\sum N_i \sigma_i} \quad (\text{G-1})$$

Thermal neutron capture cross sections used for the calculation of f_{35} (seen in Chapter 3, Table 1) are in Table G-1.

Table G-1. Thermal neutron capture cross sections for elements in Nahef East fault samples (values from Fabryka-Martin, 1998; Lide, ed., 1994)

Element (i)	σ_i (barn)
Ca	0.43
Mg	0.063
C	0.0034
O	0.0002
^{35}Cl	48
B	767
G d	41560
Sm	9640

APPENDIX H—³⁶Cl production from radiogenic (α,n) reactions

Calculation of the neutron production rate from U-Th series alpha decay. All numbers and equations are taken directly from Fabryka-Martin, 1988. The neutron production rate from alpha decay can be estimated by the following equation:

$$P(n, a) = X [U] + Y [Th] \quad \text{neutrons (g rock)}^{-1} \text{ yr}^{-1} \quad (\text{H-1})$$

Where [U] and [Th] are in ppm (measured using ICP-MS) and X and Y are calculated as follows:

$$X = \sum_i S_i F_i Y^U / \sum_i S_i F_i \quad \text{neutrons (g rock)}^{-1} \text{ yr}^{-1} (\text{ppm U})^{-1}, \quad (\text{H-2})$$

$$Y = \sum_i S_i F_i Y^{Th} / \sum_i S_i F_i \quad \text{neutrons (g rock)}^{-1} \text{ yr}^{-1} (\text{ppm Th})^{-1}, \quad (\text{H-3})$$

where S_i is the mass stopping power of element i for α -particles of a given energy (MeV (g rock)⁻¹ yr⁻¹), F_i is the fractional abundance of element i (ppm), and Y^U and Y^{Th} are neutron yields for element i per ppm U and Th, respectively.

Table H-1. Mass stopping power and neutron yields for the most common light elements found in Nahef samples.

Target element i	MSP (S_i)	Y^U	Y^{Th}
Li	548	21.1	9.6
B	527	62.3	19.2
C	561	0.45	0.18
O	527	0.23	0.079
Mg	461	5.8	2.6
Ca	428	0	0

X and Y were calculated for each of the Nahef samples using eqs. H-2 and H-3 and the values in Table H-1, as well as the individual light element concentrations (Table H-2). Using the calculated values for X and Y, and the measured values for [U] and [Th], I then calculated the production of neutrons per year. From these neutron production rates, I then calculated the number of ³⁶Cl atoms produced per year. Finally, I calculated the equilibrium abundances of ³⁶Cl based on production and radiogenic decay. Because we did not have U or Th data from the

“TOP” sample (TOP250A, TOP250B, and TOP125), we assumed X and Y for these samples is equal to those calculated for SGTOP.

Table H-2. Light element concentrations (ppm), X and Y values, [U] and [Th] concentrations, and calculated steady-state abundances of ³⁶Cl from alpha decay thermal neutrons.

Sample ID	[Ca] ppm	[Mg] ppm	[O] ppm	[C] ppm	[Li] ppm	[B] ppm	X	Y	[U] ppm	[Th] ppm	Steady-State ³⁶ Cl abundance, 10 ³ atom (gm rock) ⁻¹
SGTOP	250093	106920	507053	126879	0.57	2.26	0.77	0.33	5.92	0.03	16.52
*TOP250A	250093	106920	507053	126879	0.57	2.26	0.77	0.33	5.92	0.03	17.57
TOP250B	250093	106920	507053	126879	0.57	2.26	0.77	0.33	5.92	0.03	18.46
TOP125	250093	106920	507053	126879	0.57	2.26	0.77	0.33	5.92	0.03	21.17
SG960	396278	2967	476271	119177	0.11	0.00	0.19	0.07	4.17	0.04	1.07
SG930	390183	7414	484074	121129	0.17	0.15	0.22	0.08	6.86	0.09	0.50
SG900	383549	11809	469561	117498	0.18	0.21	0.24	0.09	4.30	0.10	0.78
SG870	396278	2931	470468	117725	0.00	0.00	0.19	0.07	4.83	0.08	0.62
SG840	267924	77495	413715	103524	0.63	2.25	0.66	0.28	6.39	0.14	8.15
SG810	391119	6716	482281	120681	0.14	0.11	0.21	0.08	3.64	0.04	0.47
SG780	391130	6751	485395	121460	0.10	0.00	0.21	0.08	3.60	0.07	0.25
SG780D	391347	6413	472039	118118	0.10	0.00	0.21	0.08	3.60	0.07	0.47
SG750	378224	15760	477582	119505	0.16	0.16	0.26	0.10	3.96	0.08	0.54
SG720	380746	13874	473729	118541	0.19	0.28	0.25	0.10	4.23	0.09	0.55
SG690	390644	6827	466600	116757	0.10	0.00	0.21	0.08	3.49	0.03	0.24
SG660	396187	3037	477177	119404	0.00	0.00	0.19	0.07	3.98	0.06	0.24
SG630	396537	2688	460139	115140	0.11	0.00	0.19	0.07	4.82	0.10	0.28
SG600	396070	3186	487283	121932	0.00	0.00	0.20	0.07	3.94	0.05	0.27
SG600R	395894	3327	489070	122380	0.00	0.17	0.20	0.07	4.40	0.10	0.45
SG570	396237	3092	491570	123005	0.00	0.00	0.20	0.07	4.37	0.08	0.26
SG540	396453	2779	465642	116517	0.00	0.00	0.19	0.07	4.44	0.07	0.31
SG540D	396274	3036	487035	121870	0.00	0.00	0.19	0.07	4.44	0.07	0.49
SG510	351659	34670	484305	121187	0.22	0.42	0.37	0.15	4.18	0.12	1.34
SG480	396234	3064	486763	121802	0.11	0.00	0.19	0.07	4.32	0.09	0.42
SG480D	396158	3032	473109	118386	0.11	0.00	0.19	0.07	4.32	0.09	0.50
SG450	396124	3078	476533	119242	0.00	0.00	0.19	0.07	4.18	0.09	0.42
SG420	396298	2977	480256	120174	0.00	0.00	0.19	0.07	4.07	0.07	0.48
SG390	376185	16956	471063	117874	0.17	0.21	0.27	0.11	4.14	0.10	0.58
SG360	396677	2641	468951	117345	0.00	0.13	0.19	0.07	3.76	0.10	0.37
SG330	308594	65190	493151	123401	0.70	1.56	0.54	0.23	4.39	0.07	3.24
SG300	308991	62896	477782	119555	0.51	1.55	0.53	0.22	4.83	0.04	5.44
SG300R	396064	2959	451866	113070	0.00	0.18	0.19	0.07	3.18	0.06	0.49
SG270	351159	35712	493912	123591	0.31	0.79	0.37	0.15	3.60	0.07	0.91
SG240	331407	48867	486823	121817	0.41	1.08	0.45	0.19	3.54	0.06	1.24
SG210	358799	28790	469596	117507	0.18	0.51	0.34	0.14	1.71	0.04	0.39
SG180	356805	31835	495982	124109	0.28	0.79	0.35	0.14	3.54	0.06	1.11
SG150	312234	64929	510613	127770	0.59	1.77	0.53	0.22	3.23	0.04	4.51
SG120	294973	77048	510676	127786	0.82	2.26	0.59	0.25	3.90	0.01	5.37
SG090	347401	39012	502185	125661	0.36	1.12	0.39	0.16	4.20	0.07	2.05
SG060	350989	36476	502790	125813	0.30	0.96	0.38	0.15	4.65	0.12	1.18
SG030	333658	47068	484209	121163	0.62	2.17	0.44	0.18	4.83	0.08	4.01
SG000	314887	63086	510900	127842	0.63	1.97	0.52	0.22	6.04	0.05	5.19
SG-030	336061	39534	421423	105452	0.58	1.81	0.41	0.17	4.50	0.04	4.77

* X and Y for the TOP samples are assumed to be the same as they are for the SGTOP sample. The difference in the steady-state ³⁶Cl abundance is due to differences in f_{35} .

APPENDIX I—Production rates from neutrons on tilted surfaces

Since I am calculating ^{36}Cl accumulation on a tilted, rather than horizontal, surface, we must consider the geometry of the fault scarp in the ^{36}Cl production rate equations. For a fault scarp of a given angle (in this case, 51°), part of the neutron flux will first travel through the chalk or strikes the scarp directly; the remaining neutron flux travels through the limestone on the back side of the scarp (Figure I-1).

Several considerations go into calculating production rates at depth on tilted surfaces. First, the neutron flux varies in intensity based on incidence angle. This means that I must integrate the flux over the angles required (51° and 129° for the footwall and hanging wall respectively). Also, Λ_{sp} (the effective neutron attenuation length) will be different for a tilted surface than for a horizontal surface. For neutron flux calculations I use an effective attenuation length (Λ_{sp}) of 210 g cm^{-2} (calculated by John Stone). This is the Λ_{sp} value that results in a proportion of e^{-1} neutrons passing through rock at depth $z = 160 \text{ g cm}^{-2}$ beneath a tilted surface, relative to the number of neutrons passing through the surface.

In order to calculate neutron intensities through the two fault blocks, John Stone has integrated the neutron flux that travels through each of the fault blocks. For calculating the production rate through the hanging wall (chalk), he has set up the integral through two sets of quadrants based on the tilt of the scarp face (I-1):

$$P_{zc} = P_{sp}(0) \left(\begin{array}{l} 2 \int_0^{0.5\pi} \int_{\text{ArcTan}(\text{Tan}\alpha\text{Sin}\phi)}^{0.5\pi} (\text{Sin}[\Theta]^{2.3} \text{Cos}[\Theta]) e^{\left[\frac{-z/h}{\text{Sin}[\Theta]210} \right]} d\Theta d\phi + \\ 2 \int_0^{0.5\pi} \int_0^{0.5\pi} (\text{Sin}[\Theta]^{2.3} \text{Cos}[\Theta]) e^{\left[\frac{-z/h}{\text{Sin}[\Theta]210} \right]} d\Theta d\phi \end{array} \right) / (2\pi/3.3) \quad (\text{I-1})$$

where P_{zc} is the ^{36}Cl production rate from calcium spallation at depth z , and $P_{sp}(0)$ is the surface production rate. Θ is the strike (horizontal) angle, ϕ is the angle between the horizon and the zenith, and α is the angle of the scarp (all angles are in radians) (figure I-1). The first part of the integral integrates the neutron flux over the “updip,” quadrants (the wedge of chalk between the scarp face and the vertical plane parallel to the strike of the scarp). The second integral integrates the neutron flux over the “downdip” quadrants (the half of the hemisphere below the vertical

plane)(figure I-1). Dividing the sum of the two integrals by $2\pi(3.3)^{-1}$ normalizes the value of the integral to the production rate of the unobstructed overlying surface.

Setting up the integral to calculate the production rate through the footwall (limestone) is very similar, the only major difference being only having to set the integral up for two quadrants (I-2):

$$P_{zl} = P_{sp}(0) \left(2 \int_0^{0.5\pi} \int_0^{\text{ArcTan}(\alpha)\text{Sin}(\phi)} (\text{Sin}[\Theta]^{-2.3} \text{Cos}[\Theta]) e^{-[z/\text{Sin}(\Theta)210]} \right) / (2\pi/3.3) \quad (\text{I-2})$$

Using these two integrals, we calculate that the ^{36}Cl production rate from Ca spallation on the 51° scarp surface from the hanging wall is 88.5% what it would be on a horizontal surface. We then calculated the production rate of ^{36}Cl at various depths for the two respective fault blocks. From these two production at depth curves, we created two polynomial fit equations that describe production at depth for both the footwall and the hanging wall (Table I-1). These production at depth curves are scaled for pure calcite, in order to scale them to individual sample chemistries one must multiply by a Ca scaling factor.

The polynomial equations follow the form:

$$P_{\text{spl}}(z) = P_{\text{sp}}(0)[\text{Ca}](P_{\text{zchalk}}) \quad (\text{I-3})$$

$$P_{\text{zchalk}} = az^5 + bz^4 + cz^3 + dz^2 + ez + f \quad (\text{I-4})$$

$P_{\text{spc}}(z)$ is the same, only using the coefficients for $P_{\text{zlimestone}}$.

Table I-1. Coefficients for Ca-spallation ^{36}Cl production at depth equation, derived from the integrations in equations I-1 and I-2.

	<i>a</i>	<i>b</i>	<i>c</i>	<i>d</i>	<i>e</i>	<i>f</i>
P_{zchalk}	-3.13×10^{-15}	2.584×10^{-11}	-2.911×10^{-8}	1.622×10^{-5}	-0.0053	0.885
$P_{\text{zlimestone}}$	-3.443×10^{-14}	3.858×10^{-11}	-1.910×10^{-8}	5.682×10^{-6}	-1.100×10^{-3}	0.115

These polynomials result in approximately 88.5% of neutrons passing through the chalk, and 11.5% passing through the limestone en route to the scarp face. In order to simplify the numerical model, rather than use the polynomial approximation, we have apportioned 88.5% of the neutron flux to the hanging wall, and the remaining 11.5% to the footwall.

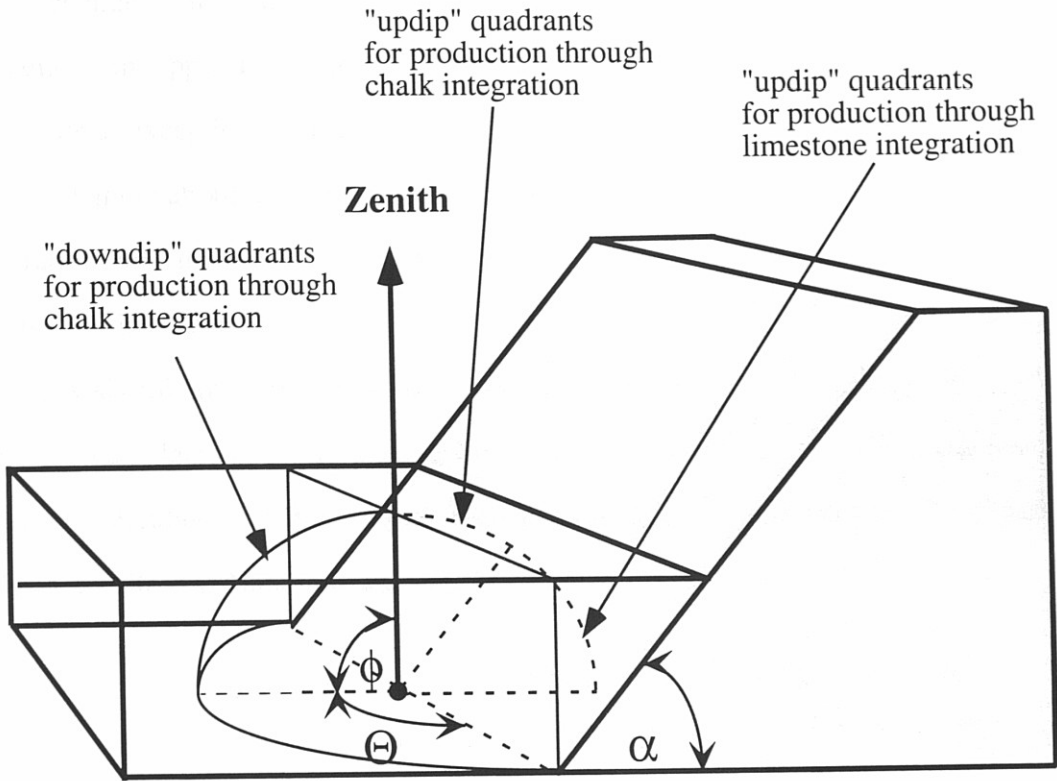


Figure I-1. Geometric relationships used for integrating neutron intensities on tilted surfaces. A portion of the cosmic ray flux travels through the footwall while the majority of cosmic rays travel through the hanging wall to reach the fault scarp surface. In order to determine the proportion of cosmic rays traveling through each fault block, I have integrated the neutron flux (which varies based on incidence angle) over horizontal angle (Θ) and dip angle (ϕ) for a scarp of tilt α . Solving the integration results in a production at depth curve as described in Table I-1

APPENDIX J—Muon scaling on tilted surfaces

The calculation of the muon flux at a given depth beneath a tilted surface is quite complicated. Both the number of muons reaching a surface and the energy spectrum of those muons change with incidence angle. The limits of the integration (based on scarp geometry) are the same as in Appendix I (Figure I-1), with the exception that the integration becomes inaccurate at exceptionally low incidence angles. As in Appendix I, (α) is the angle of the scarp, (Θ) is the angle about the horizon, and (Φ) is the incidence angle (Figure I-1). Because the integration fails at very low incidence angles, John Stone made the lower limits to incidence angles $\text{ArcSin}(z_h/23000)$ instead of 0 (this cuts out about the 5° of the horizon, very few muons reach any significant depth from these low angles). (I_v) is the vertical range spectrum of muons at depth (z), calculated and expressed as a polynomial shown in eq. J-1. This polynomial was originally calculated for Wombeyan, Australia, and has been corrected for the altitude of the Nahef East site (the Nahef samples are 37 (gm water equivalent) cm^{-2} deeper).

$$\log_{10}[I_v(z)] = 7.191 - 10.456 \log[z + 37] + 7.036 \log[z + 37]^2 - 1.977 \log[z + 37]^3 + 0.220 \log[z + 37]^4 - 0.008 \log[z + 37]^5 \quad (\text{J-1})$$

The muon stopping rate at depth for the hanging wall ($\Psi_{\mu^-(z)h}$) is (eq. J-2):

$$\Psi_{\mu^-(z)h} = 2 \int_0^{0.5\pi} \int_{\arctan[\tan(\alpha)\sin(\phi)]}^{0.5\pi} (I_v)(z_h/\sin[\Theta]) \sin[\Theta]^{n(z_h/\sin[\Theta])} \cos[\Theta] d\Theta d\phi + \pi \int_{\arcsin(z_h/23000)}^{0.5\pi} I_v(z_h/\sin[\Theta]) \sin[\Theta]^{n(z_h/\sin[\Theta])} \cos[\Theta] d\Theta \quad (\text{J-2})$$

and the footwall (eq. J-3):

$$\Psi_{\mu^-(z)f} = 2 \int_0^{0.5\pi} \int_{\arcsin[z_f/23000]}^{\arctan(\sin[\alpha]\sin[\phi])} (I_v)(z_f/\sin[\Theta]) \sin[\Theta]^{n(z_f/\sin[\Theta])} \cos[\Theta] d\Theta d\phi \quad (\text{J-3})$$

The sine exponent n in equations J-2 and J-3 varies with muon energy (range) in the following fashion (eq. J-4):

$$n(\text{range}) = 3.1 \exp^{[-10(\log_{10}(\text{range}) - 3.7)]} \quad (\text{J-4})$$

The integrations in J-2 and J-3 are then run at different depths (z_f) and (z_h) for the spectra of both (I_v) and (n). The resulting muon stopping rates at different depths for the hanging wall and footwall can be expressed as a polynomial of the form of equation J-5, with the coefficients shown in Table J-1.

$$\log_{10}[\Psi_{\mu}(z)] = a + b[\log_{10}(z)] + c[\log_{10}(z)]^2 + d[\log_{10}(z)]^3 + e[\log_{10}(z)]^4 \quad (\text{J-5})$$

Table J-1. Coefficients for the muon stopping rate at depth (z) for the hanging wall ($\Psi_{\mu}(z)h$) and footwall ($\Psi_{\mu}(z)f$).

	<i>a</i>	<i>b</i>	<i>c</i>	<i>d</i>	<i>e</i>
$\Psi_{\mu}(z)h$	3.905	-7.139	4.629	-1.190	0.097
$\Psi_{\mu}(z)f$	-0.434	-1.964	1.787	-0.535	0.0438

These polynomials result in approximately 90.5% of the total ^{36}Cl forming from cosmic rays traveling through the hanging wall, and only 9.5% from cosmic rays traveling through the footwall. To simplify the numerical model, I have multiplied the overall muon capture production rate at depth through the chalk by 0.905, and through the limestone by 0.095, for modeling ^{36}Cl accumulation.

APPENDIX K—Rock density

This appendix contains the code for the main program and sub-functions used to calculate the erosion rate. Shielding depths for neutrons and muons are often expressed in terms of $g\text{ cm}^{-2}$, the depth in cm multiplied by the density of the material. The density of five limestone samples and one chalk sample was measured by weighing a sample and measuring the volume using water displacement (Table K-1).

Table K-1. Density of limestone and chalk samples from the Nahef East fault, northern Israel.

Sample ID	Mass (gm)	Volume (cm ³)	Density
SG000	85.6	31.0	2.76
SG180	47.1	17.5	2.69
SG600	65.6	24.0	2.73
SG810	75.9	27.5	2.76
SG900	71.6	25.5	2.81
Chalk	33.0	12.3	2.75

APPENDIX L—MATLAB 5.6 model

This appendix contains the code for the main program and sub-functions used to calculate the erosion rate of the limestone and to generate model ^{36}Cl values, given different displacement histories. “%” indicates a comment; text with no function in the program.

Main Program

```
clear all;
% GENERAL VARIABLES
% z = depth of sample TODAY (g/cm2)
% ze = depth of sample throughout erosion history (for calculating initial abun. and erosion)
% e = erosion rate (cm/yr)
% Ydisp = years of displacement history

% INITIAL NUMBER OF 36CL ATOMS IN ALL SAMPLES AT START OF FAULTING HISTORY
% TO CALCULATE EROSION RATE, SET YDISP = 1 YEAR

% INCasp = # atoms in each sample from Ca spallation
% INTNsp = # atoms in each sample from spallation thermal neutrons
% NUfis = # atoms in each sample from U-fission
% NUTh = # atoms in each sample from U-Th alpha decay
% INCamz = # atoms in each sample from Ca muon capture
% INTncmz = # atoms in each sample from muon capture thermal neutrons
% INTNbz = # atoms in each sample from bremsstrahlung thermal neutrons

% STEP ONE, CALCULATE EROSION RATE

load e.dat; % Input erosion rate (you will vary this to
% get the "right" 36Cl value for the upper surface
lambda = 2.303e-06; % Decay constant of 36Cl
load Ydisp.dat; % years of displacement history (for calculating
% erosion rates, this = 1, for calculating
% model 36Cl values, use 20000
zv = z+Ydisp*e*2.75; % depth of each sample at today - Ydisp years, in g/cm2
load ze.dat; % A vector used to calculate steady-state abundances
% from muon reactions

% LOADING ALL VARIABLES
% ALL OF THESE FILES HAVE THE DATA FOR EACH SAMPLE IN THE EXACT SAME ORDER
% EACH FILE NEEDS TO HAVE THE EXACT SAME NUMBER OF INPUTS

% These files are specific to YOUR samples (each must have the same
% number of inputs), for the model to run you need all of these data files.
load ca.dat; % calcium data, mass %
load Yca.dat; % 0.012/(mass%Ca/40)
load z.dat; % today's vertical depth of sample, g/cm2
load f35.dat; % thermal neutron capture cross section for 35Cl
load U.dat; % ppm Uranium
load Th.dat; % ppm Thorium
load X.dat; % neutrons from U decay (Fabryka-Martin, 1988)
load Y.dat; % neutrons from Th decay (Fabryka-Martin, 1988)
load Cl36.dat; % measured 36Cl data from actual samples (atoms/gm rock)
load Cl36err.dat; % 1sigma error for each sample (AMS error only)
load k1.dat; % pre-exponent value, modified from Liu, 1995
```

```

load k2.dat;           % " " " "
load muonf.dat;       % Muon scaling factor for altitude and latitude
load neutf.dat;       % neutron scaling factor for altitude and latitude
%                     for muons (*NOT an input file, leave untouched*)

% CALCULATION OF EROSION RATE AND THE CL36 ABUNDANCES FOR EACH SAMPLE AT
% START OF FAULTING HISTORY

% FOR CALCULATING EROSION RATE, MAKE YDISP = 1
% FOR CALCULATING INITIAL ABUNDANCES, MAKE YDISP = 20000 (OR HOWEVER
% LONG FAULTING HISTORY SHOULD BE)

% Calculation of initial abundance due to Ca spallation
  [INCasp] = f_INCasp(ca,z,e,Ydisp,neutf);

% Calculation of initial abundance due to spallation TN
  [INTNsp] = f_INTNsp(f35,z,e,Ydisp,k1,k2,neutf);

% Calculation of initial abundance due to Ca muon capture
  [INCamz] = f_INCamz(Yca,e,z,ze,Ydisp,muonf);

% Calculation of initial abundances due to muon capture thermal neutrons
  [INTnmcz] = f_INTnmcz(f35,e,z,ze,Ydisp,muonf);

% Calculation of initial abundances from bremsstrahlung radiation
  [INTNbz] = f_INTNbz(f35,e,z,ze,Ydisp,muonf);

% Calculation of 36Cl from radiogenic reactions
% U-fission thermal neutrons
  [NUfis] = f_NUfis(f35,U);

% U-Th alpha decay thermal neutrons
  [NUTh] = f_NUTh(f35,U,Th,X,Y);

% TOTAL INITIAL ABUNDANCES

  INtotal = INCasp+INTNsp+NUTh+INCamz'+NUfis+INTnmcz'+INTNbz';

% TO SPEED THE RUNNING TIME OF THE PROGRAM, I CALCULATED INITIAL
% ABUNDANCES ONCE, SAVED THEM AS A DATA FILE, AND LOADED THOSE FOR
% SUBSEQUENT DISPLACEMENT SCENARIOS

% load intot.dat;
% CALCULATION OF 36Cl ACCUMULATION DURING A 20000 YEAR FAULTING HISTORY,
% CONSIDERING CHANGING DEPTHS WRT LIMESTONE AND CHALK, EROSION AND
% DISPLACEMENT

% CALCULATING 36Cl FOR A 20000 year history

count = 1;           % variable that steps through time
minCl = Cl36 - 2*Cl36err;%calculating "min" and "max" values to plot
maxCl = Cl36 + 2*Cl36err;
%
n = 7;               % NUMBER OF EVENTS + 1
for x=1:n             % LOOP THAT GOES THROUGH SUCCESSIVE EVENTS

```

```

WHEN = [8000 % WHEN EVENTS OCCUR (20000 - YEARS BP)
13500
14000
14500
15000
19000
21000]; % THIS IS A "DUMMY" EVENT TO MAKE THE LOOP CLOSE PROPERLY
%
HOWMUCH = [434 % SIZE OF DISPLACEMENT EVENTS IN g/cm2
434 % IN OUR MODEL, ALL EVENT SIZES ARE EQUAL
434
434
434
0];
end
%
% THIS IS WHERE PRODUCTION THROUGH TIME IS CALCULATED
%
delt2 = 10; % dealing in 10 year increments
Clc = 0; % at time 0, 36Cl produced from chalk side is 0
sClc = 0.88 .* intot; % initial value of 36Cl from chalk is 88% of INtotal
ClI = 0; % at time 0, 36Cl produced from limestone side is 0
sClI = 0.12 .* intot; % initial value of 36Cl from limestone is 12% of INtotal
zv = z + Ydisp * e * 2.75; % Depth at beginning of displacement
% history--lowest production rates possible for each
% sample, depth zv will become increasingly smaller
% as erosion and displacement take place
zl = zv; % starting depth wrt limestone is zv
zc = zv; % starting depth wrt chalk is zv
i = 0;
incze = (e * delt2 * 2.75); % in each 10 year increment, this much material lost
storevc = zeros(2000,1); % counts through 20,000 years, 10 yrs at a time
storevl = zeros(2000,1);
time = zeros(2000,1);
for t = 0:delt2:20000 % loop to calculate new depths at each timestep
i = i+1;
zl = zl - incze; % depth wrt limestone changes due to erosion only
if (t == WHEN(count)) % depth wrt chalk is dependent on faulting
zc = zc - (incze + HOWMUCH(count)); % calculate new depths wrt chalk
count = count + 1; % counter
else
zc = zc - incze; % erosion also affects depth wrt chalk
end
ii = find(zc <= 0); % Getting rid of negative numbers
zc(ii) = 0; % depth cannot be < 0
%
% FUNCTION THAT CALCULATES PRODUCTION RATE UNDER CHALK AT EACH TIME STEP
[Prodzvc] = f_Prodzvc(ca, Yca, zc, z, f35, U, Th, X, Y, Ydisp, e, muonf, neutf, k1, k2);
%
% FUNCTION THAT CALCULATES PRODUCTION RATE UNDER LIMESTONE AT EACH TIME STEP
[Prodzvl] = f_Prodzvl(ca, Yca, zl, z, f35, U, Th, X, Y, Ydisp, e, muonf, neutf, k1, k2);
%
time(i) = t;
%
Clc = (Prodzvc * delt2); % production rate from chalk side
sClc = (sClc + Clc)*(exp(-lambda * delt2)); % sum of 36Cl produced and lost %
from chalk

```



```

Cll = (Prodzvl * delt2); % production rate from limestone side
sCll = (sCll + Cll) * (exp(-lambda * delt2)); % sum of 36Cl produced
% and lost from limestone
sumCl = sCll + sClc; % total 36Cl summed at end of loop
end
% SIMPLE LEAST SQUARES FIT TO MEASURED DATA
% THESE WILL PRINT AT THE END OF EACH RUN. LOWER LS VALUES INDICATE
% A BETTER FIT THAN HIGH LS VALUES.
ind = find(z > 0); % do not include the samples from the upper surface
LSfit = sqrt((sumCl(ind) - Cl36(ind)).^2); % absolute value of all variances
LS = sum(LSfit) % sum of all variance
LS2 = mean(LSfit) % average of all variance
%
% PLOT RESULTS TO CHECK THE MODEL FIT, VISUALLY
%
plot (sumCl,-z,'b.',Cl36,-z,'r.',minCl,-z,'k.',maxCl,-z,'k:')
legend('model 36Cl','measured 36Cl', 'error', 4)
title('model and measured 36Cl')
Xlabel ('36Cl concentration')
Ylabel ('depth')

```

Nine Sub-functions, in order of appearance in the MAIN program

1

```

function [INCasp] = f_INCasp(ca,z,e,Ydisp,neutf)
% CALCULATION OF 36Cl ABUNDANCE FROM Ca SPALLATION IN ALL SAMPLES,
% GIVEN THEIR CHEMISTRY, THE EROSION RATE, AND DEPTH BENEATH SURFACE
%
lambda = 2.303e-06; % Decay constant of Cl36
Zt = z+Ydisp*e*2.75; % calculation of starting depth in cm
Psp = 48.8; % Production rate at surface from Ca spallation
Lsp = 160; % Attenuation rate of neutrons
rho = 2.75; % Density of limestone
INCasp = (neutf*Psp*(ca./100).*exp(-Zt./Lsp))/(lambda+(e*rho)/Lsp);

```

2

```

function [INTNsp] = f_INTNsp(f35,z,e,Ydisp,k1,k2,neutf)
% 36Cl ABUNDANCE FROM SPALLATION THERMAL NEUTRONS, GIVEN SAMPLE
% CHEMISTRY, EROSION RATE, DEPTH BENEATH SURFACE
lambda = 2.303e-06; % Decay constant of Cl36
Zt = z+Ydisp*e*2.75; % calculation of starting depth in cm
PTNsp = 560; % Production rate of spallogenic neutrons at ground level
%K1 = 1.17; % term to describe neutron production
%K2 = -0.89; % term to describe loss of albedo neutrons
Lsp = 160; % attenuation length
Lth = 33; % thermal neutron diffusion in limestone
rho = 2.75; % density of limestone in g/cm3
INTNsp = neutf*PTNsp*f35.*(((k1.*exp(-Zt/Lsp))./(lambda+(e*rho/Lsp)))+
+((k2.*exp(-Zt/Lth))./(lambda+(e*rho/Lth))));

```

3

```

function [INCamz] = f_INCamz(Yca,e,z,ze,Ydisp,muonf)
% CALCULATION OF 36Cl ABUNDANCES IN ALL SAMPLES FROM Ca MUON CAPTURE
% GIVEN SAMPLE CHEMISTRY, EROSION RATE, AND DEPTH BENEATH SURFACE
%
lambda = 2.303e-06; % Decay constant of Cl36 Ydisp = 20000;
Zt = z+Ydisp*e*2.75; % Depth at a given time before present

```

```

delz = max(diff(ze)); % calculation of change in depth for each time step
delt = delz/(e*2.75); % calculation of timestep
ii = find(ze <= 100);
ze(ii) = 100;
Ymz = 10.^(1.586+1.709.*(log10(ze))+(-1.817).*((log10(ze)).^2)+0.9642.*((log10(ze)).^3)...
+(-.2384).*((log10(ze)).^4)+.01955.*((log10(ze)).^5));
for j = 1:length(Yca) % Calculating INCamz for each sample
    INCasum = 0;
    Zt = z(j)+Ydisp*e*2.75; % calculation of starting depth in cm
    for i=length(ze):-1:(Zt/10) % summing 36Cl for each timestep
        INCasum = ((muonf*Yca(j) * Ymz(i)*delt)+INCasum) * (exp(-lambda*delt));
    end
    INCamz(j) = INCasum;
End

```

4

```

function [INTnmcz] = f_INTnmcz(f35,e,z,ze,Ydisp,muonf)
% 36Cl FROM MUON CAPTURE THERMAL NEUTRONS, GIVEN SAMPLE CHEMISTRY,
% EROSION RATE, AND TIME BEFORE PRESENT (DEPTH)
    lambda = 2.303e-06; % Decay constant of Cl36
    Zt = z+Ydisp*e*2.75; % calculation of starting depth in cm
    delz = max(diff(ze)); % calc of change in depth for each time step
    delt = delz/(e*2.75); % calc. of timestep
    Ys = 0.44;
    ii = find(ze <= 100);
    ze(ii) = 100;
    Ymz = 10.^(1.586+1.709.*(log10(ze))+(-1.817).*((log10(ze)).^2)+0.9642.*((log10(ze)).^3)...
+(-.2384).*((log10(ze)).^4)+.01955.*((log10(ze)).^5));
for j = 1:length(f35) % Calculating INTnmcz for each sample
    INMCsum = 0;
    Zt = z(j)+Ydisp*e*2.75; % calculation of starting depth in cm
    for i=length(ze):-1:(Zt/10) % summing 36Cl up to Zt
        INMCsum = (((muonf * Ys * f35(j) * Ymz(i)) * delt) + INMCsum) * (exp(-lambda * delt));
    end
    INTnmcz(j) = INMCsum;
End

```

5

```

function [INTNbz] = f_INTNbz(f35,e,z,ze,Ydisp,muonf)
% 36Cl ABUNDANCE FROM BREMSSTRAHLUNG THERMAL NEUTRON CAPTURE, GIVEN
% SAMPLE CHEMISTRY, DEPTH, AND EROSION RATE
%
    lambda = 2.303e-06; % Decay constant of Cl36
    delz = max(diff(ze)); % calc of change in depth for each time step
    delt = delz/(e*2.75); % calc. of timestep
    Yf = 1;
    ii = find(ze <= 100);
    ze(ii) = 100;
    Fmz = 10.^(5.059+2.088.*(log10(ze))+2.235.*((log10(ze)).^2)+1.127.*((log10(ze)).^3)...
+-.2634.*((log10(ze)).^4)+.02138.*((log10(ze)).^5));
for j = 1:length(f35) % Calculating INTnmcz for each of the 43 samples
    INTNBsum = 0;
    Zt = z(j)+Ydisp*e*2.75; % calculation of starting depth in cm
    for i=length(ze):-1:(Zt/10) % summing 36Cl up to Zt
        INTNBsum = (muonf * 5.8e-06*(Fmz(i)*Yf*f35(j)*log(0.104*ze(i))*delt)+INTNBsum)*(exp(-lambda*delt));
    end
    INTNbz(j) = INTNBsum;
End

```

6

```
function [NUfis] = f_NUfis(f35,U)
% Steady state value of 36Cl from U-fission thermal neutrons
lambda = 2.303e-06; % Decay constant of Cl36
PUfis = 0.429.*U.*f35; % Production rate (atoms/yr) from U-fiss TN
NUfis = PUfis/(1-exp(-lambda)); % Steady state number of 36Cl atoms from U-fission
```

7

```
function [NUTh] = f_NUTh(f35,U,Th,X,Y)
% Steady-state 36Cl from U-Th alpha decay thermal neutrons
lambda = 2.303e-06; % Decay constant of Cl36
PUTh = (X.*U+Y.*Th).*f35; % production rate from alpha decay TN
NUTh = PUTh/(1-exp(-lambda)); % steady-state 36Cl atoms
```

8

```
function [Prodzvc] = f_Prodzvc(ca,Yca,zv,z,f35,U,Th,X,Y,Ydisp,e,muonf,neutf,k1,k2)
% calculation of total production rate at depth for each sample THROUGH CHALK
% PCaspzvl is 36Cl production from Ca spallation at depth zv
% PTNspzvl is 36Cl production from spallation thermal neutrons at depth zv
% PCamzvl is 36Cl production from Ca muon capture at depth zv
% PTNmzvl is 36Cl production from thermal neutrons from muon capture at depth zv
% PTNbzvl is 36Cl production from thermal neutrons from bremsstrahlung
% Prad is 36Cl production from radiogenic thermal neutrons
%
% THIS FUNCTION TAKES THE DEPTH IN CHALK (ZC) AT ANY GIVEN TIME AND APPLIES IT
TO
% THESE DIFFERENT REACTIONS
%
% 36Cl FROM Ca SPALLATION
% putting in a sample thickness factor only for those exposed on the scarp itself
if zv == 0;
    ST = 0.96;
else
    ST = 1;
end
index = find(zv==0);

%production at depth zc
PCaspzvc = ((ST*neutf*0.885 * 48.8).*ca.*exp(-zv./160))./100;

% 36Cl FROM SPALLATION THERMAL NEUTRONS
PTNsp = 560; % Production rate of spallogenic neutrons at ground level
Lsp = 160; % neutron attenuation factor
Lth = 33; % thermal neutron diffusion in limestone
rho = 2.75; % density of limestone in g/cm3
if zv == 0;
    ST2 = 1.4; % normalized average production due to 5 cm sample thickness
else
    ST2 = 1;
end
%Production at depth zc
PTNspzvc = ST2*neutf*PTNsp*f35.*0.885.*(((k1.*exp(-zv/Lsp)))+(k2.*exp(-zv/Lth)));

% 36Cl FROM CA MUON CAPTURE
zmuon = zv;
ii = find(zmuon <=100); % getting rid of the log near 0 problem
zmuon(ii) = 100;
```



```

Camzcc = 10.^(3.905-7.139.*(log10(zmuon))+4.629.*((log10(zmuon)).^2)-1.190.*((log10(zmuon)).^3)...
+0.097.*((log10(zmuon)).^4)).*Yca/0.012; %Stone polynomial, chalk
Ymztc = 10.^(1.586+1.709.*(log10(zmuon))+(-1.817).*((log10(zmuon)).^2)+0.9642.*((log10(zmuon)).^3)...
+(-.2384).*((log10(zmuon)).^4)+.01955.*((log10(zmuon)).^5)).*Yca; %Stone poly., total
%
PCamzvc = muonf*(Ymztc*0.905);      %0.905 corrects for surface tilt

```

```

%      36Cl FROM MUON CAPTURE THERMAL NEUTRONS
Ys = 0.44;      % neutron yield per muon capture

```

```

% Production rate at depth zc from muon thermal neutrons
PTNmzcvc = ((muonf*Camzcc./Yca)*Ys).*f35;

```

```

%      36Cl FROM BREMSSTRAHLUNG THERMAL NEUTRONS
Yf = 1;      % neutron yield per stopped muon

```

```

%      Fmz = 10.^(5.059+2.088.*(log10(zmuon))-2.235.*((log10(zmuon)).^2)+1.127.*((log10(zmuon)).^3)...
-.2634.*((log10(zmuon)).^4)+.02138.*((log10(zmuon)).^5));

```

```

% Production rate at depth z from bremsstrahlung
PTNbzvc = muonf*0.7167.*5.8e-06.*(Fmz*Yf).*f35.*log(0.104.*zmuon);

```

```

%      36Cl FROM RADIOGENIC THERMAL NEUTRONS
Pradc = 0.885.*0.429.*U.*f35 + 0.885.*(X.*U+Y.*Th).*f35;

```

```

%      Total 36Cl production at given depth, feeds into Main program
Prodzvc = PCaspzvc + PTNspzvc + PCamzvc + PTNmzcvc + PTNbzvc + Pradc; %production rate of 36Cl for
% each sample at given depth zv in atoms 36cl per gram rock per year

```

9

```

function [Prodzvl] = f_Prodzvl(ca,Yca,zv,z,f35,U,Th,X,Y,Ydisp,e,muonf,neutf,k1,k2)
% calculation of total production rate at depth for each sample THROUGH LIMESTONE
% PCaspzvl is 36Cl production from Ca spallation at depth zv
% PTNspzvl is 36Cl production from spallation thermal neutrons at depth zv
% PCamzvl is 36Cl production from Ca muon capture at depth zv
% PTNmzcvl is 36cl production from thermal neutrons from muon capture at depth zv
% PTNbzvl is 36cl production from thermal neutrons from bremsstrahlung
% Prad is 36Cl production from radiogenic thermal neutrons

```

```

%      THIS FUNCTION TAKES THE DEPTH THROUGH LIMESTONE AT ANY GIVEN
%      TIME AND CALCULATES THE RESULTANT 36Cl PRODUCTION RATE

```

```

%      36Cl PRODUCTION FROM Ca SPALLATION
PCaspzvl = ((neutf * 0.115 * 48.8).*ca.*exp(-zv./160))./100;

```

```

%      36Cl FROM SPALLATION THERMAL NEUTRON CAPTURE
PTNsp = 560;      % Production rate of spallogenic neutrons at ground level
Lsp = 160;
Lth = 33;      % thermal neutron diffusion in limestone
rho = 2.75;      % density of limestone in g/cm3
PTNspzvl = PTNsp*neutf*f35.*0.115.*(((k1.*exp(-zv/Lsp)))+(k2.*exp(-zv/Lth)));

```

```

%      FIXING LOG OF 0 PROBLEM FOR MUON REACTIONS

```

```

      zmuon = zv;
      ii = find(zmuon <=100);
      zmuon(ii) = 100;

```

```

% 36Cl PRODUCTION RATE AT DEPTH ZV FROM Ca MUON CAPTURE

```


$Camzll = 10.^{-0.434-1.964 \cdot (\log_{10}(zmuon)) + 1.787 \cdot ((\log_{10}(zmuon))^2) - 0.535 \cdot ((\log_{10}(zmuon))^3) + 0.044 \cdot ((\log_{10}(zmuon))^4)} \cdot Yca / 0.012$; %Stone polynomial, limestone
 $Ymztl = 10.^{1.586 + 1.709 \cdot (\log_{10}(zmuon)) - 1.817 \cdot ((\log_{10}(zmuon))^2) + 0.9642 \cdot ((\log_{10}(zmuon))^3) - 0.2384 \cdot ((\log_{10}(zmuon))^4) + 0.01955 \cdot ((\log_{10}(zmuon))^5)} \cdot Yca$; %Stone poly., total
 $PCamzvl = muonf \cdot (Ymztl \cdot 0.0952)$;

% 36Cl FROM MUON CAPTURE THERMAL NEUTRONS
 $Ys = 0.44$; % neutron yield per muon capture

% Production rate at depth z from muon thermal neutrons
 $PTNmzvl = ((muonf \cdot Camzll / Yca) \cdot Ys) \cdot f35$;

% 36Cl FROM BREMSSTRAHLUNG THERMAL NEUTRONS
 $Yf = 1$; % neutron yield per stopped muon
 $Fmz = 10.^{5.059 + 2.088 \cdot (\log_{10}(zmuon)) - 2.235 \cdot ((\log_{10}(zmuon))^2) + 1.127 \cdot ((\log_{10}(zmuon))^3) - 0.2634 \cdot ((\log_{10}(zmuon))^4) + 0.02138 \cdot ((\log_{10}(zmuon))^5)}$;

% Production rate at depth z from b.
 $PTNbzvl = muonf \cdot 0.2833 \cdot 5.8e-06 \cdot (Fmz \cdot Yf) \cdot f35 \cdot \log(0.104 \cdot zmuon)$;

% 36Cl FROM RADIOGENIC THERMAL NEUTRONS
 $Pradl = 0.115 \cdot 0.429 \cdot U \cdot f35 + 0.115 \cdot (X \cdot U + Y \cdot Th) \cdot f35$;

% TOTAL 36Cl PRODUCTION RATE AT DEPTH ZL IN ATOMS/GM ROCK/YR
 $Prodzvl = PCaspzvl + PTNspzvl + PCamzvl + PTNmzvl + PTNbzvl + Pradl$